CHAPTER 64

Hierarchial Models of Nanomechanics and Micromechanics

Nasr M. Ghoniem

Mechanical and Aerospace Engineering Department, University of California, Los Angeles, California, USA

Nicholas Kioussis

Department of Physics, California State University Northridge, Northridge, California, USA

CONTENTS

1. INTRODUCTION

Recent interest in *nanotechnology* is challenging the scientific community to analyze, develop, and design nano- to micrometer size devices for applications in new generations of computers, electronics, photonics, and drug delivery systems. These new exciting application areas require novel and sophisticated physically based approaches for design and performance prediction. Thus theory and modeling are playing an ever increasing role in this area to reduce development costs and manufacturing times. An important problem that concerns the microelectronics industry is the reliable operation of integrated circuits (ICs), where the lifetime is limited by the failure of interconnect wires in between submicrometer semiconducting chips. In some cases, the nucleation and growth of even a single nanovoid can cause interconnect failure. Statistical mechanics cannot adequately address this situation. Future electronic and optoelectronic devices are expected to be even smaller, with *nanowires* connecting nano-size memory and information storage and retrieval nanostructures. Understanding the mechanics of such nanoengineered devices will enable high levels of reliability and useful lifetimes to be achieved. Undoubtedly, defects are expected to play a major role in these nano and microsystems due to the crucial impact on the physical and mechanical performance.

The development of ultrastrong, yet ductile materials by combining nanolayers with different microstructure also requires detailed understanding of their mechanical properties. Such materials, if properly designed, may be candidates for many demanding applications (e.g., microelectronics, optoelectronics, laser mirrors, aircraft structures, rocket engines, fuel cells, etc.).

Appropriate validation experiments are crucial to model verification. Models must predict the correct behavior at each length scale. However current nano- and micro-scale mechanical experiments have been mostly limited to indentation [1, 2] and bulge tests [3, 4], and to noncontact tests such as x-ray residual stress measurements [5, 6]. Multiscale interconnected approaches will need to be developed to interpret new and highly specialized nano-/micromechanical tests. One of the advantages of these approaches is that, at each stage, physically meaningful parameters are predicted and used in subsequent models, avoiding the use of empiricism and fitting parameters.

As the material dimensions become smaller, its resistance to deformation is increasingly determined by internal or external discontinuities (e.g., surfaces, grain boundaries, dislocation cell walls, etc.). The Hall-Petch relationship has been widely used to explain grain size effects, although the basis of the relationship is strictly related to dislocation pileups at grain boundaries. Recent experimental observations on nanocrystalline materials with grains of the order of 10–20 nm indicate that the material is weaker than what would be expected from the Hall-Petch relationship [7, 8]. Thus, the interplay between interfacial or grain boundary effects and slip mechanisms within a single crystal grain may result in either strength or weakness, depending on their relative sizes. Although experimental observations of plastic deformation heterogeneities are not new, the significance of these observations has not been addressed till very recently. In same metallic alloys, regular patterns of highly localized deformation zones, surrounded by vast material volumes that contain little or no deformation, are frequently seen [9–11]. The length scale associated with these patterns (e.g., typically the size of dislocation cells, the ladder spacing in persistent slip bands (PSBs), or the spacing between coarse shear bands) controls the material strength and ductility. As it may not be possible to homogenize such types of microstructure in an average sense using either atomistic simulations or continuum theories, new intermediate approaches will be needed.

In this article, we review several components of mechanics that are collectively needed to design new nano and micro materials, and to understand their performance. We first discuss in Section 2 the main aspects of quantum mechanics based methods (*ab initio*). Concepts of statistical mechanics that permit the interpretation of modern atomistic simulation methods,

such as molecular dynamics (MD) and kinetic Monte Carlo (KMC) are introduced in Section 3, together with essential details of empirical interatomic potentials and computational techniques. For a description of the mechanics of materials at length scales where defects and microstructure heterogeneities play important roles, we introduce mesomechanics in Section 4. Finally, applications of nanomechanics and micromechanics are given in Section 5.

2. COMPUTATIONAL QUANTUM MECHANICS

2.1. Essential Concepts

There is little doubt that most of the low-energy physics, chemistry, materials science, and biology can be explained by the quantum mechanics of electrons and ions, and that, in many cases, the properties and behavior of materials derive from the quantum mechanical description of events on the atomic scale. Though there are many examples in materials science of significant progress having been made without any need of quantum-mechanical modeling, this progress is often limited as one pushes forward and encounters the atomic world. For instance, the understanding of the properties of dislocations comes from classical elasticity theory, but even in these cases, until recently, very little was known about the core of a dislocation or the effect of chemistry on the core, precisely because this part of the dislocation requires detailed quantum-mechanical modeling. The ability of quantum mechanics to predict the total energy and the atomic structure of a system of electrons and nuclei, enables one to reap a tremendous benefit from a quantum mechanical calculation. Many methods have been developed for solving the Schrödinger equation that can be used to calculate a wide range of physical properties of materials, which require only a specification of the ions present (by their atomic number). These methods are usually referred to as *ab initio* methods.

In considering the motion of electrons in condensed matter, we are dealing with the problem of describing the motion of an enormous number of electrons and nuclei ($\sim 10^{23}$) obeying the laws of quantum mechanics. Prediction of the electronic and geometric structure of a solid requires calculation of the quantum-mechanical total energy of the system and subsequent minimization of that energy with respect to the electronic and nuclear coordinates. The many-body Schrödinger equation for a system containing n electrons and N nuclei has the form of an eigenvalue problem,

$$\widehat{H}\Psi(\{\mathbf{R_I}, \mathbf{r_i}\}) = \mathbf{E}\Psi(\{\mathbf{R_I}, \mathbf{r_i}\}) \tag{1}$$

with E the total energy of the many-body Hamiltonian operator $\widehat{H}$ given by

$$\widehat{H} = -\sum_I \frac{\hbar^2}{2M_I}\nabla_I^2 - \sum_i \frac{\hbar^2}{2m_{\text{el}}}\nabla_i^2 + \frac{1}{2}\sum_I\sum_{J\neq I}\frac{Z_I Z_J e^2}{|\mathbf{R}_I - \mathbf{R}_J|} - \sum_I\sum_i\frac{Z_I e^2}{|\mathbf{R}_I - \mathbf{r}_i|} + \frac{1}{2}\sum_i\sum_{j\neq i}\frac{e^2}{|\mathbf{r}_i - \mathbf{r}_j|} \tag{2}$$

Here, $\{\mathbf{R_I}\}$ are the positions of the ions, $\{\mathbf{r_i}\}$ are the positions of the electrons, M_I are the masses of the ions, m_e are the masses of the electrons, e is the electronic charge, Z_I is the valence charge of the Ith ion (nucleus plus core electrons), and $\hbar$ is Planck's constant divided by 2π. The terms in the Hamiltonian are successively, the kinetic energy associated with the nuclei, the kinetic energy associated with the electrons, the repulsive ion-ion Coulomb interaction, the attractive ion-electron Coulomb interaction, and finally, the repulsive Coulomb interaction between the electrons. Although in principle everything is known exactly, the Schrödinger equation (1) with this Hamiltonian is simply too difficult to solve directly. Hence, the quantum many-body problem is centered upon finding intelligent approximations to the Hamiltonian and the many body wavefunction, that retain the correct physics and are computationally tractable to solve.

The first simplification of this problem is attributed to Born and Oppenheimer who recognized [12] that in most cases the nuclear and electronic degrees of freedom can be decoupled, as they exhibit vastly different dynamics. Because of the large difference in mass between the electrons and nuclei (three to five orders of magnitude) and the fact that the forces on the particles are the same, the electrons respond essentially instantaneously to the motion

of the nuclei. Thus, the nuclei can be treated adiabatically, leading to a separation of the electronic and nuclear coordinates in the many-body wave function

$$\Psi(\{\mathbf{R}_I, \mathbf{r}_i\}) = \Psi^{\text{el}}_{\{\mathbf{R}_I\}}(\{\mathbf{r}_i\})\Psi^{\text{nuc}}(\{\mathbf{R}_I\}) \tag{3}$$

the so-called Born-Oppenheimer approximation [13, 14]. The *adiabatic principle* reduces the many-body problem in the solution of the dynamics of the electrons in some *frozen-in* configuration $\{\mathbf{R}_I\}$ of the nuclei. Thus, to a good approximation, the kinetic energy of the nuclei in Eq. (2) can be neglected. The electronic wavefunction $\Psi^{\text{el}}_{\{\mathbf{R}_I\}}(\{\mathbf{r}_i\})$ depends on the nuclear positions only parametrically—a different wavefunction needs to be calculated for each nuclear configuration. This is an example of the philosophy behind systematic degree of freedom elimination, which is itself at the heart of multiscale modeling.

Within the Born-Oppenhemer approximation, the complexity of the full many-body Schrödinger equation reduces to that of the simpler electronic Schrödinger equation

$$\widehat{H}^{\text{el}}\Psi^{\text{el}}_{\{\mathbf{R}_I\}}(\{\mathbf{r}_i\}) = E^{\text{el}}_{\{\mathbf{R}_I\}}\Psi^{\text{el}}_{\{\mathbf{R}_I\}}(\{\mathbf{r}_i\}) \tag{4}$$

where

$$\widehat{H}^{\text{el}} = -\sum_i \frac{\hbar^2}{2m_{\text{el}}}\nabla_i^2 + \sum_i V^{\text{ion}}(\mathbf{r}_i) + \frac{1}{2}\sum_i\sum_{j\neq i}\frac{e^2}{|\mathbf{r}_i - \mathbf{r}_j|} \tag{5}$$

and

$$V^{\text{ion}}(\mathbf{r}_i) = -\sum_I \frac{Z_I e^2}{|\mathbf{R}_I - \mathbf{r}_i|} \tag{6}$$

is the ionic potential that every electron experiences.

To calculate the total energy for a given nuclear configuration, we must add the nuclear-nuclear repulsion energy to the electronic energy, namely

$$E^{\text{tot}} = E^{\text{el}}_{\{\mathbf{R}_I\}} + \frac{1}{2}\sum_I\sum_{J\neq I}\frac{Z_I Z_J e^2}{|\mathbf{R}_I - \mathbf{R}_J|} \tag{7}$$

Throughout the rest of the paper the "tot" and "el" superscripts will be dropped and only electronic Hamiltonians and wavefunctions will be considered. Even with this simplification, the many-body problem remains formidable.

Solving the Schrödinger equation with the above Hamiltonian is however still too complex for most cases, as the many-electron wavefunction contains $3N$ variables, which for a solid containing $N \sim 10^{23}$ electrons, is simply an intractable number of degrees of freedom. Devising accurate schemes to approximate the many-electron problem has been an important goal since the founding of quantum mechanics in the early 1900s. Several notable advances have been made, starting with Thomas-Fermi theory [15, 16] in the late 1920s, which makes a significant conceptual assumption about the electron density ($\rho(\mathbf{r})$), as the central unknown variable, rather than the many-electron wavefunction. This approach simplified the problem considerably, as the density contains just three degrees of freedom, namely the x, y, z coordinates of the system. In 1930 came Hartree-Fock theory, which builds upon the single-particle approximation proposed earlier by Hartree, but in addition correctly accounts for the exchange interactions between electrons that are a consequence of the Pauli principle [17]. The various many-body methods just introduced will be discussed in more detail in the following sections.

2.1.1. Free Electron Fermi Gas

As a first step to understand the properties of metals, one can ignore the interactions of the valence electrons both with the ions and the other valence electrons. According to this simplified model, the so-called free electron Fermi gas model, the valence electrons of the constituent atoms become conduction electrons and move free through the volume of the metal. The fact that the electrons are free indicates that they are also independent, which suggests that one can solve the one-electron Schrödinger equation,

$$H\psi(\mathbf{r}) = -\frac{\hbar^2}{2m}\nabla^2\psi(\mathbf{r}) = \epsilon\psi(\mathbf{r}) \tag{8}$$

The solution of Eq. (8) is of the form of a plane wave,

$$\psi_{\mathbf{k}}(\mathbf{r}) = \frac{1}{\sqrt{\Omega}}e^{i\mathbf{k}\cdot\mathbf{r}} \tag{9}$$

where $\Omega = L^3$ is the volume of the confining cubic box of edge length L. Note, that the electronic density, $\rho_{\mathbf{k}}(\mathbf{r}) = |\psi_{\mathbf{k}}(\mathbf{r})|^2 = \psi_{\mathbf{k}}^*(\mathbf{r})\psi_{\mathbf{k}}(\mathbf{r})$, associated with each plane wave is uniform, indicating that the electron is uniformly spread out throughout the confining box. The one-electron energy eigenvalue corresponding to the plane wave characterized by wavevector $\mathbf{k}$ is

$$\epsilon_{\mathbf{k}} = \frac{\hbar^2\mathbf{k}^2}{2m} = \frac{\hbar^2}{2m}(k_x^2 + k_y^2 + k_z^2) \tag{10}$$

The one-electron wavefunctions are required to satisfy specified boundary conditions which in turn restrict the allowed values of the wavevector. For example, one can use periodic boundary conditions

$$\psi_i(\mathbf{r} + \mathbf{L}) = \psi_i(\mathbf{r}) \tag{11}$$

or boundary conditions in which the wavefunction vanishes at the boundary

$$\psi(x = y = z = 0) = \psi(x = L, y, z) = \psi(x, y = L, z) = \psi(x, y, z = L) = 0 \tag{12}$$

Imposing periodic boundary conditions we find that components of the wavevector become quantized, that is,

$$k_i = n_i\frac{2\pi}{L} \tag{13}$$

where $i = x, y, z$. The set of allowed points in k-space is shown schematically in Fig. (1). The isotropy of the energy spectrum implies a wide range of degeneracies. In order to build up the N-electron ground state, we successively fill the one-electron states of lowest energy that are not already occupied, taking into account the Pauli exclusion principle. This demands that no two electrons can have their quantum numbers identical. The quantum numbers of a conduction orbital are (n_x, n_y, n_z, m_s), where $m_s = \pm\frac{1}{2}$ is the spin quantum number.

Thus, for a system of N free electrons in the ground state, the *occupied* single-electron orbitals fill a sphere of radius k_F, the Fermi wavenumber, where the Fermi energy,

$$\epsilon_F = \frac{\hbar^2}{2m}k_F^2 \tag{14}$$

represents the highest occupied single-electron energy at zero temperature.

In the limit $L \to \infty$, the energy levels are so closely spaced so we can just convert the discrete sum over $\mathbf{k}$ states into an integral in k-space, taking into account the number of states per unit volume of k-space. Because the k-points occupy the vertices of a simple cubic lattice in k-space, each such point is assigned to a volume $(2\pi/L)^3$, or, equivalently, there number
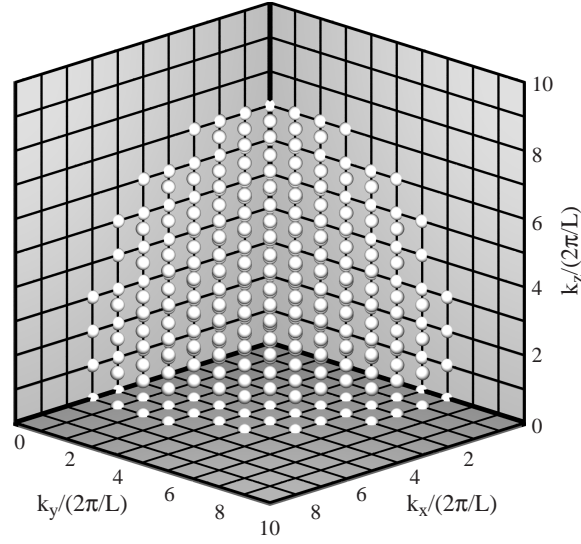
Figure 1. Allowed values of the wavevector for a particle in a cubic box of edge length L employing periodic boundary conditions $\psi_i(\mathbf{r} + \mathbf{L}) = \psi_i(\mathbf{r})$.

of allowed k-values per unit volume of k-space is simply, $(L/2\pi)^3 = \Omega/(2\pi)^3$. Hence, we can replace $\sum_\mathbf{k} = \Omega/(2\pi)^3 \int d^3k$. Thus, the total number of electrons N is given by

$$N = 2\frac{\Omega}{(2\pi)^3} \int_{\epsilon_k \leq \epsilon_F} d^3k = \frac{\Omega k_F^3}{3\pi^2} \tag{15}$$

which gives that

$$k_F = (3\pi^2 \rho)^{1/3} \tag{16}$$

where $\rho = N/\Omega$ is the electron density. It is convenient to use the quantity, r_s, which is defined as the radius of the sphere whose volume is equal to the volume per conduction electron,

$$\frac{4\pi}{3} r_s^3 = \frac{\Omega}{N} = \rho^{-1} \tag{17}$$

The total energy is

$$E_{\text{tot}} = 2 \sum_{k \leq k_F} \epsilon_k = 2\frac{4\pi\Omega}{(2\pi)^3} \int dk\, k^2 \frac{\hbar^2 k^2}{2m} = \frac{\Omega}{\pi^2} \frac{\hbar^2 k_F^5}{10m} \tag{18}$$

From Eqs. (15) and (18) the total energy per electron is

$$\frac{E_{\text{tot}}}{N} = \frac{3}{5}\epsilon_F = \frac{2.21}{(r_s/a_0)^2} \tag{19}$$

or the total energy as a function of the electron density is

$$\frac{E_{\text{tot}}}{\Omega} = \left(\frac{3\hbar^2}{10m}\right)(3\pi^2)^{2/3}\rho^{5/3} \tag{20}$$

In the above equation

$$a_0 = \frac{\hbar^2}{me^2} = 0.529 \times 10^{-8} \text{ cm} \tag{21}$$

is the Bohr radius which is often used as a scale for measuring atomic distances. Values of r_s/a_0 for metals are in the range from about 2 (e.g., in Al) to about 6 (in Cs).

2.1.2. Electrons in Periodic Solids

The next step is understanding the electrons in perfectly periodic solids where the ions are arranged in a regular periodic lattice. In the independent electron approximation, the interactions of the electrons with the ions and the electron-electron interactions are represented by an effective one-electron potential, $V^{\text{eff}}(\mathbf{r})$, which must have the periodicity of the underlying Bravais lattice, that is,

$$V^{\text{eff}}(\mathbf{r} + \mathbf{R}) = V^{\text{eff}}(\mathbf{r}) \tag{22}$$

for all Bravais lattice vectors $\mathbf{R}$

$$\mathbf{R} = n_1 \mathbf{a}_1 + n_2 \mathbf{a}_2 + n_3 \mathbf{a}_3 \tag{23}$$

Here, the $\mathbf{a}_i$s are defined as the *primitive lattice vectors* that generate the lattice and the n_is are integers. It can be shown that the Fourier Transform (FT) of any function satisfying Eq. (22) is of the form

$$V^{\text{eff}}(\mathbf{r}) = \sum_{\mathbf{G}} V^{\text{eff}}(\mathbf{G}) e^{i\mathbf{G}\cdot\mathbf{r}} \tag{24}$$

where the only vectors appearing in the sum are defined as the reciprocal lattice vectors, satisfying the condition

$$\mathbf{R} \cdot \mathbf{G} = 2m\pi \tag{25}$$

where m is any integer and $V^{\text{eff}}(\mathbf{G})$ is the FT component.

Bloch's theorem states that the one-electron eigenstates of the one-electron Hamiltonian,

$$H\psi = \left[-\frac{\hbar^2}{2m} \nabla^2 + V^{\text{eff}}(\mathbf{r}) \right] \psi = \epsilon \psi \tag{26}$$

with $V^{\text{eff}}(\mathbf{r})$ satisfying Eq. (22), has also the same underlying symmetry of the Bravais lattice up to a phase factor,

$$\psi_{\mathbf{k}}(\mathbf{r}) = e^{i\mathbf{k}\cdot\mathbf{r}} u_{\mathbf{k}}(\mathbf{r}) \tag{27}$$

where

$$u_{\mathbf{k}}(\mathbf{r} + \mathbf{R}) = u_{\mathbf{k}}(\mathbf{r}) \tag{28}$$

for all $\mathbf{R}$ in the Bravais lattice.

Due to the periodicity of the lattice, it suffices to study the single-electron Schrödinger Equation (26) only within the primitive unit cell defined by the primitive lattice vectors $\{\mathbf{a}_i\}$s in real space and only for wavevectors $\mathbf{k}$ which lie in the first Brillouin zone (BZ). The first Brillouin zone is the Wigner-Seitz primitive cell in the reciprocal lattice, enclosed by planes that are the perpendicular bisectors of the reciprocal lattice vectors $\{\mathbf{G}\}$s drawn from the origin to the nearby reciprocal lattice points. The importance of the first Brillouin zone is that if the tip of the electron's wavevector lies on the boundary of the BZ it satisfies the Bragg diffraction condition

$$\mathbf{k}' - \mathbf{k} = \Delta\mathbf{k} = \mathbf{G} \tag{29}$$

Thus, the single-electron wavefunction $\psi_{\mathbf{k}}(\mathbf{r})$ can be written as

$$\psi_{\mathbf{k}}(\mathbf{r}) = e^{i\mathbf{k}\cdot\mathbf{r}} \sum_{\mathbf{G}'} c_{\mathbf{k}}(\mathbf{G}') e^{i\mathbf{G}'\cdot\mathbf{r}} \tag{30}$$

where the wavevector $\mathbf{k}$ satisfies the periodic boundary conditions Eq. (13). Substituting the expressions (22) and (30) in the single-electron Schrödinger equation (26) we find

$$\sum_{\mathbf{G}'} \left[\left(\frac{\hbar^2}{2m}(k + G')^2 - \epsilon_{\mathbf{k}} \right) e^{i(\mathbf{k}+\mathbf{G}')\cdot\mathbf{r}} + \sum_{\mathbf{G}} V^{\text{eff}}(\mathbf{G}) e^{i(\mathbf{k}+\mathbf{G}+\mathbf{G}')\cdot\mathbf{r}} \right] c_{\mathbf{k}}(\mathbf{G}') = 0 \tag{31}$$

Multiplying by $\exp -i(\mathbf{k} + \mathbf{G}'') \cdot \mathbf{r}$ and integrating over $\mathbf{r}$ gives

$$\left[\frac{\hbar^2}{2m}(\mathbf{k} + \mathbf{G})^2 - \epsilon_\mathbf{k}\right]c_\mathbf{k}(\mathbf{G}) + \sum_{\mathbf{G}'} V^{\text{eff}}(\mathbf{G} - \mathbf{G}')c_\mathbf{k}(\mathbf{G}') = 0 \tag{32}$$

For each $\mathbf{k}$ point in the first Brillouin zone, the original problem is reduced to a set of linear equations Eq. (32) for the unknown coefficients, $c_\mathbf{k}(\mathbf{G})$, of the single-electron wave-function $\psi_\mathbf{k}(\mathbf{r})$. It is instructive to solve the set of linear equations for the case of a weak periodic potential where all Fourrier components of the potential are negligible except for one $V(\mathbf{G}_0)$, namely

$$\begin{aligned} V^{\text{eff}}(\mathbf{G}) = V(\mathbf{G}_0), &\quad \text{if } \mathbf{G} = \mathbf{G}_0; \\ 0, &\quad \text{if } \mathbf{G} = \mathbf{G}_0 \end{aligned} \tag{33}$$

In this case, Eq. (32) reduces to a system of two linear equations of the form

$$\left[\frac{\hbar^2\mathbf{k}^2}{2m} - \epsilon_\mathbf{k}\right]c_\mathbf{k}(0) + V^*(\mathbf{G}_0)c_\mathbf{k}(\mathbf{G}_0) = 0 \tag{34}$$

$$\left[\frac{\hbar^2(\mathbf{k} + \mathbf{G}_0)^2}{2m} - \epsilon_\mathbf{k}\right]c_\mathbf{k}(\mathbf{G}_0) + V(\mathbf{G}_0)c_\mathbf{k}(0) = 0 \tag{35}$$

Solving the system gives two eigenvalues

$$\epsilon_\mathbf{k} = \frac{\hbar^2\mathbf{k}^2}{2m} \pm |V(\mathbf{G}_0)| \tag{36}$$

one lower than the free-electron kinetic energy by $|V(\mathbf{G}_0)|$, and one higher by $|V(\mathbf{G}_0)|$. Thus, this simple type of potential energy, $2|V(\mathbf{G}_0)|\cos(Gx)$ has created and energy gap of $E_{\text{gap}} = 2|V(\mathbf{G}_0)|$ at the zone boundary.

2.1.3. Pseudopotential Method

In solving the single-electron Schrödinger equation [Eq. (22)], the effective potential includes the ionic potential, which varies rapidly in the vicinity of the nucleus and is weakly varying in the region between nuclei, in the so-called interstitial region. It is helpful to distinguish between the valence and core electrons: the core wavefunctions are well localized about the lattice sites, whereas the valence electrons have appreciably probability in the interstitial regions where they participate very actively in the crystal bonding. The valence wavefunctions oscillate very rapidly in the core region, whereas they vary smoothly in the interstitial region. Their complicated nodal structure in the core region is created from the requirement that the wave function be orthogonal to the wave functions of the core electrons. Because of this difference between the valence and core electrons, the pseudopotential method has been developed [18]. The pseudopotential is constructed such that it matches the true potential outside a given radius, designated the core radius. Similarly, each pseudowavefunction must match the corresponding true wavefunction beyond this distance. In Fig. 2, we show the schematic representation of the construction of the pseudo-wavefunction and pseudopotential. In addition, the charge densities obtained outside the core region must be identical to the true charge density. Thus, the integral of the squared amplitudes of the real and pseudo wave functions over the core region must be identical. This condition is known as norm-conservation.

The "pseudopotential" V^{pseudo} and the pseudo wave function $|\tilde{\phi}^{(v)}\rangle$ are given by

$$V^{\text{pseudo}} = V^{\text{eff}} + \sum_c (\epsilon^{(v)} - \epsilon^{(c)})|\psi^{(c)}\rangle\langle\psi^{(c)}| \tag{37}$$

and

$$|\psi^{(v)}\rangle = |\tilde{\phi}^{(v)}\rangle - \sum_c \langle\psi^{(c)}|\tilde{\phi}^{(v)}\rangle|\psi^{(c)}\rangle \tag{38}$$
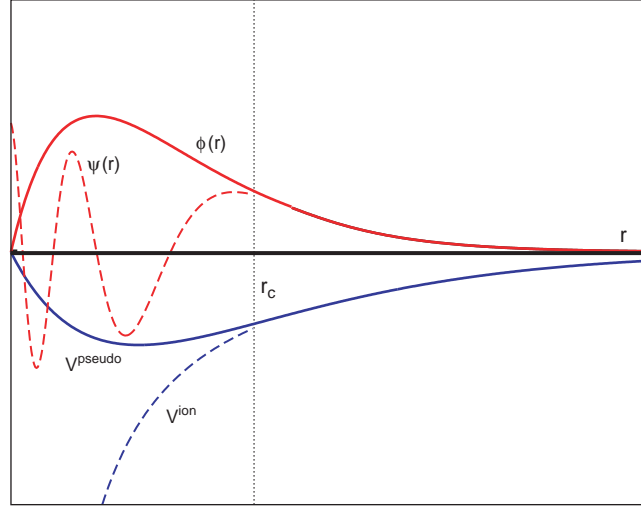
Figure 2. Schematic diagram of the real (dashed red curve) and pseudo (solid red curve) wavefunction, $|\tilde{\phi}^{(v)}\rangle$, respectively. Also, we show the Coulomb potential $V^{Coul}(r)$ (dashed blue curve) and the pseudopotential V^{pseudo} (solid blue curve); r_c is the cutoff radius.

Here, $|\psi^{(c)}\rangle$ and $|\psi^{(v)}\rangle$ are the single-electron states for the core and valence electrons, respectively, and $\epsilon^{(c)}$ and $\epsilon^{(v)}$ are the corresponding single-electron core and valence energies. Because $\epsilon^{(v)} \rangle \epsilon^{(c)}$, the second term is repulsive and tends to push the $|\tilde{\phi}^{(v)}\rangle$ outside the core. Thus, the resulting pseudopotential (and consequently the pseudo wave function) is a smooth function in this region reducing the number of plane waves needed in the basis expansion. This is known as the cancellation theorem [19].

2.1.4. The Hartree and Hartree-Fock Approximations

The Hartree approximation is one of the simplest approximate theories for solving the many body Hamiltonian. It is based on the assumption of independent electrons and that the true many-body wavefunction can be written as a product of single-particle wavefunctions of the form

$$\Psi(\mathbf{r}_1\sigma_1, \mathbf{r}_2\sigma_2, \ldots, \mathbf{r}_N\sigma_N) = \varphi_1(\mathbf{r}_1\sigma_1)\varphi_2(\mathbf{r}_2\sigma_2) \ldots \varphi_N(\mathbf{r}_N\sigma_N) \tag{39}$$

where the one-electron wavefunctions, $\varphi_i(\mathbf{r}_i\sigma_i) = \phi_i(\mathbf{r}_i)\sigma_i$, are an orthonormal set, that is,

$$\langle\varphi_i|\varphi_j\rangle = \delta_{i,j} \tag{40}$$

Here, $\phi_i(\mathbf{r}_i)$ is the spatial orbital and σ_i a two component spinor, $\alpha = \binom{1}{0}$ for spin up and $\beta = \binom{0}{1}$ for spin down-electron with respect to a preferred axis.

When the electron system is in the state, $\Psi(\{\mathbf{r}_i\sigma_i\})$, the expectation value of the energy is given by,

$$E[\Psi] = \langle H\rangle_\Psi = \frac{\langle\Psi|\widehat{H}|\Psi\rangle}{\langle\Psi|\Psi\rangle} = \frac{\int \Psi^*\widehat{H}\Psi d\mathbf{r}_1 \ldots d\mathbf{r}_N}{\int \Psi^*\Psi d\mathbf{r}_1 \ldots d\mathbf{r}_N} \tag{41}$$

The expectation value of the Hamiltonian in the state of Eq. (39) is

$$\langle H\rangle_\Psi = \sum_i \int d\mathbf{r}\phi_i^*(\mathbf{r})\left[-\frac{\hbar^2}{2m}\nabla_\mathbf{r}^2 + V^{ion}(\mathbf{r})\right]\phi_i(\mathbf{r})$$

$$+ \frac{e^2}{2}\sum_{i,jj\neq i}\int d\mathbf{r}\,d\mathbf{r}'\phi_i^*(\mathbf{r})\phi_j^*(\mathbf{r}')\frac{1}{|\mathbf{r}-\mathbf{r}'|}\phi_i(\mathbf{r})\phi_j(\mathbf{r}') \tag{42}$$

The best solution $|\Psi\rangle$ must be a stationary state of the system, that is, $\delta E[\Psi] = 0$. The variations of the bra and ket of ϕs are considered to be independent of each other because

the wavefunctions are complex quantities. Thus, minimizing $E[\Psi]$ with respect to variations in $\langle\delta\phi_i|$, subject to the constraint $\sum_i \epsilon_i\langle\delta\phi_i|\phi_i\rangle = 0$, where ϵ_i are Lagrange multipliers, we find

$$\sum_i \int \delta\phi_i^*(\mathbf{r})\left[-\frac{\hbar^2}{2m}\nabla_{\mathbf{r}}^2 + V^{\text{ion}}(\mathbf{r}) + e^2\sum_{j\neq i}\int \phi_j^*(\mathbf{r}')\frac{1}{|\mathbf{r}-\mathbf{r}'|}\phi_j(\mathbf{r}')d\mathbf{r}' - \epsilon_i\right]\phi_i(\mathbf{r})d\mathbf{r} = 0 \quad (43)$$

Since the variations $\langle\delta\phi_i|$ are independent, the above equation cannot be satisfied unless the coefficients of each $\langle\delta\phi_i|$ vanish independently, namely

$$\left[-\frac{\hbar^2}{2m}\nabla_{\mathbf{r}}^2 + V^{\text{ion}}(\mathbf{r}) + \sum_{j\neq i}\int \phi_j^*(\mathbf{r}')\frac{e^2}{|\mathbf{r}-\mathbf{r}'|}\phi_j(\mathbf{r}')d\mathbf{r}'\right]\phi_i(\mathbf{r}) = \epsilon_i\phi_i(\mathbf{r}) \quad (44)$$

These equations for each occupied one-electron orbital, $\phi_i(\mathbf{r})$, are called the *Hartree equations*. They are eigenvalue equations for a single electron moving in the Coulomb potential of the nuclei plus the Hartree potential

$$V_i^H(\mathbf{r}) = \sum_{j\neq i}\int \phi_j^*(\mathbf{r}')\frac{e^2}{|\mathbf{r}-\mathbf{r}'|}\phi_j(\mathbf{r}')d\mathbf{r}' = \sum_{j\neq i}\int d\mathbf{r}' \frac{\rho_j(\mathbf{r}')}{|\mathbf{r}-\mathbf{r}'|} \quad (45)$$

due to all the other electrons, which depends on their charge density $e|\phi_i(\mathbf{r}')|^2$. This charge density is only known after the above equations have been solved for each i. The self-consistent field approximation is an iterative procedure for solving the above set of nonlinear equations. A trial function is used to calculate the initial charge density. New single particle wave functions are found by numerically solving the above equations. These wave functions now yield new charge densities, which in turn yield new wave functions. The procedure is repeated until self consistency is reached.

The Hartree approximation does not include the electronic correlations associated with the fermionic nature of the electrons. Namely, the many-electron wavefunction needs to be antisymmetric with respect to an interchange of any two electrons,

$$\Psi(\mathbf{r}_1\sigma_1,\ldots,\mathbf{r}_i\sigma_i,\ldots,\mathbf{r}_j\sigma_j,\ldots,\mathbf{r}_N\sigma_N) = -\Psi(\mathbf{r}_1\sigma_1,\ldots,\mathbf{r}_j\sigma_j,\ldots,\mathbf{r}_i\sigma_i,\ldots,\mathbf{r}_N\sigma_N) \quad (46)$$

a requirement imposed by the Pauli exclusion principle.

The next simplest generalization of the Hartree approximation is the Hartree-Fock approximation. It is based on the assumption of independent electrons and that the true many-body wavefunction can be written in the form of a single Slater determinant of single-electron wave functions, the so-called spin-orbitals

$$\Psi(\mathbf{r}_1\sigma_1,\ldots,\mathbf{r}_N\sigma_N) = \frac{1}{\sqrt{N!}}\begin{vmatrix} \varphi_1(\mathbf{r}_1\sigma_1) & \varphi_1(\mathbf{r}_2\sigma_2) & \ldots & \varphi_1(\mathbf{r}_N\sigma_1) \\ \varphi_2(\mathbf{r}_1\sigma_1) & \varphi_2(\mathbf{r}_2\sigma_2) & \ldots & \varphi_2(\mathbf{r}_N\sigma_N) \\ \vdots & \vdots & \ddots & \vdots \\ \varphi_N(\mathbf{r}_1\sigma_1) & \varphi_N(\mathbf{r}_2\sigma_2) & \ldots & \varphi_N(\mathbf{r}_N\sigma_N) \end{vmatrix} \quad (47)$$

This simple *ansatz* for the wavefunction Ψ captures much of the physics required for accurate solutions of the Hamiltonian.

The expectation value of the energy in the Hartree-Fock state of Eq. (47) becomes

$$\langle H\rangle_\Psi = \sum_i \int d\mathbf{r}\, \phi_i^*(\mathbf{r})\left[-\frac{\hbar^2}{2m}\nabla_{\mathbf{r}}^2 + V^{\text{ion}}(\mathbf{r})\right]\phi_i(\mathbf{r})$$

$$+ \frac{e^2}{2}\sum_{i,jj\neq i}\int d\mathbf{r}\,d\mathbf{r}'\,\phi_i^*(\mathbf{r})\phi_j^*(\mathbf{r}')\frac{1}{|\mathbf{r}-\mathbf{r}'|}\phi_i(\mathbf{r})\phi_j(\mathbf{r}')$$

$$- \frac{e^2}{2}\sum_{i,jj\neq i}\delta_{s_is_j}\int d\mathbf{r}\,d\mathbf{r}'\,\phi_i^*(\mathbf{r})\phi_j^*(\mathbf{r}')\frac{1}{|\mathbf{r}-\mathbf{r}'|}\phi_i(\mathbf{r}')\phi_j(\mathbf{r}) \quad (48)$$

Minimizing the above equation with respect to $\delta\psi_i^*$, subject to the constraint $\Sigma_i \epsilon_i \int d\mathbf{r}\delta\phi_i^*(\mathbf{r})\phi_i(\mathbf{r}) = 0$ leads to the Hartree-Fock equations

$$\left[-\frac{\hbar^2}{2m}\nabla_{\mathbf{r}}^2 + V^{\text{ion}}(\mathbf{r}) + V^H(\mathbf{r})\right]\phi_i(\mathbf{r}) - e^2\sum_{j\neq i}\delta_{s_i s_j}\int d\mathbf{r}'\phi_j^*(\mathbf{r}')\frac{1}{|\mathbf{r}-\mathbf{r}'|}\phi_i(\mathbf{r}')\phi_j(\mathbf{r}) = \epsilon_i\phi_i(\mathbf{r}) \quad (49)$$

The last negative term in Eq. (49) which acts solely between electrons with parallel spins is called the *exchange term*. It is a nonlocal operator involving the product $\phi_i(\mathbf{r}')\phi_i(\mathbf{r})$ rather than the $|\phi_i(\mathbf{r})|^2$. The gain in potential energy found in Hartree-Fock descends from the fact that the Pauli principle is built into the many-body wave function and keeps apart electrons with parallel spins, lowering their Coulomb repulsive interaction energy on average.

2.1.5. Hartree-Fock Approximation for a Free Electron Gas

The Hartree-Fock equations can be solved exactly for the jellium model, in which the periodic array of ions is replaced with a uniform distribution of positive charge with the same density as the electronic charge. Recall that the electronic charge density for the free electron model is also uniform. Hence, the ionic potential precisely cancels the Hartree potential and the only term surviving is the exchange potential. In the plane wave basis $\phi_i \rightarrow \phi_{\mathbf{k}}$ the exchange potential assumes the form

$$-\frac{e^2}{\sqrt{\Omega}}\sum_{\mathbf{k}'}\int d\mathbf{r}'\frac{e^{-i\mathbf{k}'\cdot\mathbf{r}'}e^{i\mathbf{k}\cdot\mathbf{r}'}e^{i\mathbf{k}'\cdot\mathbf{r}}}{\Omega}\frac{1}{|\mathbf{r}-\mathbf{r}'|} = -\frac{e^2}{\sqrt{\Omega}}\left[\sum_{\mathbf{k}'}\int d\mathbf{r}'\frac{e^{-i(\mathbf{k}-\mathbf{k}')\cdot(\mathbf{r}-\mathbf{r}')}}{\Omega}\frac{1}{|\mathbf{r}-\mathbf{r}'|}\right]e^{i\mathbf{k}\cdot\mathbf{r}} \quad (50)$$

Expressing the Coulomb interaction in terms of its Fourier transform

$$\frac{1}{|\mathbf{r}-\mathbf{r}'|} = \int \frac{d\mathbf{q}}{(2\pi)^3}\frac{4\pi}{q^2}e^{i\mathbf{q}\cdot(\mathbf{r}-\mathbf{r}')} \quad (51)$$

the exchange potential becomes

$$-\frac{4\pi e^2}{\sqrt{\Omega}}\int_{k'<k_F}\frac{d\mathbf{k}'}{(2\pi)^3}\int \frac{d\mathbf{q}}{q^2}\left[\frac{1}{(2\pi)^3}\int d\mathbf{r}'e^{-i(\mathbf{k}-\mathbf{k}'-\mathbf{q})\cdot(\mathbf{r}-\mathbf{r}')}\right]e^{i\mathbf{k}\cdot\mathbf{r}}$$

$$= -\frac{4\pi e^2}{\sqrt{\Omega}}\left[\int_{k'<k_F}\frac{d\mathbf{k}'}{(2\pi)^3}\int d\mathbf{q}\frac{\delta(\mathbf{k}-\mathbf{k}'-\mathbf{q})}{q^2}\right]e^{i\mathbf{k}\cdot\mathbf{r}}$$

$$= -\frac{4\pi e^2}{\sqrt{\Omega}}\left[\frac{1}{(2\pi)^3}\int_{k'<k_F}\frac{d\mathbf{k}'}{|\mathbf{k}-\mathbf{k}'|^2}\right]e^{i\mathbf{k}\cdot\mathbf{r}} = -\frac{2e^2}{\pi}k_F F\left(\frac{k}{k_F}\right)\left[\frac{1}{\sqrt{\Omega}}e^{i\mathbf{k}\cdot\mathbf{r}}\right] \quad (52)$$

where the function $F(x)$ is defined as

$$F(x) = \frac{1}{2} + \frac{1-x^2}{4x}\ln\left|\frac{1+x}{1-x}\right| \quad (53)$$

Thus, the single particle Hartree-Fock energy $\epsilon_{\mathbf{k}}$ is

$$\epsilon_{\mathbf{k}} = \frac{\hbar^2 \mathbf{k}^2}{2m} - \frac{2e^2}{\pi}k_F F\left(\frac{k}{k_F}\right)$$

$$= \left[\left(\frac{(9\pi/4)^{1/3}}{r_s/a_0}\right)^2 (k/k_F)^2 - \frac{4}{\pi}\left(\frac{(9\pi/4)^{1/3}}{r_s/a_0}\right)F\left(\frac{k}{k_F}\right)\right]Ry \quad (54)$$

In deriving the second line in Eq. (54), we have used the unit of energy rydberg

$$\frac{\hbar^2}{2ma_0^2} = \frac{e^2}{2a_0} = 1Ry \quad (55)$$

and Eqs. (11) and (12) for k_F in terms of the density and r_s. The function $F(x)$ and the single particle energy $\epsilon_{\mathbf{k}}$ normalized to ϵ_F for $r_s/a_0 = 4$ are plotted in Figs. 3a and 3b, respectively. The expression Eq. (54) predicts that the derivative of the renormalized single-particle
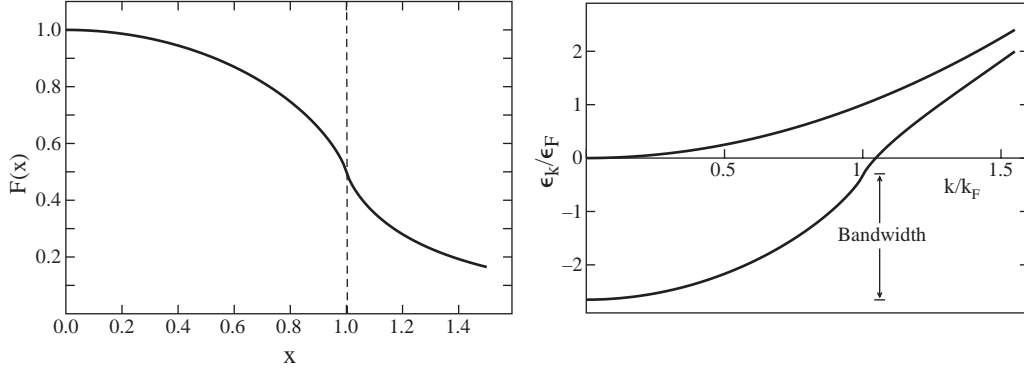
Figure 3. Left panel: The function F(x) defined in equation. Right panel: The single-electron Hartree-Fock energy normalized to the Fermi energy value $\epsilon_{\mathbf{k}}^{\mathrm{HF}}/\epsilon_F = \left[(k/k_F)^2 - 0.663(r_s/a_0)F(k/k_F)\right]$ plotted as a function of k/k_F for $r_s/a_0 = 4$. The single-electron Hartree-Fock energy is compared to the corresponding free-electron energy.

energy $\epsilon_{\mathbf{k}}^{\mathrm{HF}}$ has a logarithmic divergence at $|\mathbf{k}| = k_F$. Namely, on the Fermi surface the effective mass

$$m^* \equiv \frac{\hbar^2 k_F}{\left|\nabla_{\mathbf{k}}\epsilon_{\mathbf{k}}^{\mathrm{HF}}\right|_{k=k_F}} \tag{56}$$

and the density of single-particle, which is proportional to m^* vanish within Hartree-Fock. The main fault within the Hartree-Fock approximation is that by including exchange between electrons with parallel spin, but neglecting correlations due to the Coulomb repulsions which are most effective for electrons with antiparallel spins, it includes neither screening nor the collective plasma excitation. The singularity can be traced back to the very long range of the inverse square of the Coulomb interaction which has a Fourier transform $4\pi e^2/q^2$ diverging at $q = 0$.

The total energy of the N-electron system can be calculated by summing the occupied $(k < k_F)$ single-particle Hartree-Fock energies

$$E_{\mathrm{tot}}^{\mathrm{HF}} = 2\sum_{k\leq k_F}\frac{\hbar^2 k^2}{2m} - \frac{e^2 k_F}{\pi}\sum_{k\leq k_F}\left[1 + \frac{k_F^2 - k^2}{2kk_F}\ln\left|\frac{k_F + k}{k_F - k}\right|\right] \tag{57}$$

The first term is simply the kinetic energy of the ideal Fermi system in Eq. (57). Upon converting the second term into an integral, the total Hartree-Fock energy is

$$\frac{E_{\mathrm{tot}}^{\mathrm{HF}}}{N} = \left[\frac{3}{5}\epsilon_F - \frac{3}{4}\frac{e^2 k_F}{\pi}\right] = \left[\frac{2.21}{(r_s/a_0)^2} - \frac{0.916}{(r_s/a_0)}\right]Ry \tag{58}$$

Because r_s/a_0 in metals is in the range from to 2 to 6, the second term in Eq. (58) is comparable to the first in size. Notice That for small values of r_s (high densities), the kinetic energy term dominates. As r_s increases, the exchange term contributes more and more to $E_{\mathrm{tot}}^{\mathrm{HF}}/N$ and eventually gives binding. In the low density limit $(r_s \to \infty)$, the exchange contribution dominates. In this limit correlation effects become dominant leading to the formation of Wigner lattices [20]. Only then the overlap of the electronic wave functions will be small enough that the formation of energy band with delocalized electrons will be overcome by the long-range Coulomb interaction leading to crystallization of the electrons.

As discussed before, in the Hartree-Fock method electrons of the same spin are prevented from occupying the same space volume. On the other hand, electrons with antiparallel spin come arbitrary close and the pair correlation function is independent of $\mathbf{r}$. There is no tendency to keep electrons apart to reduce their Coulomb repulsion. The pair distribution function calculated from the true ground-state wave function is expected to be strongly reduced for small electron distances. The correlation energy is defined as the difference

between the energy in the Hartree-Fock limit ($E_{\text{tot}}^{\text{HF}}$) and the exact nonrelativistic energy of a system ($E_{\text{tot}}^{\text{exact}}$), namely

$$E_{\text{tot}}^{\text{exact}} \equiv E_{\text{tot}}^{\text{HF}} + E^{\text{corr}} \tag{59}$$

This energy will always be negative because the Hartree-Fock energy is an upper bound to the exact energy (this is guaranteed by the variational theorem, as explained above). The exact nonrelativistic energy $E_{\text{tot}}^{\text{exact}}$ could, in principle, be calculated by performing a full configuration interaction (CI) calculation in a complete one-electron basis set or a full diffusion Monte Carlo calculation [17].

Hartree-Fock theory is a useful tool for many problems. Results can be systematically improved through an increasingly rigorous choice of basis set. It gives good structures and vibrational modes for small molecules, although tends to under predict bond lengths with a corresponding over prediction of frequencies [17]. A major flaw with the method is the lack of electron correlation (leading to zero density of states at the Fermi level for jellium). This precludes the use of Hartree-Fock theory in problems such as, for example, metallic systems. The difference in correlation between ground and excited states in real systems means that Hartree-Fock greatly over predicts the width of the band gap.

2.1.6. Thomas-Fermi Theory

The Thomas-Fermi theory [15, 16] marks a change in approach from Hartree and Hartree-Fock theory, as it was the first method to propose using the electronic charge density as its fundamental variable instead of the many-body wavefunction. It is thus the earliest form of density functional theory. The model can be understood with reference to Fig. 4. Although the charge density is that of a nonuniform electron gas, the number of electrons in a given element, $d|\mathbf{r}|$, can be expressed as $\rho(r)\,dr$, where $\rho(r)$ is the charge density for a uniform electron gas at that point. The Thomas-Fermi energy functional, $E^{\text{TF}}[\rho(\mathbf{r})]$ is

$$E^{\text{TF}}[\rho(\mathbf{r})] = \frac{3\hbar^2}{10m}(3\pi^2)^{2/3} \int \rho^{5/3}(\mathbf{r})\,d\mathbf{r} + \int \rho(\mathbf{r})V^{\text{ion}}(\mathbf{r})\,d\mathbf{r} + \frac{1}{2}\int\int \frac{\rho(\mathbf{r})\rho(\mathbf{r}')}{|\mathbf{r}-\mathbf{r}'|}\,d\mathbf{r}\,d\mathbf{r}' \tag{60}$$

The first term is the electronic kinetic energy associated with a system of non-interacting electrons in a homogeneous electron gas. This form is obtained by integrating the kinetic energy density of a homogeneous electron gas of density $d\mathbf{r}$ at $\mathbf{r}$, which is given by Eq. (20). The second term is the classical electrostatic energy between the nuclei and the electrons, where $V^{\text{ion}}(\mathbf{r})$ is given by Eq. (6). Finally, the third term represents the electron-electron interactions of the system, that is, the Hartree energy.

To obtain the ground state density and energy of the system, the Thomas-Fermi energy functional must be minimized subject to the constraint that the number of electrons is conserved

$$N = \int \rho(\mathbf{r})\,d\mathbf{r} \tag{61}$$
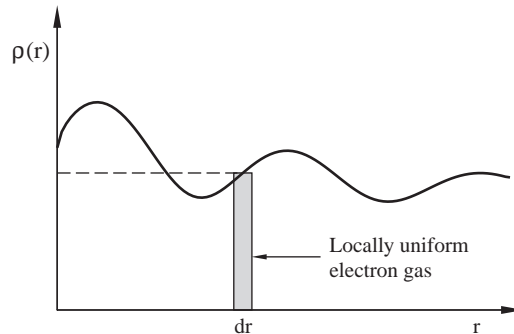
Figure 4. Schematic diagram showing the principle of the local density approximation and also Thomas-Fermi theory. Namely that for a given radial slab, dr, the local charge density can be considered to be $\rho(r)$, the density of an equivalent *uniform* homogeneous electron gas.

This type of constrained minimization problem, which occurs frequently within many-body methods, can be performed using the technique of Lagrange multipliers, μ, leading to the stationary condition

$$\delta\left[E^{\mathrm{TF}}[\rho(\mathbf{r})] - \mu\left(\int \rho(\mathbf{r})\,d\mathbf{r} - N\right)\right] = 0 \tag{62}$$

which leads to the so-called Thomas-Fermi equations,

$$\frac{\hbar^2}{2m}(3\pi^2)^{2/3}\rho^{2/3}(\mathbf{r}) + V^{\mathrm{ion}}(\mathbf{r}) + \frac{1}{2}\int\frac{\rho(\mathbf{r}')}{|\mathbf{r}-\mathbf{r}'|}d\mathbf{r}' - \mu = 0 \tag{63}$$

that can be solved directly to obtain the ground-state density.

Thomas-Fermi theory suffers from many deficiencies, probably the most serious defect is that it does not predict bonding between atoms [21], so molecules and solids cannot form in this theory. The main source of error comes from approximating the kinetic energy in such a crude way. The kinetic energy represents a substantial portion of the total energy of a system and so even small errors prove disastrous. Another shortcoming is the over-simplified description of the electron-electron interactions, which are treated classically and so do not take account of quantum phenomenon such as the exchange interaction.

2.1.7. Density Functional Theory

Density functional theory (DFT) [13, 14, 22–24] has been proven to be a very powerful quantum mechanical method in investigating the electronic structure of atoms, molecules, and solids. Here, the density of the electrons, $\rho(\mathbf{r})$, or spin density, $\rho_\sigma(\mathbf{r})$, is the fundamental quantity, rather the total wave function employed for example in Hartree-Fock theory [25]. The DFT makes successful predictions of ground-state properties for moderately correlated electronic systems [26]. DFT can provide accurate ground-state properties for real materials—such as total energies and energy differences, cohesive energies of solids and atomization energies of molecules, surface energies, energy barriers, atomic structure, and magnetic moments—and provides a scheme for calculating them [17, 24, 26].

We next give a brief discussion of the essential concepts of DFT. Hohenberg and Kohn [23] proved that the total energy, including exchange and correlation, of an electron gas (even in the presence of a static external potential) is a unique functional of the electron density. The minimum value of the total-energy functional is the ground-state energy of the system, and the density that yields this minimum value is the exact single-particle ground-state density. Kohn and Sham [22] then showed how it is possible, formally, to replace the many-electron problem by an exactly equivalent set of self-consistent one-electron equations

$$\left[-\frac{1}{2}\nabla^2 + v_\sigma(\mathbf{r}) + \int \mathbf{d^3r'}\frac{\rho(\mathbf{r}')}{|\mathbf{r}-\mathbf{r}'|} + v_{xc}^\sigma(\mathbf{r})\right]\psi_{\mathbf{k}}\sigma(\mathbf{r}) = \epsilon_{\mathbf{k}\sigma}\psi_{\mathbf{k}\sigma}(\mathbf{r}) \tag{64}$$

where $\psi_{\mathbf{k}\sigma}(\mathbf{r})$ are the Kohn-Sham orbitals, and the spin-dependent exchange-correlation potential is defined as

$$v_{xc}^\sigma(\mathbf{r}) \equiv \frac{\delta\mathbf{E}_{xc}[\rho_\uparrow, \rho_\downarrow]}{\delta\rho_\sigma(\mathbf{r})} \tag{65}$$

Here, $E_{xc}[\rho_\uparrow, \rho_\downarrow]$ is the exchange-correlation energy and the density of electrons, $\rho_\sigma(\mathbf{r})$, of spin $\sigma(=\uparrow, \downarrow)$ is found by summing the squares of the occupied orbitals,

$$\rho_\sigma(\mathbf{r}) = \sum_{\mathbf{k}}|\psi_{\mathbf{k}\sigma}(\mathbf{r})|^2\theta(\mu - \epsilon_{\mathbf{k}\sigma}) \tag{66}$$

where $\theta(x)$ is the step function and μ is the chemical potential. The exchange-correlation energy is "nature's glue." It is largely responsible for the binding of atoms to form molecules and solids. The total electronic density is

$$\rho(\mathbf{r}) = \rho_\uparrow(\mathbf{r}) + \rho_\downarrow(\mathbf{r}) \tag{67}$$

Aside from the nucleus-nucleus repulsion energy, the total energy is

$$E = \sum_{\mathbf{k}\sigma} \left\langle \psi_{\mathbf{k}\sigma} \left| -\frac{1}{2}\nabla^2 \right| \psi_{\mathbf{k}\sigma} \right\rangle \theta(\mu - \epsilon_{\mathbf{k}\sigma}) + \sum_{\sigma} \int d\mathbf{r} v_{\sigma}(\mathbf{r}) \rho_{\sigma}(\mathbf{r}) + U[\rho] + E_{xc}[\rho_{\uparrow}, \rho_{\downarrow}] \qquad (68)$$

where

$$U[\rho] = \frac{1}{2} \int d^3r \int d^3r' \frac{\rho(\mathbf{r})\rho(\mathbf{r}')}{|\mathbf{r} - \mathbf{r}'|} \qquad (69)$$

is the Hartree self-repulsion of the electron density.

The Kohn-Sham equations represent a mapping of the interacting many-electron system onto a system of noninteracting electrons moving in an effective nonlocal potential due to all the other electrons. The Kohn-Sham approach achieves an exact correspondence of the density and the ground-state energy of noninteracting Fermions and the "real" many body system described by the Schrödinger equation. A schematic cartoon representing this relationship is displayed in Fig. 5.

The Kohn-Sham equations must be solved self-consistently so that the occupied electronic states generate a charge density that produces the electronic potential that was used to construct the equations. New iterative diagonalization approaches can be used to minimize the total-energy functional [27–29]. These are much more efficient than the traditional diagonalization methods. If the exchange-correlation energy functional were known exactly, then taking the functional derivative with respect to the density would produce an exchange-correlation potential that included the effects of exchange and correlation exactly.

The complexity of the real many-body problem is contained in the unknown exchange correlation potential, $v_{xc}^{\sigma}(\mathbf{r})$. Nevertheless, making simple approximations, we can hope to circumvent the complexity of the problem. Indeed the simplest possible approximation, that is, the local-density (LDA) or local-spin-density (LSDA) approximation, have been proven [22, 30] very successful.

2.2. The Local Density Approximation

This simplest method of describing the exchange-correlation energy of an electronic system has been the workhorse of condensed matter physics for almost 30 years. In the LSDA, the exchange-correlation energy of an electronic system is constructed by assuming that the exchange-correlation energy per electron at a point $\mathbf{r}$ in the electron gas, ϵ_{xc}, is equal to the
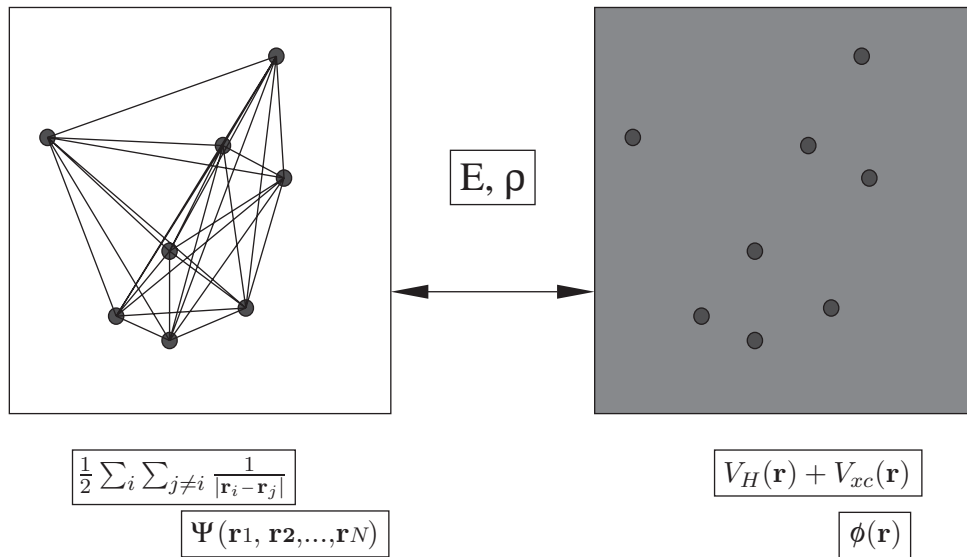
Figure 5. Schematic representation of the relationship between the "real" many-body system (left-hand side) and the noninteracting system of Kohn-Sham density functional theory (right-hand side).

1. Pick a trial one-electron potential $V^{eff}_{(in)}(\mathbf{r})$

$\downarrow$

2. Solve $H\psi_{\mathbf{k}}(\mathbf{r}) = [\leftarrow\frac{\hbar^2}{2m}\nabla^2 - V^{eff}_{(in)}(\mathbf{r})]\psi_{\mathbf{k}}(\mathbf{r}) = \epsilon_{\mathbf{k}}\psi_{\mathbf{k}}(\mathbf{r})$

$\downarrow$

3. Calculate $\rho(\mathbf{r})$

$\downarrow$

4. Construct $V_H(\mathbf{r})$, $V_{xc}(\mathbf{r})$, and $V^{eff}_{(out)}(\mathbf{r})$

$\downarrow$

5. If $|V^{eff}_{(out)}(\mathbf{r}) - V^{eff}_{(in)}(\mathbf{r})| < \delta$ calculate total energy; else, mix V_{out} and V_{in} and GOTO 2.
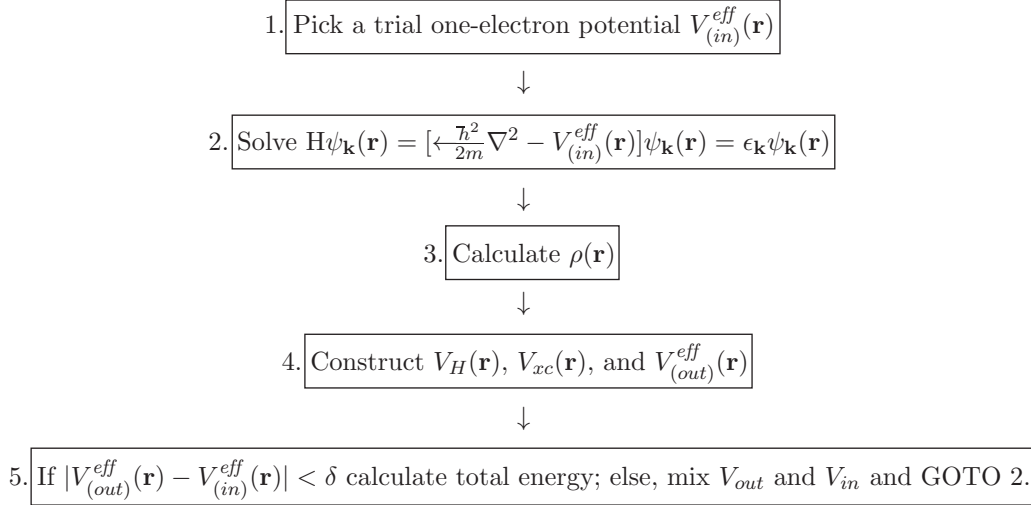
Figure 6. Flow chart describing the computational procedure for the self-consistent calculation of the total energy of a solid.

exchange-correlation energy per electron in an electron gas of *uniform* spin densities $\rho_\uparrow$, $\rho_\downarrow$, namely,

$$E^{\mathrm{LSDA}}_{xc}[\rho_\uparrow, \rho_\downarrow] = \int d^3r\rho(\mathbf{r})\epsilon^{unif}_{\mathbf{xc}}(\rho_\uparrow(\mathbf{r})\rho_\downarrow(\mathbf{r})) \tag{70}$$

The LSDA assumes that the exchange-correlation energy functional is purely local. Several parameterizations exist for the exchange-correlation energy of a homogenous electron gas all of which lead to total-energy results that are very similar [22, 31–33]. These parameterizations use interpolation formulas to link exact results for the exchange-correlation energy of high-density electron gases and calculations of the exchange-correlation energy of intermediate and low-density electron gases. The LDA or LSDA, in principle, ignores corrections to the exchange-correlation energy at a point $\mathbf{r}$ due to nearby inhomogeneities in the electron gas. Considering the inexact nature of the approximation, it is remarkable that calculations performed using the LDA have been so successful. Recent work has shown that this success can be partially attributed to the fact that the LDA gives the correct sum rules for the exchange-correlation hole [34–36].

   A number of attempts to improve the LDA or LSDA use gradient expansions of the charge or spin density. In this way, nonlocal information about the charge or spin density could be provided from the *gradient terms. These type of approximations* are in generally referred to as *gradient expansion approximations* [26]. The most popular, the Perdew-Wang generalized gradient approximation (GGA) [26, 37, 38].

$$E^{\mathrm{GGA}}_{xc}[\rho_\uparrow, \rho_\downarrow] = \int d^3rf(\rho_\uparrow, \rho_\downarrow, \nabla\rho_\uparrow, \nabla\rho_\downarrow) \tag{71}$$

starts from the second-order gradient expansion of the exchange-correlation hole density, then cuts off the spurious long-range ($|\mathbf{r} - \mathbf{r}'| \to \infty$) parts to restore the sum rules. The GGA is typically more accurate than LSD, especially for the rapidly-varying densities of atoms and molecules. In recent years, GGA's have made DFT popular in quantum chemistry.

2.3. Basis Functions

In the discussion of the Kohn-Sham equations earlier, nothing has been said about the way $\psi_{\mathbf{k}}(\mathbf{r})$ itself will be determined. Many methods share the common feature that the wave function is presumed to exist as a linear combination of some set of basis functions which might be written generically as

$$\psi(\mathbf{r}) = \sum_{\mathbf{n}} \alpha_{\mathbf{n}}\phi_{\mathbf{n}}(\mathbf{r}) \tag{72}$$

where α_n is the weight associated with the nth basis function $\phi_n(\mathbf{r})$. The solution of the Kohn-Sham equations in turn becomes a search for unknown coefficients rather than unknown functions. Part of the variety associated with the many different implementations of DFT codes is associated with the choice of basis functions and the form of the effective crystal potential. In deciding on a particular set of basis functions, a compromise will have to be made between high-accuracy results, which require a large basis set, and computational costs, which favor small basis sets. Similar arguments hold with respect to the functional forms of the $\phi_n(\mathbf{r})$. There are several powerful techniques in electronic structure calculations.

The various methods may be divided into those which express the wave functions as linear combinations of some *fixed* basis functions, say linear combination of atomic orbitals (LCAO) localized about each atomic site [39] or those that use free-electron-like basis, the so-called plane-wave basis set [28, 40].

Alternatively, there are those methods that employ *matching* of partial waves, such as the full potential linear augmented plane wave (FLAPW) method [41], the full potential linear muffin-tin-orbital (FLMTO) method [42, 43], and the full potential Korringa-Kohn-Rostoker (KKR) method [44].

2.4. Limitations of the DFT

Density functional theory within the LSDA and GGA generally work well for ground-state properties of moderately correlated electron systems. In some systems, however, the correlations among the electrons are stronger than might be expected from the local spin densities. This occurs in systems where the electrons partially preserve their localized atomic-like nature, as in the case for $4f(5f)$-states in rare-earth (actinide) atoms and sometimes for $3d$-states of transition metal atoms. Typical examples include rare-earth metals, where LDA predicts a strong peak of $4f$-orbital origin in the density of states at the Fermi level, which is in disagreement with experiment, and certain insulating transition metal oxides, which LDA predicts to be metallic. Other systems with anomalous electronic and magnetic properties are heavy-fermion compounds, copper-oxides based superconductors, colossal magnetoresistance manganites, and so forth. In the past few years, there is a growing sense that realistic LDA-like approaches may be generalized to include the most significant correlation effects for strongly correlated electron systems of the Mott-Hubbard and charge-transfer variety [45]. All these approaches are based on LDA as a starting point and introduce additional terms intended to treat Coulomb correlations between electrons. Among these are the LDA + U method [46, 47], the self-interaction correction (SIC) method [33, 48], the LDA + dynamical mean field theory (DMFT) method [49], and the optimized effective potential (OEP) method [50].

In addition, only limited information about spectroscopic properties is available from such ground-state calculations. Quasiparticle (QP) excitations, as they occur in photoemission and tunneling experiments, are not fully described by the Kohn-Sham eigenvalues. In fact, the band structures given by the LDA are often in distinct disagreement from experimental data, showing systematic deviations of band dispersions and band gaps. In addition to the failures of the band structure, two-particle excitations are also not obtained with satisfying accuracy. In particular, optical spectra, which correspond to electron-hole excitations in the electronic system, cannot be described by straight forward use of DFT or other ground-state theories. A time-dependent extension of DFT [50] can treat excitation properties, but so far the method is limited to finite systems. Excitation properties have also been studied using the Configuration Interaction (CI) method [51], but similarly, this method is very much restricted to small systems such as small molecules or clusters. A major achievement in the field was given by the GW approximation (GWA) [52] for the self-energy, which allows for a very accurate evaluation of the self-energy on the basis of results from a preceding DFT calculation. Highly accurate band structures for real materials have been obtained by this method, including bulk semiconductors, insulators, metals, semiconductor surfaces, atoms, defects, and clusters, thus making the GWA a standard tool in predicting the electronic quasiparticle spectrum of moderately correlated electron systems [53].

2.5. Linear Scaling Electronic Structure Methods

A wealth of efficient methods, the so-called O(N) methods, have recently been developed [54–57] for calculating electronic properties of an extended system that require an amount of computation that scales linearly with the size of the system N. On the contrary, the widely used Carr-Parinello [27] molecular dynamics methods and various minimization techniques [28] are limited because the computational time required scales as N^3, where N can be defined to be the number of atoms or the volume of the system. Thus, these methods are an essential tool for the calculation of the electronic structure of large systems containing many atoms. Most O(N) algorithms are built around the density matrix or its representation in terms of Wannier functions [58] and take advantage of its decay properties. To obtain linear scaling, one has to cut off the exponentially decaying quantities when they are small enough. This introduces the concept of a localization region. Only inside this localization region is the quantity calculated; outside it is assumed to vanish. For simplicity the localization region is usually taken to be a sphere, even though the optimal shape might be different.

O(N) methods have become as essential part of most large-scale atomistic simulations based on either tight-binding or semiempirical methods. The use of O(N) methods within DFT methods is not yet widespread. All the algorithms that would allow us to treat very large basis sets within DFT have certain shortcomings. An illustration of the wide range of areas where O(N) methods have made possible the study of systems that were too big to be studied with conventional methods include the 90° partial dislocation in silicon [59], the surface reconstruction properties of silicon nanobars [60], the molecular crash simulation of C_{60} fullerenes colliding with a diamond surface [61], the irradiation-mediated knockout of carbon atoms from carbon nanotubes [62], and the geometric structure of large biomelecules [63].

3. COMPUTATIONAL METHODS FOR ATOMISTIC SIMULATIONS

3.1. Basic Concepts of Statistical Mechanics

The *ab initio* methods presented in the previous section are quite reliable in predicting many properties at the nanoscale. However, they are currently limited to systems containing a few hundred atoms. Such methods serve two important purposes. First, they provide direct information on the response of materials to external environments (e.g., force and temperature). Second, they also generate a database of properties that can be used to construct effective (*empirical*) interatomic potentials. To determine the properties of an ensemble of atoms larger than what can be handled by computational quantum mechanics, the description of the atomic interactions must be approximated. The *molecular dynamics* (MD) method is developed to enable studies of the properties of material volumes containing millions to billions of atoms with effective interatomic potentials. The basic idea is to eliminate all electronic degrees of freedom, and assume that the electrons are *glued* to the nuclei. Thus, the interaction between two atoms is represented by a *potential* function that depends on the atomic configuration (i.e., relative displacement) and the local environment (i.e., electrons). Based on the electronic structure database, or alternatively using experimental measurements of specific properties, approximate effective potentials can be constructed. According to classical Newtonian mechanics, the dynamic evolution of all atoms can be fully determined by numerical integration. In principle, once the positions and velocities of atoms in the finite ensemble within the simulation cell are known, all thermodynamic properties can be readily extracted. Before we present a review of the methods used to simulate statistical ensembles of atomic systems at larger length scales, such as the molecular dynamics and Monte Carlo methods, we will first discuss some basic aspects of statistical mechanics. We will also briefly review some of the most popular interatomic potentials employed in these atomistic simulations.

A statistical "ensemble" of simulated atoms contains atoms that are members of a desired macrostate. This often defined by thermodynamic variables or constraints, such as temperature or pressure. Many equivalent ensembles can be constructed with different microstates,

but with the same thermodynamic constraints of the macrostate. An ensemble is descried by the macroscopic thermodynamic constraints, as follows:

1. A *microcanonical* ensemble is that where the internal energy, volume, and number of atoms are specified, and the system is isolated from its surroundings.
2. A *canonical* ensemble is one in which the temperature, volume, and number of atoms are specified, and the system can exchange only heat with the surroundings.
3. A *grand canonical* ensemble is one in which the temperature, volume, and chemical potential are specified, and the system can exchange heat and atoms with the surroundings.

Consider an isolated system of atoms that has internal energy U, and that it can be divided into two parts that can communicate only heat. The internal energy of the first part is E, while that of the second part is E_r, such that $U = E + E_r$. The density of states of the first part is $\omega(E)$, and that of the second part is $\omega_r(E_r)$. Thus, the total number of microstates in the composite system is: $\omega(E)\omega_r(E_r)dE\,dE_r$. Because U is constant, the product representing the total number of states will have a maximum for a particular value of the energy E, and such state would represent thermodynamic equilibrium. Taking the logarithm of the product, and differentiating with respect to E, we find that the maximum occurs when:

$$\frac{\partial \ln \omega(E)}{\partial(E)} = \frac{\partial \ln \omega_r(E_r)}{\partial(E_r)} \tag{73}$$

The two sides of Eq. (73) define a common property of each subsystem, which is now the temperature, within a constant (i.e., Boltzmann's constant).

$$\frac{\partial \ln \omega(E)}{\partial(E)} = \frac{1}{kT} \tag{74}$$

Now, if we take one of the two parts of the total system to contain precisely one state at an energy E_i, then the probability of finding the small subsystem in a microstate of energy E_i is:

$$P_i = \frac{\omega_r(U - E_i)}{\sum_i \omega_r(U - E_i)} \tag{75}$$

Because $E_i \ll U$, then we can expand:

$$\ln[\omega_r(U - E_i)] = \ln[\omega_r(U)] - \frac{\partial \ln \omega_r}{\partial U}E_i + \cdots \tag{76}$$

and to first order, we have:

$$\omega_r(U - E_i) = \omega_r(U)e^{-E_i/kT} \tag{77}$$

and finally, the probability P_i in Eq. (75) takes the form:

$$P_i = \frac{e^{-E_i/kT}}{Z}; \quad Z = \sum_i e^{-E_i/kT} \tag{78}$$

where Z is defined as the *partition function*, defined as the sum of Boltzmann's factors for all possible microstates of the N-atom system at specified temperature and volume. The concept of the partition function is very powerful, and connects the microstates (obtained, for example, from MD or MC simulations), and the macrostate. For example, the total internal energy of the system of atoms is given by:

$$U = \sum_i E_i P_i = \frac{1}{Z}\sum_i E_i e^{-E_i/kT} \tag{79}$$

Because the partition function is a thermodynamic property, it will generally depend on two variables (say temperature and volume in the canonical ensemble case we are considering). This property can be used to evaluate the summation in Eq. (78), thus, we have:

$$\left(\frac{\partial Z}{\partial T}\right)_V = \frac{1}{kT^2}\sum_i E_i e^{-E_i/kT} \tag{80}$$

and

$$U = \frac{kT^2}{Z}\left(\frac{\partial Z}{\partial T}\right)_V = kT^2\left(\frac{\partial \ln Z}{\partial T}\right)_V \tag{81}$$

The entropy, S, of the canonical ensemble is defined as the ensemble average of $\ln P_i$, thus:

$$S = -k\left[\sum_i\left(\frac{e^{-E_i/kT}}{Z}\right)\left(-\frac{E_i}{kT}\right) - \sum_i\left(\frac{e^{-E_i/kT}}{Z}\right)\ln Z\right] \tag{82}$$

which, when written in terms of the partition function, gives:

$$S = k\ln Z + kT\left(\frac{\partial \ln Z}{\partial T}\right)_V \tag{83}$$

Other thermodynamic functions can be readily obtained from the partition function. The Helmholtz energy, A, is simply obtained as:

$$A = U - TS = -kT\ln Z \tag{84}$$

and as the pressure P is related to the Helmholtz energy as $P = -(\partial A/\partial V)_T$, then we can obtain the system pressure as:

$$P = kT\left(\frac{\partial \ln Z}{\partial V}\right)_T \tag{85}$$

Finally, it can be easily shown from basic definitions that the enthalpy, H and the Gibbs free energy G can be obtained easily from the partition function, as:

$$H = U + PV = kT\left[T\left(\frac{\partial \ln Z}{\partial T}\right)_V + V\left(\frac{\partial \ln Z}{\partial V}\right)_T\right]$$
$$G = H - TS = -kT\ln Z + VkT\left(\frac{\partial \ln Z}{\partial V}\right)_T \tag{86}$$

3.2. Interatomic Potentials

3.2.1. Connections Between Quantum and Approximate Potentials

The direct use of DFT methods to perform full quantum molecular-dynamics simulations on real materials is limited to a hundred or so atoms and a few picoseconds of simulation time. Thus, the next step of coarse-graining the problem is to remove the electronic degrees of freedom by imagining the atoms to be held together by some sort of glue or interatomic potential, thereby allowing large scale atomistic simulations for millions of atoms and nanoseconds of simulation time. Such simulations, employing approximate (or empirical) interatomic potentials, have been extremely useful in investigating generic phenomena in simple systems. Empirical potentials involve the fitting of parameters to a predetermined experimental or *ab initio* database, which includes physical quantities such as the lattice constant, the bulk modulus and elastic constants, the vacancy formation energy, the surface energy, and so forth. The goodness of the potential is determined by fitting to a small set of properties and then accurately predicting other properties not within the set used for fitting its parameters. However, at the same time, they may not provide the desired physical accuracy for many real complex materials of interest. For example, reliable interatomic potentials are not usually available for multielement materials and for systems containing

substitutional or interstitial alloying impurities. Interatomic potentials used in MD simulations may generally be classified into three broad categories: (1) pair potentials; (2) effective medium potentials; and (3) quantum-based potentials. In *pair potentials*, the electronic DOF are totally eliminated, and are glued to nuclear DOF, thus atoms are represented by coordinates and momenta only. When electronic DOF are averaged out and included into an electronic density function that depends on the local environment of the atom, we have what is known as *effective medium potentials*. Implicit recognition of the electronic DOF is given through the embedding function. Further recognition of the electronic DOF is achieved through the introduction of reduced sets of coefficients based on quantum mechanics in *quantum-based potentials*. We give here examples of interatomic potentials belonging to the three main categories.

3.2.2. Pair Potentials

Pair potentials are constructed such that the electronic DOF are elimnated, and the exact energy of the system, E_{exact} is replaced by an approximate energy function, E_{approx}. Thus, we map the energy function of the system's nuclear, $\mathbf{R}_i$, and electronic, $\mathbf{r}_i$, coordinates, such that:

$$E_{\text{exact}}(\{\mathbf{R}_i, \mathbf{r}_i\}) \longrightarrow E_{\text{approx}}(\{\mathbf{R}_i\}) \tag{87}$$

Two common examples of pair potentials are the Lennard-Jones [64] and the Morse [65] potentials:

1. **The Lennard-Jones Potential** [64]. The Lennard-Jones potential is sometimes used to model the interatomic interaction in solids, although it is best fit to the behavior of gases or fluids. The potential is given by:

$$V(R) = -\frac{A}{R^{12}} + \frac{B}{R^6} \tag{88}$$

where A and B are constants, determined by matching independent physical properties. For example, if the equilibrium lattice constant in Cu is 0.36 nm, and its shear modulus is 50 GPa, let's see how one can determine the two A and B.

$$E(R) = -\frac{A}{R^{12}} + \frac{B}{R^6}, \qquad F = -\nabla E = -\frac{12A}{R^{13}} + \frac{6B}{R^7} \tag{89}$$

We now t take equilibrium distance to be the lattice constant $= 3.6 \times 10^{-10}$ m, where the force should be zero. This gives: $B = 2A/R_0^6$. We can assume that the approximate area per atom $= \approx \pi R_0^2$, then:

$$\sigma = \frac{\Delta F}{\pi R_0^2} = E\varepsilon = E\frac{\Delta R}{R}\bigg|_{R_0} = E \simeq \frac{1}{\pi R_0}\frac{\partial F}{\partial R} \tag{90}$$

However, $E = 2(2+\nu)\mu = 1.34 \times 10^{-11}[\text{Pa}] = (\pi R_0)/\{\frac{156A}{R_0^{14}} - \frac{42B}{R_0^8}\}$.

Now, solving for A and B, we obtain: $A = 1.38 \times 10^{-132}$ and $B = 1.17 \times 10^{-69}$.

2. **The Morse Potential** [65]. This potential, $E(R)$, is characterized by three parameters: ϵ, a, and R_0, and is given by:

$$E(R) = \varepsilon\big[e^{-2a(R-R_0)} - 2e^{-a(R-R_0)}\big] \tag{91}$$

Compared with the simpler Lennard-Jones potential, the repulsion term here is more realistic, but the attraction is less so. Furthermore, there is an extra parameter a, which can be used to fit a third property. We can fit, for example, the lattice constant ,R_0, the bulk modulus B, and the cohesive energy E_{coh}, using the three conditions:

$$\left[\frac{dE}{dR}\right]_{R_0} = 0 \tag{92}$$

$$B = -V\frac{dP}{dV} = V\frac{\partial^2 E}{\partial V^2} \tag{93}$$

$$E_{\text{coh}} = [E]_{R_0} \tag{94}$$

The Morse potential may be written as:

$$E(R) = \zeta(\zeta - 2), \quad \text{and} \quad \zeta = \exp\left[\rho\left(1 - \frac{R}{R_0}\right)\right] \tag{95}$$

where ε, ρ, and R_0 are adjustable parameters that determine the shape of the potential. First, ε adjusts the depth of the potential (i.e., the binding energy), R_0 adjusts the equilibrium interatomic separation, and ρ adjusts the range of the potential. This is shown in Fig. 7. Recently, an intermolecular potential for Bucky balls (C_{60} molecules), has been obtained, with an effective value of $\rho = 13.62$. The alkali metals have longer-ranged interactions, for example $\rho = 3.15$ has been suggested for sodium, while $\rho = 3.96$ for nickel. Take the case of two isolated atoms, separated by 0.4 nm at equilibrium and have a cohesive energy of (-5 eV). Then, $\varepsilon = -5$ eV, $R_0 = 0.4$ nm.

3.2.3. Effective Medium Potentials

This class of potentials include the embedded-atom (EAM) type [66, 67] or the Finnis-Sinclair (FS) type [68] potentials for metals that do not exhibit directional bonding character, and the Stillinger-Weber (SW) type [69, 70] or the Tersoff type [71] potentials in covalent materials, where the potential depends on the bond angle. In these types of potentials, we treat the electronic degrees of freedom as a class of total energy functionals known as effective medium and angular force schemes to incorporate environmental and angular dependencies. Thus, we map the exact potential to an approximate representation as:

$$E_{\text{exact}}(\{\mathbf{R}_i, \mathbf{r}_i\}) \longrightarrow E_{\text{approx}}(\{\mathbf{R}_i, \mathbf{r}_i\}) \longrightarrow E_{\text{approx}}[\rho(\mathbf{r}_i), \{\mathbf{R}_i\}] \tag{96}$$

Approximate embedding potentials divide the energy into two contributions, one from core-core repulsion that can be of a Coulomb or screened Coulomb type, while the second part represents the energy cost for embedding an ion in a uniform electron gas, of local density ρ. *Ab initio* calculations have shown that the electronic component of the embedding energy shows a minimum that is dependent on the type of embedded ion. We will discuss now one example of analytical determination of embedded atom potentials. This is followed by the procedure for more accurate numerical determination of the embedded atom method, or EAM for short [66, 67], and finally a different approach for the embedding function based on the Finnis-Sinclair procedure.

1. **The Johnson Potential: An Analytical Approach to EAM** [72]. In the EAM, all atoms are viewed as embedded in the host consisting of all other atoms [73], and the total energy is divided into an embedding energy, which is electron-density dependent, and
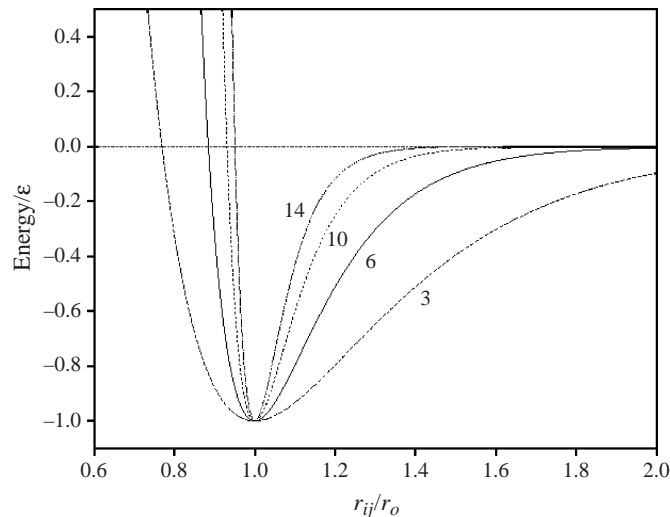
Figure 7. The three-parameter Morse potential.

pair contributions. Various functional forms are developed on the basis of known experimental or *ab initio* data:

$$E_{\text{tot}} = \frac{1}{2} \sum_{ij} \phi(R_{ij}) + \sum_i F(\rho_i)$$

$$F(\rho) = E_{\text{embed}}$$

$$\rho(i) = \sum_{j \neq i} f(R_{ij}) \tag{97}$$

$$\phi_{ij}(R) = \frac{Z_i(R)Z_j(R)}{R}$$

$\phi_{ij}(R)$ is the pair-interaction potential, which is usually taken as screened Coulomb, while $F(\rho)$ is the embedding energy.

Based on extensive experimental data and first principles calculations, the total energy was found to be a function of the interatomic separation (a), in a simple form, known as the universal binding energy relation (UBER) [74], and given by:

$$E_{\text{tot}}(a) = -E_{\text{sub}}(1 + a^*)e^{-a^*}$$

$$a^* = \frac{(a/a_0 - 1)}{(E_{\text{sub}}/9B\Omega)^{1/2}} \tag{98}$$

Here, E_{sub} is the absolute value of the sublimation energy at zero temperature and pressure. a^* is a measure of the deviation from the equilibrium lattice constant. B is the bulk modulus of the material, a is a length scale characteristic of the condensed phase, which we will take to be the fcc lattice constant, a_0 is the equilibrium lattice constant, and Ω is the equilibrium volume per atom.

An analytical procedure was developed by [72], where the interatomic potential is obtained analytically. In this procedure, the embedding function is deduced as the difference between the total energy as given by the UBER and the total contributions of the pair part of the potential. For an fcc metal, the energy of a given atom (without double counting, since the fcc structure has 12 nearest neighbors) is E_i, given by:

$$E_i = F(\rho_i) + 6\phi(R_{nn}) \tag{99}$$

where R_{nn} is the equilibrium distance of the nearest neighbor, ϕ is the pair potential, F the embedding function, and ρ_i the total electron density at atom i. If we rely on our knowledge of the universal binding energy relationship, we can immediately deduce the embedding function as follows:

$$F[\rho(R)] = E_{\text{tot}}(R) - 6\phi(R) \tag{100}$$

Johnson assumed the following forms for $\rho(R)$ and $\phi(R)$:

$$\rho(R) = fe^{-\beta(R/R_0 - 1)} \tag{101}$$

$$\phi(R) = \phi_0 e^{-\gamma(R/R_0 - 1)} \tag{102}$$

where f, β, ϕ_0 and γ are constants. With these forms, the embedding function can be analytically obtained, and is given by:

$$F(\rho) = -E_c\left(1 - \frac{\alpha}{\beta}\ln\frac{\rho}{\rho_0}\right)\left(\frac{\rho}{\rho_0}\right)^{\alpha/\beta} - 6\phi_0\left(\frac{\rho}{\rho_0}\right)^{\gamma/\beta} \tag{103}$$

Force calculations in MD simulations must take into account the implicit dependence of the embedding function on interatomic distances. The force on the ith atom due to the embedding function is given by:

$$\mathbf{f}_i = -\sum_{i \neq j}(F'(\rho_j)\rho_i' + F'(\rho_i)\rho_j')\widetilde{\mathbf{R}}_{ji} \tag{104}$$

where $\widetilde{\mathbf{R}}_{ji}$ is the unit vector connecting the ith and jth atoms.

2. **The Daw-Baskes Potential: A Numerical Approach to EAM** [66, 67]. In this widely used numerical procedure developed by Daw and Baskes, the electron density is approximated by the superposition of atomic densities

$$\rho_i = \sum_{j \neq i} \rho_j^a(R_{ij}) \tag{105}$$

where $\rho_j^a(R)$ is the electron density contributed by atom j and computed from the Hartree-Fock wave functions by

$$\rho^a(r) = N_s \rho_s^a(r) + N_d \rho_d^a(r)$$
$$\rho_s^a(r) = \frac{|\sum_i C_i \psi_i(r)|^2}{4\pi} \tag{106}$$
$$\psi_i(r) = \frac{(2\xi_i)^{(n_i+1/2)}}{[(2n_i)!]^{1/2}} r^{n_i-1} e^{-\xi_i r}$$

where n_s and n_d are the number of outer s and d electrons, respectively, and ρ_s and ρ_d are the densities associated with the s and d wave functions. The pair interaction can be written in terms of effective charges as:

$$\phi_{ij}(r) = \frac{Z_i(r)Z_j(r)}{r}$$
$$Z(r) = Z_0(1 + \beta r^\nu)e^{-\alpha r} \tag{107}$$

The embedding energy can be uniquely defined by requiring that the total energy of the homogeneous fcc solid, computed using Eq. (97) to agree with the universal equation of state given by Eq. (98). For a concrete example, let us consider the procedure to evaluate the EAM potential for Ni. The wave function and other parameters for Ni and Cu are given in Tables 1 and 2. Once the geometry surrounding an atom is defined (i.e., distances and positions of nearest neighbors), Eq. (98) is used to determine the total energy. The effective charges are then calculated and used to determine the pair part of the potential, using Eq. (107). Now, we calculate the wave functions and their contributions to the s- and d-bands for the electron density, using Eqs. (106) and (105). The value of the embedding energy is calculated from Eq. (97). Thus, we can create a numerical relationship between the electron density and the embedding energy, which would be equivalent to what Johnson assumed in Eq. (103). Forces can be evaluated using Eq. (104), and the procedure repeated for all atoms in the MD simulation cell.

3. **The Finnis-Sinclair Potential** [68]. An embedding potential introduced by [68] incorporates the band character of metallic cohesion. Finnis and Sinclair replaced the charge Z in tight-binding treatments with the sum of functions representing the valence electrons. The form of the potential is a balance between this attractive contribution and core repulsion. One form of the potential is given by:

$$E = E_n + E_e = \frac{1}{2}\sum_{ij} \phi_{ij}(R_{ij}) - \sum_i \sqrt{\rho_i} \tag{108}$$

Table 1. EAM parameters for Ni and Cu.

	Z_0	r	β	ν	n_s	Atomic configuration
Cu	11.0	1.7227	0.1609	2	1.000	$3d^{10}4s^1$
Ni	10.0	1.8633	0.8957	1	1.5166	$3d^8 4s^2$

Table 2. EAM wave function parameters for Ni.

i	n_i	ξ_i	C_i
4s			
1	1	54.88885	−0.00389
2	1	38.48431	−0.02991
3	2	27.42703	−0.03189
4	2	20.88204	0.15289
5	3	10.95707	−0.20048
6	3	7.31958	−0.05423
7	4	3.92650	0.49292
8	4	2.15289	0.61875
3d			
1	3	12.67582	0.42120
2	3	5.43253	0.70658

The electron density for each atom is given by:

$$\rho_i = \sum_{i \neq j} \rho(R_{ij}) \tag{109}$$

$$\text{where} \quad \rho(R_{ij}) = \begin{cases} (R_{ij} - d)^2, & R_{ij} < d \\ 0, & R_{ij} > d \end{cases} \tag{110}$$

Potentials with Angular Dependence   The embedding-type potentials are applicable to metals that do not exhibit strong directional bonding character. However, in covalently-bonded solids, such as Si and SiC, the crystal structure is not closed packed, but is rather open. Certain angles between bonds designate the equilibrium nature of the open structure. Empirical interatomic potentials have been developed to reflect this fact, and the following two are among the most popular.

1. **Stillinger-Weber Angular Potential** [69]. In the Stellinger-Weber potential, the total energy is expanded in terms of two-body V_2 and three-body V_3 contributions.

$$E_{\text{tot}}(\{\mathbf{R}_i\}) = \frac{1}{2} \sum_{i,j} V_2(R_{ij}) + \frac{1}{3!} \sum_{i,j,k} V_3(\mathbf{R}_i, \mathbf{R}_j, \mathbf{R}_k) \tag{111}$$

The two-body (pair potential) contribution to the total energy is given by a function of scaled interatomic distances

$$V_2(R_{ij}) = \epsilon f_2\left(\frac{R_{ij}}{\sigma}\right) \tag{112}$$

while the three-body contribution is expressed as a function of three vectors connecting between triplets of three atoms as

$$V_3(\mathbf{R}_i, \mathbf{R}_j, \mathbf{R}_k) = \epsilon f_3\left(\frac{\mathbf{R}_i}{\sigma}, \frac{\mathbf{R}_j}{\sigma}, \frac{\mathbf{R}_k}{\sigma}\right) \tag{113}$$

$$f_2(R) = \begin{cases} A(BR^{-p} - R^{-q})e^{[(r-a)^{-1}]} & \text{if } r < a \\ 0 & \text{otherwise} \end{cases} \tag{114}$$

$$f_3(\mathbf{R}_i, \mathbf{R}_j, \mathbf{R}_k) = h(R_{ij}, R_{ik}, \theta_{jik}) + h(R_{ji}, R_{jk}, \theta_{ijk}) + h(R_{ki}, R_{kj}, \theta_{ikj}) \tag{115}$$

$$h(R_{ij}, R_{ik}, \theta_{jik}) = \lambda e^{[\gamma(R_{ij}-a)^{-1} + \gamma(R_{ik}-a)^{-1}]}\left(\cos\theta_{jik} + \frac{1}{3}\right)^2 \tag{116}$$

The key ingredient in this formulation is the angular function h, which is selected to be a function of the angle θ_{jik} between the vectors $\mathbf{R}_{ji}$ and $\mathbf{R}_{jk}$. λ, a, γ, A, B, and q are fitting constants. It is noted that the angular term is minimized for $\theta \approx 109.47°$, corresponding to the tetrahedral angles that characterize the sp^3 bonds of covalent materials.

2. **Tersoff Cluster Functionals (1988)** [71]. The Stellinger-Weber potential does not have explicit functional dependence on the embedding environment for participating atoms. [71] was the first to develop Si potentials that account for environmental dependence. The total energy in his potential takes the form:

$$E_{\text{tot}} = \frac{1}{2} \sum_{ij} \left[V^r(R_{ij}) + b_{ij} V^a(R_{ij}) \right] \tag{117}$$

where the repulsive potential is given by

$$V^r(R_{ij}) = A e^{-\lambda_1 R_{ij}} \tag{118}$$

and the attractive potential by

$$V^a(R_{ij}) = B e^{-\lambda_2 R_{ij}} \tag{119}$$

The environmental and angular dependence enter the potential through the function b_{ij}

$$b_{ij} = (1 + \beta^n \xi_{ij}^n)^{-1/2n} \tag{120}$$

where the function ξ_{ij} is given by

$$\xi_{ij} = \sum_{k \neq ij} f_c(R_{ik}) g(\theta_{ijk}) \tag{121}$$

and $f_c(R)$ is a cutoff function that smoothly decreases from $1 \to 0$ as $R \to R_c$. The function $g(\theta_{ijk})$ contains the angular dependence, and takes the form

$$g(\theta) = 1 + \frac{c^2}{d^2} - \frac{c^2}{d^2 + (h - \cos\theta)^2} \tag{122}$$

3.2.4. Quantum-Based Potentials: The Tight-Binding Method

There is a growing need to develop more accurate interatomic potentials, derived from quantum mechanics, that can be applied to large-scale atomistic simulations. This is especially so for directionally-bonded systems, such as transition metals, and for chemically or structurally complex systems, such as intermetallic compounds and alloys. The tight-binding [75, 76] and the self-consistent-charge density functional tight-binding molecular dynamics (TBMD) approach is becoming widespread in the atomistic simulation community, because it allows one to evaluate both ionic and electronic properties [77]. The success of TBMD stands on a good balance between the accuracy of the physical representation of the atomic interactions and the resulting computational cost. TBMD implements an empirical parameterization of the bonding interactions based on the expansion of the electronic wave functions on a very simple basis set. Recently, novel analytic bond-order potentials have been derived for atomistic simulations by coarse-graining the electronic structure within the orthogonal two-center tight-binding representation [78–80]. Quantum-based interatomic potentials for transition metals that contain explicit angular-force contributions have been developed from first-principles, DFT-based generalized pseudopotential theory [81–83].

The basic idea of the tight-binding method is that the electronic wave function of the solid can be built up as a linear combination of the atomic wave functions centered on the atoms, following the solution procedure of the Schrödinger equation for the hydrogen molecule. The coefficients of the basis functions, $\alpha_{i\beta}$, are selected such that the total energy is a minimum. The eigenvalues of the resulting Hamiltonian matrix are the electronic contribution to the total energy. The method results in two main aspects: (1) the total energy of the system can be calculated directly without separation into pair potentials and embedding energy; and (2) it gives the form of the pair functionals and angular forces.

The electronic degrees of freedom are thus incorporated by the mapping

$$E_{\text{exact}}(\{\mathbf{R}_i, \mathbf{r}_n\}) \longrightarrow E_{\text{approx}}(\{\mathbf{R}_i, \alpha_i\}) \tag{123}$$

where $\{\alpha_i\}$ are expansion coefficients that characterize the electronic wave function. The solid is assumed to be formed by bringing its atoms into close proximity such that the atomic energy levels of outer valence electrons are distributed as a result of the overlap between the wave functions of adjacent atoms. We postulate a wave function for the total solid of the form

$$\psi_r = \sum_{i=1}^{N} \sum_{\alpha=1}^{n} a_{i\alpha} \phi_\alpha(r - R_i) \tag{124}$$

or, written in a more compact form

$$|\psi\rangle = \sum_{i=1}^{N} \sum_{\alpha=1}^{n} a_{i\alpha} |i, \alpha\rangle \tag{125}$$

The outer sum runs over the number of atoms, N, in the solid, while the inner sum runs over the number of orbitals per site. The representation of the wave function, $|i, \alpha\rangle = \phi_\alpha(r - R_i)$ is for the α orbital on site i. For the case of Si, for example, we make our expansion for the 3s and 3p electrons only, with no contributions from inner shell electrons. The procedure attempts to find the minimal set of wave functions, with no attempt for completeness. Now we write the energy functional, Π, as a function of the wave function, ψ, or, as a function of the unknown expansion coefficients

$$\Pi(\{a_{i\alpha}\}) = \langle\psi|\widehat{H}|\psi\rangle - E\langle\psi|\psi\rangle \tag{126}$$

Substituting now for the total wave function [Eqs. (124) and (125)], we have

$$\Pi(\{a_{i\alpha}\}) = \sum_{i,\,j=1}^{N} \sum_{\alpha,\,\beta=1}^{n} \left(h_{ij}^{\alpha\beta} - E S_{ij}^{\alpha\beta}\right) a_{i\alpha}^* a_{j\beta} \tag{127}$$

where the matrices, $h_{ij}^{\alpha\beta}$, and $S_{ij}^{\alpha\beta}$ are given by

$$h_{ij}^{\alpha\beta} = \langle i, \alpha|\widehat{H}|j, \beta\rangle = \int_\Omega \phi_\alpha^*(\mathbf{r} - \mathbf{R}_i)\widehat{H}\phi_\beta(\mathbf{r} - \mathbf{R}_j)\, d^3\mathbf{r}$$

and

$$S_{ij}^{\alpha\beta} = \langle i, \alpha|j, \beta\rangle = \int_\Omega \phi_\alpha^*(\mathbf{r} - \mathbf{R}_i)\phi_\beta(\mathbf{r} - \mathbf{R}_j)\, d^3\mathbf{r} \tag{128}$$

The matrix $S_{ij}^{\alpha\beta}$ represents the degree of overlap between wave functions of adjacent sites, and is hence called the overlap matrix. If the wave function basis set is selected to be orthogonal, then $S_{ij}^{\alpha\beta} = \delta_{ij}\delta\alpha\beta$. Once the Hamiltonian matrix is formed [Eq. (127)], the unknown coefficients $a_{i\alpha}$ can be obtained by minimization, thus

$$\frac{\partial\Pi}{\partial a_{i\alpha}^*} = 0$$

or

$$\sum_{k'}(H_{kk'} - E\delta_{kk'})a_k = 0 \tag{129}$$

where the super index k runs from 1 to nN. Solution of the set of nN Eqs. (129) results in a set of energy eigen values, $E_k \equiv E_{i\alpha}$, and a set of coefficients $a_k \equiv a_{i\alpha}$ that determine the total wave function itself.

Evaluation of the matrix elements is usually done by the so-called two-center approximation, where contributions to the $h_{ij}^{\alpha\beta}$ arise only from the potential of two neighboring atoms i and j, $V_{atom}(\mathbf{r} - \mathbf{R}_i)$ and $V_{atom}(\mathbf{r} - \mathbf{R}_j)$, respectively. Each matrix element depends on the separation distance and orientation vector between two neighboring atoms. Because p-orbitals are spherically symmetric, and p-orbitals have single lobes of the wave functions, oriented along x (p_x), y (p_y) or z (p_z), then various symmetries should arise in coupling

factors, V, within the matrix elements. For example, if the azimuthal rotational symmetry direction of individual atoms is aligned with the bond direction, we would have the so-called σ-bond. This may arise because of coupling between two s-orbitals, two p-orbitals, and so forth and we would have factors like $V_{ss\sigma}$, $V_{pp\sigma}$, and so forth. On the other hand, π-bonds are denoted for couplings of orbitals such that the azimuthal symmetry directions of individual atoms are normal to bond direction. Such is the case when we consider two p_z-orbitals of two neighboring atoms connected along the x-axis.

Solution of the eigenvalue problem stated above results in a spectrum of energies that covers a wide span, and can be best represented as a *histogram* of delta functions, known as the electronic density of states (DOS), which takes the form

$$\rho(E) = \sum_i \delta(E - E_i) \tag{130}$$

Thus, the electronic contribution to the total energy is obtained by summing up all eigne values of E, or rather by performing the integral:

$$E_{\text{el}} = 2 \int_{-\infty}^{\epsilon_F} E\rho(E)\, dE \tag{131}$$

the factor of two accounts for up-down electron spin occupancy of each state. The total energy can then be constructed by adding an effective pair potential for the interaction between neighboring nuclei.

$$E_{\text{total}}(\{\mathbf{R}_i\}) = \frac{1}{2} \sum_{ij} V_{\text{eff}}(R_{ij}) + 2 \int_{-\infty}^{\epsilon_F} E\rho(E)\, dE \tag{132}$$

Typical calculations proceed as follows. First, a computational cell is constructed with its set of nuclear coordinates, $\mathbf{R}_i$. Once we have these coordinates, we can determine the elements of the interaction matrix, $h_{ij}^{\alpha\beta}$, which describe the coupling between the αth orbital on site i with the βth orbital on site j. The overlap matrix, $S_{ij}^{\alpha\beta}$, can be similarly determined. The full Hamiltonian is thus known, and we can proceed to find the energy eigen values, and finally determine the DOS, $\rho(E)$.

3.2.4.1. Moments of the Density of States   The density of states is a distribution function of possible electronic energies, up to the Fermi level. The DOS can be characterized by its moments, defined as

$$\mu_n = \int_{-\infty}^{\infty} E^n \rho(E)\, dE \tag{133}$$

where μ_n is the nth moment of the DOS. For example, for d-band bonding, the first moment gives the mean (or energy centroid of the d-band DOS), the 2nd gives the variance or energy width of the d-band DOS, the 3rd represents the skewness of the d-band DOS, and the 4th is for its kurtosis.

Consider and s-band tight-binding application of these ideas, and use the notation $|i, s\rangle = |i\rangle$. Then $\mu_2(i) = \langle i|H^2|i\rangle$. Utilizing the identity $\mathbf{I} = \sum_j |j\rangle\langle j|$, we find the second moment as

$$\mu_2(i) = \sum_j h(R_{ij}h(R_{ij}) \tag{134}$$

where $h(R_{ij}) = \langle i|H|j\rangle$. Similarly, for the third and fourth moment

$$\mu_3(i) = \sum_{jk} h(R_{ij}h(R_{jk})h(R_{ki})$$

$$\mu_4(i) = \sum_{jkl} h(R_{ij})h(R_{jk})h(R_{kl})h(R_{li}) \tag{135}$$

We note here that moments can be written as products of matrix elements over paths starting and ending on the same atom. This observation is stated as the *moments theorem* : the nth moment of the DOS on an atom is determined by the sum over all paths comprised of n steps between neighboring atoms that begin and end on the originating atom.

3.2.4.2. Rectangular Band Model and Pair Functionals A simplification of the tight-binding procedure described earlier is the rectangular band model of the DOS, and provides an understanding of the idea of pair functionals for cohesion in solids. Instead of the tedious calculation of the DOF from its energy eigen values, this model assumes that the DOF is constant over an energy width w, and is zero otherwise. The constant value assigned to the DOS is determined from a known value, N_{full}, which is the total number of electrons that can be accommodated in the band.

$$N_{\text{full}} = 2 \int_{-W/2}^{W/2} \rho(E)\, dE \tag{136}$$

Thus, $\rho(E) = N_{\text{full}}/2W$. We can now determine the electronic contribution to the total energy as a function of filling the band, or the number of electrons, N_e. The electronic contribution to the total energy is

$$E_{\text{el}} = \frac{N_{\text{full}}}{W} \int_{-W/2}^{\varepsilon_F} E\, dE \tag{137}$$

where the Fermi energy ε_F is dependent on band filling

$$N_e = \frac{N_{\text{full}}}{W} \int_{-W/2}^{\varepsilon_F} dE$$
$$\varepsilon_F = W \left(\frac{N_e}{N_{\text{full}}} - \frac{1}{2} \right) \tag{138}$$

which yields for the electronic energy

$$E_{\text{el}} = -\frac{N_{\text{full}} W}{2} \left(\frac{N_e}{N_{\text{full}}} \right) \left(1 - \frac{N-e}{N_{\text{full}}} \right) \tag{139}$$

The cohesive electronic energy is a parabolic function of electron shell filling, maximizing half-way between empty and full shells. This observation is consistent with the experimental data on transition metals. If we apply the simple rectangular band model and calculate the second moment of the DOS function, we find that $\mu_2 = 5W^2/12$, which demonstrates that the width of the band is proportional to the square root of the second moment. The rectangular band model suggests that the total energy can be written as a pair potential for the interaction between nuclei, and an electronic bonding term that is proportional to the second moment. The 2nd moment arises from all "hopping steps" from the atom to its nearest-neighbors and back, which is just the number of nearest neighbors, Z. This gives a binding energy that is proportional to $\sqrt{Z\rho}$, as postulated by the more empirical Finnis-Sinclair potential.

$$E_{\text{tot}} = \frac{1}{2} \sum_{ij} \phi(R_{ij}) - \sum_i \alpha \sqrt{\mu_2(i)} \tag{140}$$

where the constant α depends on band filling, and can be determined from ab initio calculations, or used as a fitting parameter. It is noted that the second moment is of the pairwise additive nature, and like the embedded atom method, the energy per bond will depend on the coordination number Z.

3.2.4.3. Moments and Angular Forces The connection between the moments and angular forces can be revealed by considering an expansion of the total energy in terms of separate potentials for interactions of two-body, three-body, four-body, and so forth. This takes the form

$$E_{\text{tot}} = \frac{1}{2} \sum_{ij} V_2^{\text{eff}}(R_i, R_j) + \frac{1}{3!} \sum_{ijk} V_3^{\text{eff}}(R_i, R_j, R_k) + \frac{1}{4!} \sum_{ijkl} V_4^{\text{eff}}(R_i, R_j, R_k, R_l) + \cdots \tag{141}$$

Let's now consider a reference state for the electronic contribution of the total energy, expressed in terms of the DOS moments in the form

$$E_{el}^{ref} = E(\mu_2^{ref} + \mu_3^{ref}, \ldots, \mu_n^{ref}) = 0 \tag{142}$$

Deviations from this reference state (which can be assigned as the equilibrium state, i.e., $E_{el}^{ref} = 0$) result in changes in the DOS moments. The electronic energy contribution to the total energy changes from E_{el}^{ref} to E_{el}, and takes the form

$$E_{el} = E(\mu_2^{ref} + \delta\mu_2, \mu_3^{ref} + \delta\mu_3, \ldots, \mu_n^{ref} + \delta\mu_n) \tag{143}$$

This form of E_{el} can be expanded in a Taylor series, and the difference in energy expressed as a series of DOS moments

$$E_{el} = \sum_n \left(\frac{\partial E}{\partial \mu_n}\right)_{ref} (\mu_n - \mu_n^{ref}) \tag{144}$$

The energy of a state may then be expressed as

$$E_{el} = \sum_n \left(\frac{\partial E}{\partial \mu_n}\right)_{ref} \sum_{k=1}^{n} \Delta\mu_n^{(k)} \tag{145}$$

The notation $\Delta\mu_n^{(k)}$ is used to represent the partial nth moment (relative to the reference state moment) contributed from paths connecting k atoms. Comparing Eqs. (141) and (145), we conclude that the two expressions would be equivalent, provided

$$V_n^{eff}(R_i, R_j, \ldots, R(n)) = n! \sum_{n=2}^{N_m} \left(\frac{\partial E}{\partial \mu_n}\right)_{ref} \Delta\mu_n(R_i, R_j, \ldots, R(n)) \tag{146}$$

The main aspect of these types of many-body potentials is that contributions to the potential at an atom contributed by doublet, triplet, etc. atom clusters inherit the characteristics of the 2nd, 3rd, etc. moments of the DOS function. This is particularly important for the directional dependence of these moments, as they give rise to angular forces.

3.3. The Molecular Dynamics Method

The basic premise of constructing empirical or semiempirical interatomic potentials is that we can eliminate all electronic degrees of freedom (DOF), thus treating atoms with Newtonian mechanics. In this view of nature, we develop effective methods for dealing with such huge reduction of the DOF by adding extra terms to interatomic interaction potentials. Of course, the validity of these simplified interaction potentials must be checked by ascertaining the accuracy of simulating basic known properties of the material.

The dynamic evolution of a system of atoms is governed by classical Newtonian mechanics, where for each atom (i), the equation of motion is given by:

$$M_i \frac{d^2 \mathbf{R}_i}{dt^2} = \mathbf{F}_i = -\nabla_{R_i} \Phi \tag{147}$$

which is derived from the classical Hamiltonian of the system:

$$\mathcal{H} = \sum_1^N \frac{M_i V_i^2}{2} + \Phi \tag{148}$$

An atom of mass M_i moves as a rigid particle at the velocity V_i in the effective potential of other particles, $\Phi(\mathbf{R_i})$. The atomic force $\mathbf{F}_i$ is obtained as the negative gradient of the effective potential, $\mathbf{F}_i = -\nabla_{R_i}\Phi$. Solving these 2nd order ordinary differential equations or all the atoms in a simulation cell may appear simplistic. A physical simulation involves proper selection of numerical integration scheme, employment of appropriate boundary conditions, and stress and temperature control to mimic physically meaningful thermodynamic ensembles.

The numerical integration scheme, which is performed either by explicit or implicit methods, should be both stable and computationally efficient. The simple Euler scheme is not appropriate for MD simulations because it lacks numerical stability. In the explicit Verlet's leap-frog method, the equation of particle motion is split into two first-order equations:

$$\frac{d\mathbf{R}_i}{dt} = \mathbf{V}_i, \quad \frac{d\mathbf{V}_i}{dt} = \frac{\mathbf{F}(\mathbf{R}_i)}{M_i} \tag{149}$$

Based on the half-step leap-frog method, this set of equations is converted for small time increment δt to:

$$\mathbf{R}_i(t + \delta t) = \mathbf{R}_i(t) + \delta t \mathbf{V}_i\left(t + \frac{1}{2}\delta t\right) \tag{150}$$

$$\mathbf{V}_i\left(t + \frac{1}{2}\delta t\right) = \mathbf{V}_i\left(t - \frac{1}{2}\delta t\right) + \delta t \frac{\mathbf{F}_i}{M_i} \tag{151}$$

The Verlet algorithm is very popular in MD simulations because it is stable, memory-efficient, and allows for a reasonably large time-step. Another popular implicit integration method for MD simulations is the predictor-corrector scheme, in particular, Gear algorithm [84].

Similar to the numerical integration scheme, proper use of boundary conditions is crucial to obtaining a physically meaningful MD simulation. The boundary of a simulation cell is usually within close proximity to each simulated atom, because of limited computational power. Simulations for one billion atoms represent the upper limit of computation today with simple interatomic potentials (e.g., [64]). Total simulation times are typically less than one nanosecond as a result of short integration time steps in the femto-second range. The boundary of a simulation cell may not be a real physical interface, rather it is merely the interface of the simulation cell and its surroundings. Various boundary conditions are used in mechanics simulations. Since dislocations dominate the linking of nano- and micromechanics, the following presentation of boundary conditions focuses on those boundary conditions relevant to the long-range strain fields of dislocations. These boundary conditions include: the rigid boundary condition [85], periodic boundary condition [86], direct linking of atomistic and continuum regions [87], and flexible (Green's function) boundary condition [88–91].

The rigid boundary condition is probably the simplest. According to this condition, boundary atoms are fixed during molecular dynamics simulations. For simple dislocation configurations, the initial strain field, say of an infinitely long straight dislocation, is imposed on all atoms in the simulation cell. During subsequent simulations, boundary atoms are not allowed to relax. This rigidity of the boundary condition naturally leads to inaccuracy in the simulation results. The inaccuracy also exists in the application of the periodic boundary condition. According to this condition, the simulation cell is repeated periodically to fill the entire space. When one dislocation is included in the simulation cell, infinite number of its images are included in the entire space because of the infinite repetition of the simulation cell. Modifications have been made to include dipoles in a simulation cell, and to subtract the image effects. However, it is difficult to extend such modifications to general dislocation configurations, which are more complex.

In contrast to the two approximate boundary conditions, the direct linking and flexible boundary conditions can be rigorous. The direct linking of atomistic and continuum region [87] aims at a seamless bridging of two different scales. This idea has been extended to include the direct linking of atomistic and electronic structure regions [92]. Once numerically robust and efficient, the direct linking scheme should be the most reliable and desirable boundary condition. At present, the other rigorous scheme—flexible boundary condition—is more commonly used in dislocation simulations. This scheme has gone through the implementations in two and three dimensions. In the 1970s, the two-dimensional version of this boundary condition was implemented [88–90], allowing the simulation of a single straight dislocation. In these simulations, periodic boundary conditions are applied along the dislocation line. On the plane normal to the dislocation line, the simulation cell is divided into

three regions. The innermost region is MD region, in which atoms follow Newtonian dynamics according to the MD method outlined earlier. The intermediate region is the flexible region (or Green's function region), in which the force on each atom is calculated, and then used to generate displacements of all atoms in the simulation cell using the Green's function of displacement. Because periodic boundary condition is applied along the dislocation line, line forces are calculated in the flexible region, making the displacement two-dimensional. The outermost region contains atoms that serve as background for force calculations in the flexible region. As a result of renewed interest in dislocation dynamics, flexible boundary conditions have been extended to three dimensions, and are often referred to as the Green's function boundary conditions [91]. Flexible or Green's function boundary conditions have clear advantages in allowing for full relaxation of one or a few dislocations in a simulation cell, without suffering from the artifacts of image dislocations. However, Green's function calculations are time-consuming, limiting applications of the Green's function boundary condition. Recently, a tabulation and interpolation scheme [93] has been developed, improving the computational efficiency by two orders of magnitude, yet maintaining the accuracy of linear elasticity. With this improvement, the Green's function boundary conditions work well for static simulations of dislocations. However, they are not applicable to truly dynamic simulations. During dislocation motion, elastic waves are emitted, and when they interact with the simulation cell boundaries or borders, they are reflected and can lead to interference or even resonance in the simulation cell. Approximate approaches [94, 95] have been proposed to damp the waves at the boundary, but a fully satisfactory solution is still not available.

In addition to the numerical integration and boundary condition issues, successful MD simulations rely on the proper control of thermodynamic variables: stress and temperature. When the internal stress, as derived from interatomic interactions, is not balanced by the external stress, the simulation cell deforms accordingly. At small stress levels, this response is consistent with linear elasticity. Under general stress conditions, the formulation of [96] provides a mechanism to track the deformation. In this formulation, the three vectors describing the simulation cell shape are equated to position vectors of three imaginary atoms. The driving force of the imaginary atoms is the imbalance of internal and external stresses, and the displacement of those atoms are governed by Newton's equations of motion. This formulation works well when an equilibrated stress state is sought. However, large fluctuations in the deformation are unavoidable according to the Parrinello-Rahman method; the lattice constant may fluctuate by about 0.5% around its equilibrium value. This large fluctuation may introduce artifacts in the simulation of kinetic process, and caution should be exercised. The other thermodynamic variable, temperature, is controlled through the kinetic energy or velocities of all atoms. Using frictional forces to add or subtract heat, the Nose-Hoover method [97, 98] provides a mechanism of controlling the temperature of a simulation cell. When the temperature is uniform in space and constant in time, little difficulty exists. When the temperature changes, however, the strength of the frictional force dictates the transition time. A fast transition is usually necessary because of the short time reachable in MD simulations. However, such a transition is generally too fast compared to realistic processes. This transition problem exists in other temperature control mechanisms, such as velocity scaling or introduction of random forces.

The implementation and practice of MD simulations are more involved than the conceptual description alluded to here. A successful simulation depends on three major factors:

1. The computational implementation of the MD method;
2. The construction of accurate interatomic potentials; and
3. The analysis of massive data resulting from computer simulations.

In the following, we briefly present key concepts in the numerical implementation of MD methods, and then discuss salient aspects of the last two topics.

3.3.1. Choice of an Interatomic Potential

In general, interatomic potentials use in MD simulations are empirical or semiempirical, and thereby require fitting parameters. Simpler potentials, like the Lennard-Jones potential [64] and Morse potentials [65], have very few fitting parameters, which can be easily determined

from crystal properties. On the other hand, these potentials suffer from nontransferability. Because these potentials are fitted to only a few perfect crystal properties, their applicability in studying defects is by default questionable. The more sophisticated potentials, like the EAM—particularly the force matching approach [99]—use several or many defect properties to determine the EAM functions, in either analytical or tabular form. Material properties, of either the perfect crystal or defected structures, are obtained from *ab initio* calculations and reliable experiments. It is worth pointing out that these interatomic potentials apply for specific classes of materials. Strictly speaking, pair potentials are applicable to simulations of rare gas behavior. However, applications to simple metal systems can also provide qualitative guidance. The EAM type of potential has proven to be a good choice for simple metals. Applications to metals like aluminum, copper, silver, and iron (except its magnetic properties) have been very successful. The radial function form of the EAM is computationally advantageous. However, this advantage is accompanied by the inability to describe covalent systems, in which angular dependence dominates. In studying silicon, diamond carbon and other covalent systems, angular dependent potentials, particularly the Stillinger-Webber [69], the Tersoff [71], and the bond-order potentials [78] are among the leading candidates. A modification of the EAM has been proposed to include the angular dependence by [100], and applied to SiC by [101]; the modification by [102] is similar. Potentials that have quantum mechanical basis, such as the generalized pseudopotential [81, 103], the bond order potential [78], and the inversion method [104, 105] have also been used for greater accuracy.

3.3.2. Temperature and Pressure Control

In molecular dynamics simulations, we are usually interested in systems that can be described by global thermodynamic parameters, such as temperature, pressure energy, etc.. However, numerical integration of the system of equations does not guarantee that the overall system attains a specific thermodynamic state, and most often, we require temperature or pressure control. For a system to be simulated at a constant desired temperature, a typical simulation proceeds as follows: (1) we first assign velocities to all atoms in the system at a low temperature; (2) we then heat the system up to a desired temperature; (3) following the heat-up phase, we equilibrate the system for a short period of time; (4) and finally, we continue the simulation, but reset the simulation time to zero from that point on. During heating and equilibration, the temperature of the system is kept constant as described below. Dependent on how we apply simulation constraints, we would have different kinds of statistical ensembles. The NVE *ensemble* is the easiest one to be have, and it requires that the number of atoms, system volume and energy remain constant. The temperature of an NVE *ensemble* will fluctuate without modification. However, if the simulation must be carried on under certain temperature or pressure constraints, the NVE *ensemble* is not suitable anymore, and we have to adopt an NVT *ensemble*, NPT, or NPH *ensemble* instead [106]. Here, T is for constant temperature, N number of atoms, V system volume, E system energy, P system pressure, and H system enthalpy.

3.3.2.1. Constant-Temperature Algorithms   The essential idea behind all temperature or pressure control algorithms is that we simulate a system that undergoes additional interactions, or is coupled to an external thermodynamic bath. The energy can be transferred between the system and the external bath, which makes it possible to control the temperature of the system [107].

The Andersen procedure [108] is an early algorithm that suggests that, at certain time intervals during a simulation, the velocities of a randomly chosen particle could be reassigned on the basis of the Maxwell-Boltzmann distribution. Here, we imagine that the atom *collides* with one of the particles in a heat bath. However, due to velocity reassignment, energies are not smooth but discontinuous over time.

In the Nosé-Hoover method [97, 98, 109], we consider the system to be coupled to an external bath. The basis of this method is to introduce an extra, thermostating degree of freedom that represents the external thermal bath. In the original Nosé-Hoover method,

there is a single bath coordinate, η, and an associated momentum, p_η. The equations of motion of the combined system become:

$$\dot{\mathbf{R}} = \mathbf{M}^{-1}\mathbf{P} \tag{152}$$

$$\dot{\mathbf{P}} = \mathbf{F}(\mathbf{R}) - \frac{p_\eta}{Q}\mathbf{P} \tag{153}$$

$$\dot{\eta} = \frac{p_\eta}{Q} \tag{154}$$

$$\dot{p}_\eta = \mathbf{P}^{\mathbf{T}}\mathbf{M}^{-1}\mathbf{P} - N_{df}k_BT \tag{155}$$

where $\mathbf{R}$, $\mathbf{M}$, $\mathbf{P}$, and $\mathbf{F}$ are coordinates, mass, momentum and force arrays of the system. N_{df} is the number of coordinate degrees of freedom. Q is the *mass* of the thermostat, which is has units of mass times length squared, and determines the size of the coupling. Large values of Q lead to approximate constant-energy of the system, while small values of Q lead to large coupling and poor equilibration. p_η is the momentum of the bath. When its value is positive, the kinetic energy of the system decreases, while when this value is negative, the kinetic energy increases. The value of p_η is determined by equation (155) for the difference between the actual and desired temperature.

Another widely followed approach is to use Langevin equations as a stochastic analogues of Newton's equations of motion (i.e., Langevin dynamics). This equation can describe the interaction between an atom and a thermal bath quite well. It has two extra force terms: a random force and a frictional force that is proportional to the velocity of the particle. The random force buffets the particle about, while the frictional force dissipates any excess kinetic energy.

3.3.2.2. Constant-Pressure Algorithms   The idea behind pressure-control algorithms is similar to the temperature-control approach. The main difference is that pressure control modifies the coordinates and the volume of the system. One of the first algorithms for pressure control was also proposed by Andersen [108], where the volume of the simulation box, V, is introduced as an additional variable in the equations of motion:

$$\dot{\mathbf{R}} = \mathbf{M}^{-1}\mathbf{P} + \frac{1}{3}\frac{\dot{V}}{V}\mathbf{R} \tag{156}$$

$$\dot{\mathbf{P}} = \mathbf{F}(\mathbf{R}) - \frac{1}{3}\frac{\dot{V}}{V}\mathbf{P} \tag{157}$$

$$\ddot{V} = \frac{1}{W}(\mathscr{P} - P_B) \tag{158}$$

where $\mathscr{P}$ is the instantaneous pressure and P_B is the reference pressure. W is the effective *mass* of the volume degree of freedom, with units of mass times length to the fourth power.

3.4. The Kinetic Monte Carlo Method

The Monte Carlo (MC) technique is a statistical method for solving deterministic or probabilistic problems, by sampling from random distributions utilizing concepts of probability theory. A simple method for generation of random numbers according to a given distribution function is the inversion method [110]. In this approach, if the distribution function is normalized to obtain a probability density function (PDF), $p(x)$, we can determine the probability that the random variable x' is less than an arbitrary x by integrating the PDF from the minimum value to x. The integral of the (PDF) is called the cumulative distribution function (CDF), $C(x)$. When the CDF is equated to a uniformly distributed random number ξ, $C(x) = \xi$, the resulting solution for x gives the desired distribution function. If the PDF, $p(x)$, cannot be easily inverted analytically, sampling can be performed by the Von Neumann rejection technique. Another method to achieve the same result is known as importance sampling, and is a combination of the previous two methods. Here, we replace

the original distribution function, $p(x)$, by an approximate form, $\tilde{p}(x)$, for which the inversion method can be applied. Then we obtain trial values for x with the inversion technique following $p'(x)$. Finally, we accept trial values with the probability proportional to the weight w, given by $w = p(x)/\tilde{p}(x)$. The rejection technique has been shown to be a special case of importance sampling, where $p'(x)$ is a constant [5].

When the configurational space is discrete, and all rates at which they occur can be determined, we can choose and execute a single change to the system from the list of all possible changes at each MC step. This is the general idea of the Kinetic Monte Carlo (KMC) method [111–113]. The main advantage of this approach is that it can take into account simultaneous different microscopic mechanisms, and can cover very different time scales.

3.4.1. Elastic Representation of Defects

Although the interaction between atomic-size defects requires extensive MD or even *ab initio* calculations, the theory of elasticity can be used to simplify such calculations. Defect-defect interaction does not generally result in significant local deformation, and hence linear elasticity is expected to give accurate results. This approach has successfully been used to describe static defect-defect interactions [114–116].

Following Kröner [117] and Teodosiu [118], nanoscale defects exert forces on the atoms in theirs vicinity, which are different from those acting on these atoms in a perfect lattice. Let $\mathbf{P}^v$ denote the additional forces exerted by a nanodefect centred at $\mathbf{x}'$ on the atom situated at $\mathbf{x}' + \mathbf{l}^v$. According to the definition of Green's function, the force system $\mathbf{P}^v$ generates in an infinite elastic medium the displacement field

$$u_m(\mathbf{x}) = \sum_{v=1}^{N} G_{ms}(\mathbf{x} - \mathbf{x}' - \mathbf{l}^v)P_s^v \tag{159}$$

where $\mathbf{G}$ is Green's tensor function of the elastic medium, while N is the number of atoms on which extra forces are exerted. Theoretically, $N = \infty$, but, as $\mathbf{P}^v$ decays very rapidly when $\|\mathbf{l}^v\| \to \infty$, it is usually sufficient to take into account only the forces employed on the first and second nearest neighbors.

Expanding $\mathbf{G}(\mathbf{x} - \mathbf{x}' - l^v)$ in a Taylor series about $\mathbf{x} - \mathbf{x}'$ leads to

$$G_{ms}(\mathbf{x} - \mathbf{x}' - \mathbf{l}^v) = \sum_{k=0}^{\infty} \frac{1}{k!} G_{ms, q_1' q_2' \dots q_k'}(\mathbf{x} - \mathbf{x}') l_{q_1}^v l_{q_2}^v \dots l_{q_k}^v \tag{160}$$

where $(\cdot)_{m'} = \partial(\cdot)/\partial x_m'$. The expansion (160) converges only for sufficiently small values of $\|\mathbf{l}^v\|$, that is, only if the application points of the forces $\mathbf{P}^v$ are sufficiently close to the nano-defect.

Substituting (160) into (159), we have

$$u_m(\mathbf{x}) = \sum_{k=0}^{\infty} \frac{1}{k!} G_{ms, q_1' q_2' \dots q_k'}(\mathbf{x} - \mathbf{x}') P_{q_1 q_2 \dots q_k s}^{(k)} \tag{161}$$

where $\mathbf{P}^{(0)} = \sum_{v=1}^{N} \mathbf{P}^v$, $P_s^{(0)} = \sum_{v=1}^{N} P_s^v$, is the resultant force, and

$$\mathbf{P}^{(k)} = \sum_{v=1}^{N} \underbrace{\mathbf{l}^v \mathbf{l}^v \dots \mathbf{l}^v}_{k} \mathbf{P}^v, \quad P_{q_1 q_2 \dots q_k s}^{(k)} = \sum_{v=1}^{N} l_{q_1}^v l_{q_2}^v \dots l_{q_k}^v P_s^v \tag{162}$$

is the multipolar moment of the kth order, $k = 1, 2, \dots$, of the system of additional forces $\mathbf{P}^v$ exerted by the nanodefect on its surroundings. In particular, the following tensors are called dipole moment, quadrupole moment and octopole moment, respectively,

$$\mathbf{P}^{(1)} = \sum_{v=1}^{N} \mathbf{l}^v \mathbf{P}^v, \quad \mathbf{P}^{(2)} = \sum_{v=1}^{N} \mathbf{l}^v \mathbf{l}^v \mathbf{P}^v, \quad \mathbf{P}^{(3)} = \sum_{v=1}^{N} \mathbf{l}^v \mathbf{l}^v \mathbf{l}^v \mathbf{P}^v \tag{163}$$

Applying the differential operator

$$\frac{1}{k!} P^{(k)}_{q_1 q_2 \ldots q_k s} \frac{\partial^k}{\partial x'_{q_1} \partial x'_{q_2} \ldots \partial x'_{q_k}} \tag{164}$$

to the equilibrium equation of a unit point force

$$C_{ijmn} G_{ms,jn}(\mathbf{x} - \mathbf{x}') + \delta_{is} \delta(\mathbf{x} - \mathbf{x}') = 0 \tag{165}$$

where C_{ijmn} is the elastic tensor and δ_{is} is the Kronecker δ, and comparing the results with (161), we can see that the action of a nanodefect on the elastic medium is equivalent to that of a body force field, which consists of force dipoles, quadrupoles, octopoles, and so forth, applied at the center of the defect, namely:

$$f_i(\mathbf{x}) = \sum_{k=0}^{\infty} \widetilde{P}^{(k)}_{q_1 q_2 \ldots q_k i} \delta_{q'_1 q'_2 \ldots q'_k}(\mathbf{x} - \mathbf{x}') \tag{166}$$

where

$$\widetilde{P}^{(k)}_{q_1 q_2 \ldots q_k s} = \frac{1}{k!} P^{(k)}_{q_1 q_2 \ldots q_k s} \tag{167}$$

the strengths of the multipolar forces, $f_i(\mathbf{x})$, being completely determined through (167) by the multipolar moments associated with the nanodefect [118]. It should be noted that the resultant force and couple exerted by a nanodefect on its surroundings are zero. Thus, the equilibrium condition implies

$$\sum_{v=1}^{N} \mathbf{P}^v = 0, \quad \sum_{v=1}^{N} \mathbf{l}^v \times \mathbf{P}^v = 0 \tag{168}$$

The last relation may be rewritten as

$$\sum_{v=1}^{N} \epsilon_{kns} l^v_n P^v_s = \epsilon_{kns} P^{(1)}_{ns} = 0 \tag{169}$$

where ϵ_{kns} is so called permutation tensor. The dipole moment $\mathbf{P}^{(1)}$ must be a symmetric tensor, and conditions (168) are equivalent to:

$$\mathbf{P}^{(0)} = 0, \quad \mathbf{P}^{(1)} = (\mathbf{P}^{(1)})^{\mathrm{T}} \tag{170}$$

Introducing (170) into (161), we obtain:

$$u_m(\mathbf{x}) = \sum_{k=0}^{\infty} \frac{(-1)^k}{k!} G_{ms, q_1 q_2 \ldots q_k}(\mathbf{x} - \mathbf{x}') P^{(k)}_{q_1 q_2 \ldots q_k s} \tag{171}$$

Equation (171) shows that the elastic field produced by a nano-defect in an infinite elastic medium is completely determined by the multipolar moments $\mathbf{P}^{(k)}$, $k = 1, 2, \ldots$, provided that Green's tensor functions of the medium are known.

Because the elastic field of a nanodefect is characterized by its multipolar moments, the main idea of describing the elastic field of a defect reduces to the evaluation of these quantities by solving the equation system (171), with the displacement field $\mathbf{u}(\mathbf{x})$ acquired from molecular dynamics or statics simulations. As a first approximation, we now only consider the force system $\mathbf{P}^v$ exerted on the center of the defect and the first term in the Taylor expansion (171), that is, the dipole moment.

Suppose that the displacement of each and every lattice atom is already known from atomistic calculations. The least squares method can then be used to determine the equivalent point force dipolar system, that is, f_{jk}, which is to act at the center of the defect. If the real

displacement field (e.g., obtained from atomistics) is denoted by $\tilde{u}(\mathbf{x})$, we define the residual function

$$\Pi = \sum_{m=1}^{N} \|\mathbf{u}(\mathbf{x}) - \tilde{\mathbf{u}}(\mathbf{x})\|^2 = \sum_{m=1}^{N} [\mathbf{u}(\mathbf{x}) - \tilde{\mathbf{u}}(\mathbf{x})][\mathbf{u}(\mathbf{x}) - \tilde{\mathbf{u}}(\mathbf{x})] \tag{172}$$

where N is the number of points whose displacements are already known. The best fitting value of f_{jk} minimizes the residual Π:

$$\frac{\partial \Pi}{\partial f_{jk}} = 0 \tag{173}$$

The interaction energy, Φ_{int}, between two nanodefects can be shown to take the form [118]:

$$\Phi_{\text{int}} = -\mathbf{f} \cdot \boldsymbol{\nabla}\tilde{\mathbf{u}}(\mathbf{x}) = -f_{ij}\tilde{u}_{j,i}(\mathbf{x}) \tag{174}$$

where f_{ij} is the force dipole used to represent the nanodefect at $\mathbf{x}$, and $\tilde{\mathbf{u}}(\mathbf{x})$ is the displacement field induced by the defect at $\mathbf{x}'$, which can also be described by a force dipole tensor $\tilde{\mathbf{f}}$. Substituting the force dipole term of (171) for the displacement field produced by one of the defects into (174), we obtain:

$$\Phi_{\text{int}} = -f_{ij}\tilde{f}_{lk}G_{jk,li}(\mathbf{x} - \mathbf{x}') \tag{175}$$

It should be noted that this first-order description of nanodefects provides a good approximation only if the separation distance between defects is large enough and the geometry of the defect is rather simple.

3.4.2. Computational Model

The jump frequency (or the probability per unit time) for a possible jump of a SIA cluster, i, to take place is given by:

$$r_i = \omega_0 \exp\left(-\frac{E_i}{k_B T}\right) \tag{176}$$

where ω_0 is a pre-exponential factor of the defect cluster, k_B is the Boltzmann constant, E_i the "effective" activation energy for jumps of the cluster, and T is the absolute temperature. In the present work, we used MD results for the values of E_i for small defect clusters [119]. The first step in KMC simulations is to tabulate the rate at which an event (i) will take place anywhere in the system, r_i. The probability of selecting an event is equal to the rate at which the event occurs relative to the sum of all possible event rates. Once an event is selected, the system is changed correspondingly, and the list of events that can occur at the next KMC step is updated. Therefore, at each KMC step, one event denoted by m is randomly selected from all possible M events. Define $\tilde{r}_i = r_i / \sum_{i=0}^{M} r_i$ as the normalized event rate, where r_i is the actual rate of occurrence of an event i. If ξ is a random number uniformly distributed in the range [0, 1], then selection of an event m follows from the following condition: $\sum_{i=0}^{m-1} \tilde{r}_i < \xi < \sum_{i=0}^{m} \tilde{r}_i$. After an event is selected and executed, the total number of possible events, M, and the sequence in which the events are ordered, will change.

The reciprocal of an atomic jump probability per unit time is a residence time for a defect cluster that moves by that specific type of jump. Because the jump probabilities of all different types of jumps are independent, the overall probability per unit time for the system to change its state by any type of jump step is just the sum of all possible specific jump probabilities. Therefore, the residence time that would have elapsed for the system in a specific configuration is the reciprocal of the overall jump probability rate

$$\Delta t = \frac{1}{\sum_{i=0}^{M} r_i} \tag{177}$$

which is independent of the chosen transition. If ξ_2 is a random number from 0 to 1, the elapsed time for a particular transition is given by [120]:

$$\Delta t = \frac{-\ln \xi_2}{\sum_{i=0}^{M} r_i} \tag{178}$$

The system is then advanced to the final state of the chosen transition and the process is repeated. So far, all KMC computer simulations for microstructure evolution under irradiation have not considered the influence of the internal and applied stress fields on defect motion (e.g., Refs. [121] and [122]). Although explicit elastic interactions are not included in existing KMC treatments (e.g., in the ALSOME [122] or BIGMAC [121] codes), in most realistic situations interactions between dislocations and point defects play a key role in determining the effects of radiation on mechanical properties. The current KMC method accounts for elastic interactions amongst SIA clusters, nanovoids and dislocations. The numerical method developed by Ghoniem [123] and Ghoniem and Sun [124] is employed to evaluate the interaction between small defect clusters and slip dislocation loops. The interaction energy of two dislocation loops over the volume V is expressed as:

$$E_I = \int_V \sigma_{ij}^{(1)} \varepsilon_{ij}^{(2)} \, dV \tag{179}$$

in which $\sigma_{ij}^{(1)}$ is the stress arising from the first dislocation and $\varepsilon_{ij}^{(2)}$ the strain originating in the other. For the current study, if the second loop (defect cluster) is assumed to be infinitesimal, the interaction energy can be simplified to [114]

$$E_I = \delta A^{(2)} n_i^{(2)} \sigma_{ij}^{(1)} b_j^{(2)} \tag{180}$$

where $n_i^{(2)}$ is the unit normal vector to the defect cluster habit plane of area $\delta A^{(2)}$. Substituting the expressions of σ_{ij} given in [125] into (180) we can readily compute the interaction energy of the cluster, designated with the superscript (2), and the slip loop, of Burgers vector $b_n^{(1)}$. For simplicity, we assume that the stress tensor of grown-in (slip) dislocation loops is constant over the cross-section of a small point-defect cluster. In case we treat one single vacancy or interstitial atom as a center of dilatation, the interaction energy simplifies to

$$E_I = -\frac{4}{9} \pi r_0^3 \varepsilon_{ii}^{(2)} \sigma_{jj}^{(1)} \tag{181}$$

where $\varepsilon_{ii}^{(2)}$ is the dilatation and r_0 is the effective radius of a point defect. The elastic representation of defects introduced in the previous section was applied and Kroupa's solution [114] for the elastic field around an infinitesimal dislocation loop is utilized to determine the interaction between SIA clusters and vacancies.

We explicitly incorporate here the effects of elastic interactions between SIA and vacancy clusters themselves (cluster-cluster type), and between defect clusters and dislocations (dislocation-cluster type). SIA clusters are directly produced on the periphery of neutron collision cascades, and they may contain from a few atoms up to tens of atoms in the near vicinity of the cascade [126]. Such clusters are extremely mobile, and migrate predominantly along highly-packed crystallographic directions, with migration energies of less than 0.1 eV [121, 126]. Small SIA clusters may also spontaneously change their Burgers vector, and thus have the flexibility to translate along various crystallographic directions if their motion is not obstructed by internal strain fields. Because MD simulations have shown that the majority of SIA clusters have the form of mobile (glissile) perfect dislocation loops, we represent here SIA clusters as small prismatic, rigid and circular dislocation loops. We approximate vacancy clusters produced in cascades as small spherical voids, with an effective radius of $r_v = \sqrt[3]{3N\Omega/4\pi}$, where Ω is the atomic volume and N the number of vacancies in the cluster. The temperature dependence of the jump frequency of SIA clusters diffusion has been given by (176). The influence of other defects and the external stress on one SIA or vacancy cluster is given by the stress field σ_{ij}. For an infinitesimal dislocation loop, the interaction energy, E_{int}, is given by Eq. (180). Similarly, for a vacancy cluster, the interaction energy

is obtained from (181). The dilation, ε_{jj}, in this case, is given by $\varepsilon_{jj} = q/K = G\delta V/\pi a_0^3 K$, where $3K = 3\lambda + 2G$ is the bulk modulus.

The total cluster activation energy for migration is then given by:

$$\widetilde{E}_m = E_m + \Delta E_{int} \tag{182}$$

where E_m is the activation energy in a perfect crystal, and ΔE_{int} the difference in the interaction energy of a defect cluster placed at two neighboring equivalent positions in the crystal.

4. COMPUTATIONAL MESOMECHANICS

4.1. Introduction

Studies of the mechanical behavior of materials at a length scale larger than what can be handled by direct atomistic simulations, and smaller than what allows macroscopic continuum averaging represent particular difficulties. When the mechanical behavior is dominated by microstructure heterogeneity, the mechanics problem can be greatly simplified if all atomic degrees of freedom were adiabatically eliminated, and only those associated with defects are retained. Because the motion of all atoms in the material is not relevant, and only atoms around defects determine the mechanical properties, one can just follow material regions around defects. Because the density of defects is many orders of magnitude smaller than the atomic density, two useful results emerge. First, defect interactions can be accurately described by long-range elastic forces transmitted through the atomic lattice. Second, the number of degrees of freedom required to describe their topological evolution is many orders of magnitude smaller than those associated with atoms. These observations have been instrumental in the emergence of meso-mechanics on the basis of defect interactions by Eshelby, Kröner, Kossevich, Mura and others (see references [127–132]). Thanks to many computational advances during the past two decades, the field has steadily moved from conceptual theory to practical applications. While early research in defect mechanics focused on the nature of the elastic field arising from defects in materials, recent computational modelling has shifted the emphasis on defect ensemble evolution.

Two of the most fascinating features of microscale plasticity are the spontaneous formation of dislocation patterns, and the highly intermittent and spatially localized nature of plastic flow. Dislocation patterns consist of alternating dislocation rich and dislocation poor regions usually in the μm range (e.g., dislocation cells, sub-grains, bundles, veins, walls, and channels). On the other hand, the local values of strain rates associated with intermittent dislocation avalanches are estimated to be on the order of 1–10 million times greater than externally imposed strain rates [133, 134]. Understanding the collective behavior of defects is important because it provides a fundamental understanding of failure phenomena (e.g., fatigue and fracture). It will also shed light on the physics of elf-organization and the behavior of critical-state systems (e.g., avalanches, percolation, etc.).

In an attempt to resolve these observations, two main approaches have been advanced to model the mechanical behavior in this *meso* length scale. The first is based on statistical mechanics methods [135–142]. In these developments, evolution equations for statistical averages (and possibly for higher moments) are to be solved for a complete description of the deformation problem. The main challenge in this regard is that, unlike the situation encountered in the development of the kinetic theory of gases, the topology of interacting dislocations within the system must be included [141]. The second approach, commonly known as dislocation dynamics (DD), was initially motivated by the need to understand the origins of heterogeneous plasticity and pattern formation. An early variant of this approach (the cellular automata) was first developed by [143], and that was followed by the proposal of DD [144–147]. In these early efforts, dislocation ensembles were modelled as infinitely long and straight in an isotropic infinite elastic medium. The method was further expanded by a number of researchers [148–152], with applications demonstrating simplified features of deformation microstructure. We will describe the main features of these two approaches in the following.

4.2. Statistical Mesomechanics

Because of the high density of dislocations and the strong nature of their interactions, direct computer simulations of inhomogeneous plastic deformation and dislocation patterns is still unattainable. Even if direct computer simulations are successful in the description of these collective phenomena, it is very desirable to obtain global kinetic or thermodynamic principles for understanding the self-organization associated with plasticity at the microscale. To attain these objectives, and to enable a direct link with continuum deformation theory, the statistical mechanics approach has been advanced [135–142, 153–157]. The fundamental difficulty here is that dislocations, unlike particles, are linear objects of considerable topological complexity. Hence, when concepts of statistical mechanics and the theory of rate processes are used, some level of phenomenological description is unavoidable.

Statistical models of dislocation cells, persistent slip bands (PSBs), shear bands, or other organized dislocation structures attempt to develop continuum equations for dislocation densities that contain spatial gradients that drive instabilities and self-organization. Several models have been recently advanced, and will be reviewed here.

The Walgraef-Aifantis [135] statistical model has gained interest, because of its ability to predict dislocation pattern formation under cyclic deformation. The model is formulated as a set of reaction-diffusion equations with spatial derivatives that lead to inhomogeneous dislocation distributions, and will thus be first considered here. In this model, the static dislocation density, formed by the immobilized dislocations of the forest, sub-grain walls or boundaries, is defined as ρ_s, and the mobile dislocation density for dislocations gliding between obstacles is defined as ρ_m. For simplicity, consider systems oriented for single slip. Hence, the mobile dislocation density, ρ_m is divided into two subfamily densities representing dislocations gliding in the direction of the Burgers vector (ρ_m^+) or in the opposite direction (ρ_m^-) (with $\rho_m = \rho_m^+ + \rho_m^-$). These dislocation densities are related to the strain rate via the Orowan relation: $\dot{\epsilon} = b\rho_m v_g$, where b is the length of Burgers vector, ρ_m the total mobile dislocation density and v_g the glide velocity in the primary slip plane. Moreover, the dislocation densities are related to the internal stress by the relation:

$$\sigma_i = \frac{\mu b}{2\pi\lambda} + \xi\mu b\sqrt{\rho_s} \tag{183}$$

with μ is the shear modulus and ξ is a constant. In the last equation the first contribution comes from obstacles such as precipitates or pre-existing walls separated by an effective spacing λ and, the second part is the contribution from the static dislocation population which also opposes dislocation motion. The internal stress, σ_i, reduces the effective stress, σ_e, defined as: $\sigma_e = \sigma_a - \sigma_i$, with σ_a representing the applied stress. Finally, the glide velocity is related to the effective stress via appropriate phenomenological relations expressing the fact that individual dislocation motion is initiated when the effective stress acting on a dislocation exceeds the yield stress, in the form: $v_g \propto (\sigma_e/\sigma_0)^m$. This can be put more explicitly as:

$$v_g = v_0 \exp\left\{-\frac{\mu}{kT}\left(\frac{\sigma_e}{\sigma_0}\right)^{-m}\right\} \tag{184}$$

where σ_0 is the yield stress and $m > 1$. The essential features of dislocation dynamics are: their mobility, which includes thermal diffusion and climb, and their mutual interaction processes. By taking into account these mechanisms, the resulting dynamical system can be written as [135]:

$$\partial_t \rho_s = -\boldsymbol{\nabla} \cdot \mathbf{J}_s + v_g \rho_m \sqrt{\rho_s} - v_s d\rho_s^2 - v_g \delta\rho_m\rho_s - \beta\rho_s + v_g G(\rho_s)\rho_m$$

$$\partial_t \rho_m^+ = -\boldsymbol{\nabla} \cdot \mathbf{J}_+ + \frac{\beta}{2}\rho_s - v_g G(\rho_s)\rho_m^+ - v_g \delta\rho_m^+(\rho_s + \rho_m^-) \tag{185}$$

$$\partial_t \rho_m^- = -\boldsymbol{\nabla} \cdot \mathbf{J}_- + \frac{\beta}{2}\rho_s - v_g G(\rho_s)\rho_m^- - v_g \delta\rho_m^-(\rho_s + \rho_m^+)$$

where δ is the characteristic separation length between dislocations for spontaneous annihilation [158], d is the characteristic length of spontaneous dipole collapse, β is the frequency of dislocation freeing from the forest and is proportional to $v_g/\bar{d}$, where $\bar{d}$ is the characteristic dipole de-stabilization length which is inversely proportional to the effective stress, and $\beta = \beta_0 v_g \sigma_e$. The different characteristic lengths introduced here, or at least their order of magnitude, may in principle be evaluated from microscopic analysis [153, 158]. Due to mutual interactions, thermal activation and climb, forest dislocations mobility is represented by a diffusive current $\mathbf{J} = -D_s \nabla \rho_s$, which represents the effective diffusion within the forest. The current of mobile dislocations is taken as $\mathbf{J}_{\pm} = \pm \mathbf{v}_g \rho_m^{\pm}$ and represents the flux caused by gliding dislocations, in the present case, it is the flux caused by their edge component. Stability and numerical analyses of the previous set of equations have provided information on the conditions for formation of PSBs in fatigued specimens. It is shown that PSB formation is triggered by the clustering of dislocations or dislocation dipoles, which become finally immobile and arrange themselves in regularly spaced walls of high dislocation density [135].

Another class of models is based on the evolution of dipolar loops, triggered by their interaction with gliding dislocations [137, 138, 159]. The proposed statistical models are of the reaction-transport type, and focus on the feedback between the evolution of glide dislocations and the dipole density, as conceptualized earlier by [160]. The result is the sweeping of dipole loops by screw dislocations, which initiates the formation of dislocation walls. In this approach, dipole generation and interactions play a secondary role, and are introduced in an *ad hoc* and qualitative way.

To illustrate the statistical approach of Kratochvil and coworkers, let us consider N loops of one type (i.e., either interstitial or vacancy), $i = 1, \ldots, N$. For the ith loop, the equation of motion can be then expressed as:

$$\frac{d\mathbf{r}_i}{dt} = B\left(\sum_{j \neq i}^{N} \mathbf{f}_{\text{int}}(\mathbf{r}_i - \mathbf{r}_j) + \mathbf{f}_{\text{ext}}\right) \tag{186}$$

where B is the loop mobility and $\mathbf{f}_{\text{ext}}$ is the force caused by stress gradients and glide dislocations, and $\mathbf{f}_{\text{int}}$ is the interaction force between dipoles. In order to obtain a continuous field description, Eq. (186) is multiplied by the delta function $\delta(\mathbf{r} - \mathbf{r}_i)$, and the result is differentiated with respect to $\mathbf{r}$, thus we have:

$$\frac{d}{d\mathbf{r}}\left(\frac{d\mathbf{r}_i}{dt}\delta(\mathbf{r} - \mathbf{r}_i)\right) = B\frac{d}{d\mathbf{r}}\left(\left[\sum_{i=1}^{N} \mathbf{f}_{\text{int}}(\mathbf{r}_i - \mathbf{r}_j) + \mathbf{f}_{\text{ext}}\right]\delta(\mathbf{r} - \mathbf{r}_i)\right) \tag{187}$$

By introduction of the discrete density function $\varrho(\mathbf{r}, \mathbf{r}_1, \ldots, \mathbf{r}_N) = \sum_{j \neq i}^{N} \delta(\mathbf{r} - \mathbf{r}_i)$, and taking the sum on the right-hand side of Eq. (187), it can be replaced by a weighted integral. Summing up the above equation for all loops, one gets

$$\frac{d}{dt}\varrho(\mathbf{r}) + \frac{d}{d\mathbf{r}}[B\mathbf{f}(\mathbf{r})\varrho(\mathbf{r})] = 0 \tag{188}$$

where

$$\mathbf{f}(\mathbf{r}) \equiv \int \mathbf{f}_{\text{int}}(\mathbf{s} - \mathbf{r})\varrho(\mathbf{s})d\mathbf{s} + \mathbf{f}_{\text{ext}} \tag{189}$$

As a first approximation, it can be assumed that ϱ in Eq. (188) and definition (189) represents the local averaged loop density $\varrho(\mathbf{r})$ independent of detailed loop positions $\mathbf{r}_i$. Then, Eq. (188) represents the balance equation for the continuous distribution of loops described by the density $\varrho(\mathbf{r})$. Because the interaction force between loops f_{int} is short range, Kratochvil and coworkers use a Taylor series expansion of $\varrho(\mathbf{r})$ around $\mathbf{r}$ to finally obtain:

$$\mathbf{f}(\mathbf{r}) = -\frac{d\varrho(\mathbf{r})}{d\mathbf{r}}\int(\mathbf{s} - \mathbf{r})f_{\text{int}}(\mathbf{s} - \mathbf{r})d\mathbf{s} + \mathbf{f}_{\text{ext}} \tag{190}$$

From the balance Eq. (188) and approximation (190), the problem of loop-loop interaction was shown to be represented as a diffusion equation in a drift field:

$$\frac{d}{dt}\varrho(\mathbf{r}) = \frac{d}{d\mathbf{r}}\left[\mathscr{D}\frac{d\varrho(\mathbf{r})}{d\mathbf{r}}\right] + \frac{d}{d\mathbf{r}}\mathbf{f}_{\text{ext}} \tag{191}$$

where $\mathscr{D}$ is an effective diffusion coefficient, given by:

$$\mathscr{D} = B\varrho(\mathbf{r})\int \mathbf{s}\mathbf{f}_{\text{int}}(\mathbf{s})\,d\mathbf{s} \tag{192}$$

When the motion of screw dislocations is coupled with Eq. (191), self-organized patterns of dipolar loops may be attainable as conjectured by Mughrabi [160].

In an attempt to generalize the statistical description of dislocations, [141] described the dislocation content of a slip system by introducing the distribution $\phi^{(i)}(\mathbf{x}, \mathbf{v}, \mathbf{t}, t)$. Considering only glide motion, the tangent vector is described by a single scalar parameter: $\mathbf{t} = \mathbf{t}(\theta)$. The distribution function, $\phi^{(i)}$ is defined in a generalized phase space, such that $\phi^{(i)}(\mathbf{x}, \mathbf{v}, \theta, t)\,d\mathbf{x}\,d\mathbf{v}\,d\theta$ is the dislocation line length contained in the phase space volume $d\mathbf{x}\,d\mathbf{v}\,d\theta$ at time t on the ith slip system. The approach of [141] is to consider the conservation equation of the dislocation density tensor, $\boldsymbol{\alpha}$, for which dislocations on the ith slip system contribute:

$$\boldsymbol{\alpha}^{(i)}(\mathbf{x}, t) = \int_{\mathbf{v}}\int_{\theta}\mathbf{t}\otimes\mathbf{b}^{(i)}\phi^{(i)}(\mathbf{x}, \mathbf{v}, \theta, t)\,d\mathbf{v}\,d\theta \tag{193}$$

The condition of compatibility of the total distortion field in the crystal is written as: $\boldsymbol{\alpha} + \nabla\times\boldsymbol{\beta}^P = \mathbf{0}$ [161]. Considering a volume Ω, this can be extended to:

$$\mathscr{A} = \int_{\Omega}\boldsymbol{\alpha}\,d\Omega + \int_{\Omega}\nabla\times\boldsymbol{\beta}^P\,d\Omega = \mathbf{0} \tag{194}$$

$\boldsymbol{\beta}^P$ is the plastic distortion tensor. Eq. (194) corresponds to the principle of invariance of the total Burgers vector. For interacting dislocations, however, [141] included additional source terms to the conservation equations. Thus, for the ith slip system, we have:

$$\frac{d}{dt}\int_{\Omega}\boldsymbol{\alpha}^{(i)}d\Omega = \int_{\Omega}\sum\mathbf{S}^{(i)}d\Omega;\qquad i = 1, N \tag{195}$$

$\sum\mathbf{S}^{(i)}$ includes all possible tensorial sources, $\mathbf{S}^{(i)}$, resulting from Burgers vector reactions and cross slip. The time rate of variation of the dislocation density tensor in terms of the distribution function has been worked out by [141] as:

$$\frac{d}{dt}\int_{\mathbf{x}}\boldsymbol{\alpha}^{(i)}(\mathbf{x}, t)\,d\mathbf{x} = \int_{\mathbf{x}}\int_{\mathbf{v}}\int_{\theta}\mathbf{t}\otimes\mathbf{b}^{(i)}\left(\frac{\partial}{\partial t} + \mathbf{v}\cdot\nabla + \dot{\mathbf{v}}\cdot\nabla_v\right)\phi^{(i)}\,d\mathbf{x}\,d\mathbf{v}\,d\theta \tag{196}$$

where the terms containing $\dot{\theta}\partial/\partial\theta$ cancel each other. The right-hand side of (195) can also be represented by a phase space integral of scalar source functions

$$\int_{\Omega}\sum\mathbf{S}^{(i)}d\Omega = \int_{\mathbf{x}}\int_{\mathbf{v}}\int_{\theta}\mathbf{t}\otimes\mathbf{b}^{(i)}\sum S^{(i)}\,d\mathbf{x}\,d\mathbf{v}\,d\theta \tag{197}$$

From the last two equations, [141] finally obtained a set of kinetic equations, of the form:

$$\left(\frac{\partial}{\partial t} + \mathbf{v}\cdot\nabla + \dot{\mathbf{v}}\cdot\nabla_v\right)\phi^{(i)} = \sum S^{(i)};\qquad i = 1, N \tag{198}$$

It is also shown that this generalized approach can be reduced to the more simplified formulation of [162] in the special case of a system of parallel edge dislocations in a single slip configuration. The linear stability analysis of Groma [162] shows that a homogeneous stationary solution is unstable and that density perturbations grow, leading to pattern formation.

Hartley [163] introduced the concept of a dislocation distribution vector in an effort to connect DD simulations to continuum theories. This is defined as:

$$\boldsymbol{\rho}_\beta(\mathbf{t}) \equiv \mathbf{t}\rho_\beta(\mathbf{t}) \tag{199}$$

so that the magnitude of $\boldsymbol{\rho}_\beta(\mathbf{t})$ is

$$|\boldsymbol{\rho}_\beta(\mathbf{t})| = \rho_\beta(\mathbf{t}) \tag{200}$$

which is the total length per unit volume of dislocation lines with tangents parallel to $\mathbf{t}$, and with Burgers vector $\mathbf{b}_\beta$. The dislocation distribution vector is related to the Nye tensor, $\boldsymbol{\alpha}$, by:

$$\alpha = \sum_\beta \mathbf{b}_\beta \otimes \boldsymbol{\rho}_\beta \tag{201}$$

where the sum is carried over all Burgers vectors in all slip systems. The curvature tensor of the deformed volume is given by:

$$\boldsymbol{\kappa} = \frac{1}{2}Tr(\boldsymbol{\alpha})\mathbf{I} - \boldsymbol{\alpha} \tag{202}$$

Thus, it may be possible to compute the volumetric distortions associated with the movement of dislocations within a simulation volume, and then connect these distortions to continuum theories.

Zaiser [134] noted that because of the highly intermittent nature of plastic flow, the instantaneous active slip volume in FCC metals is of the order of 10^{-6} only, and that at typical strain rates of 10^{-4} s^{-1}, the time between neighboring avalanches exceeds the lifetime of an individual avalanche by 4–6 orders of magnitude. On that basis, he concluded that plastic deformation can be characterized as a slowly driven nonequilibrium system exhibiting large fluctuations. To estimate the magnitude of such fluctuations Hahner, [155] proposed that, if one neglects dislocation multiplication and annihilation, the average work done by the internal stress must be zero, and that the work of the external stress is dissipated into heat. Thus, one can write:

$$\langle \tau_{\text{int}}^\beta v^\beta \rangle = 0 \tag{203}$$

where τ_{int}^β and v^β are internal stresses and dislocation velocities on slip system β. Recognizing that the effective stress τ_{eff} has an external τ_{ext} plus an internal τ_{int} component, and upon separating the stress and velocity into average (represented by $\langle \cdots \rangle$) and fluctuating (represented by $\delta \cdots$) components, Zaiser [134] arrives at the following expressions for the autocorrelation functions of the effective stress τ_{eff}^β, and dislocation velocity v^β fluctuations:

$$\begin{aligned}
\langle (\delta\tau_{\text{eff}}^\beta)^2 \rangle &= \langle \tau_{\text{int}}^\beta \rangle \langle \tau_{\text{eff}}^\beta \rangle \\
\frac{\langle (\delta v^\beta)^2 \rangle}{\langle v^\beta \rangle^2} &= \frac{\langle \tau_{\text{int}}^\beta \rangle}{\langle \tau_{\text{eff}}^\beta \rangle} = \frac{b^2 \rho^\beta \langle \tau_{\text{int}}^\beta \rangle}{B \langle \dot{\gamma}^\beta \rangle}
\end{aligned} \tag{204}$$

where B is the mobility, and $\dot{\gamma}^\beta$ is the average shear strain rate. Using typical values for Cu in the previous equations, the relative velocity fluctuation is found to be on the order of 10^7 [134], in accordance with the experimental measurements of Neuhauser [133]. Recently, detailed measurements of the misorientation angles across dislocation walls have been made by Hughes [164]. Zaiser [134] formulated a velocity-averaged stochastic version of Equation (198) for the distribution function of *surplus dislocation segments*, or geometrically necessary dislocations to show that the probability distribution function for misorientation angles is in good agreement with the experimental measurements of Hughes [164].

A percolation-type stochastic dislocation model has been advanced by Thomson and coworkers [142, 165, 166]. In this model, which is limited to Stage III deformation, the weakest cell in a band undergoes a burst of strain, which initiates a cluster of newly strained cells. Slip transmission to neighboring cells is assumed to be of the form: $s^* = as$, where s is the

number of dislocations in the strained cell, a is a pileup amplification factor, and s^* is the number of dislocations in the previously unstrained cell. The key parameter in such model, a, is assumed to depend on two types of mechanisms: (1) a random distribution of sources within the cell walls, and/or (2) a distribution of locks holding up dislocations within the cell walls. Their analysis shows that percolating slip clusters conform to the universality class of percolation theory [167] can be effectively used to describe slip transmission in Stage III, and that a well-defined percolation threshold can be identified.

The power of statistical mechanics can be brought to bear on one of the most important challenges for the *multiscale modeling* approach. The large disparity in time and length scales during plastic deformation limit the reach of direct dislocation dynamics simulations. Hence, it is of interest to determine the necessary *coarse graining* strategies for both temporal and spatial variables. LeSar and coworkers have begun to tackle this issue by investigations of a number of specific problems, namely the combined motion of dislocations and solutes, and the problem of the long-range interactions of *blocks* of dislocation ensembles [157, 168–170].

In the limit where the solute mobility is high relative to that of the dislocations, dislocation-solute atmosphere pairs can be treated as *quasiparticles*, and the degrees of freedom associated with individual solute atoms can be eliminated [170]. Thus, and effective mobility can be derived, and can be related to the details of such interaction. However, in the other extreme limit of low solute mobility compared to dislocations, the solute atoms function essentially as static traps for dislocations. In this case, LeSar and coworkers modelled slip as a discrete, one-dimensional "birth-and-death" stochastic process [171]. [157] find that the dislocation diffusivity is modified by $\Delta D(c, \epsilon/k_B T)$:

$$\frac{\Delta D}{D'} = -c\frac{(\tau_t/\tau) - 1}{c(\tau_t/\tau) - 1 + 1} \tag{205}$$

where $\tau_t/\tau = e^{-\epsilon/k_B T}$ is the mean residence time in a trapped state, D' is the diffusivity when there are no traps, $c \equiv N_t/N$ is the trap (i.e., solute) concentration. These examples show that it may be possible to *average-out* fast time variables in dislocation dynamics simulations.

4.3. Discrete Dislocation Dynamics

4.3.1. Isotropic Crystals

Since it was first introduced in the mid 1980s independently by Lepinoux and Kubin [143] and by Ghoniem and Amodeo [144], dislocation dynamics (DD) has now become an important computer simulation tool for the description of plastic deformation at the micro- and mesoscales (i.e., the size range of a fraction of a micron to tens of microns). The method is based on a hierarchy of approximations that enable the solution of relevant problems with today's computational resources.

In its early versions, the collective behavior of dislocation ensembles was determined by direct numerical simulations of the interactions between infinitely long, straight dislocations [11, 143, 144, 146–152, 172–175]. Recently, several research groups extended the DD methodology to the more physical, yet considerably more complex 3D simulations. The method can be traced back to the concepts of internal stress fields and configurational forces. The more recent development of 3D lattice dislocation dynamics by Kubin and co-workers has resulted in greater confidence in the ability of DD to simulate more complex deformation microstructure [176–183]. More rigorous formulations of 3D DD have contributed to its rapid development and applications in many systems [184–193]. We can classify the computational methods of DD into the following categories:

1. The Parametric Method [191–194]: The dislocation loop can be geometrically represented as a continuous (to second derivative) composite space curve. This has two advantages: (1) there is no abrupt variation or singularities associated with the self-force at the joining nodes in between segments, (2) very drastic variations in dislocation curvature can easily be handled without excessive re-meshing. Other approximation methods have been developed by a number of groups. These approaches differ mainly

in the representation of dislocation loop geometry, the manner by which the elastic field and self energies are calculated, and some additional details related to how boundary and interface conditions are handled. The suitability of each method is determined by the required level of accuracy and resolution in a given application. dislocation loops are divided into contiguous segments represented by parametric space curves.

2. The Lattice Method [176, 195]: Straight dislocation segments (either pure screw or edge in the earliest versions, or of a mixed character in more recent versions) are allowed to jump on specific lattice sites and orientations. The method is computationally fast, but gives coarse resolution of dislocation interactions.

3. The Force Method [184, 188]: Straight dislocation segments of mixed character in the are moved in a rigid body fashion along the normal to their midpoints, but they are not tied to an underlying spatial lattice or grid. The advantage of this method is that the explicit information on the elastic field is not necessary, as closed-form solutions for the interaction forces are directly used.

4. The Differential Stress Method [185, 186]: This is based on calculations of the stress field of a differential straight line element on the dislocation. Using numerical integration, Peach-Koehler forces on all other segments are determined. The Brown procedure [196] is then used to remove the singularities associated with the self force calculation.

5. The Phase Field Microelasticity Method: This method is based on the reciprocal space theory of the strain in an arbitrary elastically homogeneous system of misfitting coherent inclusions embedded into the parent phase. Thus, consideration of individual segments of all dislocation lines is not required. Instead, the temporal and spatial evolution of several density function profiles (fields) are obtained by solving continuum equations in Fourier space [197–199].

We will develop in the following the basic ingredients of computational dislocation dynamics, following closely the parametric method. When the Green's functions are known, the elastic field of a dislocation loop can be constructed by a surface integration. The starting point in this calculation is the displacement field in a crystal containing a dislocation loop, which can be expressed as [130, 200]:

$$u_i(\mathbf{x}) = - \int_S C_{jlmn} b_m \frac{\partial}{\partial x'_l} G_{ij}(\mathbf{x}, \mathbf{x}') n_n \, \mathrm{d}S(\mathbf{x}') \tag{206}$$

where C_{jlmn} is the elastic constants tensor, $G_{ij}(\mathbf{x}, \mathbf{x}')$ are the Green's functions at $\mathbf{x}$ due to a point force applied at $\mathbf{x}'$, S is the surface capping the loop, n_n is a unit normal to S and b_m is the Burgers vector. The elastic distortion tensor, $u_{i,j}$ can be obtained from Eq. (206) by differentiation. The symmetric part of $u_{i,j}$ (elastic strain tensor) is then used in the stress-strain relationship to find the stress tensor at a field point $\mathbf{x}$, caused by the dislocation loop.

In an elastically isotropic and infinite medium, a more efficient form of Eq. (206) can be expressed as a line integral performed over the closed dislocation loop as [201]:

$$u_i = -\frac{b_i}{4\pi} \oint_C A_k dl_k + \frac{1}{8\pi} \oint_C \left[\epsilon_{ikl} b_l R_{pp} + \frac{1}{1-\nu} \epsilon_{kmn} b_n R_{mi} \right] dl_k \tag{207}$$

where μ and ν are the shear modulus and Poisson's ratio, respectively, $\mathbf{b}$ is Burgers vector of Cartesian components b_i, and the vector potential $A_k(\mathbf{R}) = \epsilon_{ijk} X_i s_j / [R(R + \mathbf{R} \cdot \mathbf{s})]$ satisfies the differential equation: $\epsilon_{pik} A_{k,p}(\mathbf{R}) = X_i R^{-3}$, where $\mathbf{s}$ is an arbitrary unit vector. The radius vector $\mathbf{R}$ connects a source point on the loop to a field point, as shown in Fig. 8, with Cartesian components R_i, successive partial derivatives $R_{ijk...}$, and magnitude R. The line integrals are carried along the closed contour C defining the dislocation loop, of differential arc length $d\mathbf{l}$ of components dl_k.

Consider now the virtual motion of the dislocation loop. The mechanical power during the virtual motion is composed of two parts: (1) change in the elastic energy stored in the medium upon loop motion under the influence of its own stress (i.e., the change in the loop self-energy), (2) the work done on moving the loop as a result of the action of external and internal stresses, excluding the stress contribution of the loop itself. These two components constitute the Peach-Koehler work [202]. The main idea of DD is to derive approximate
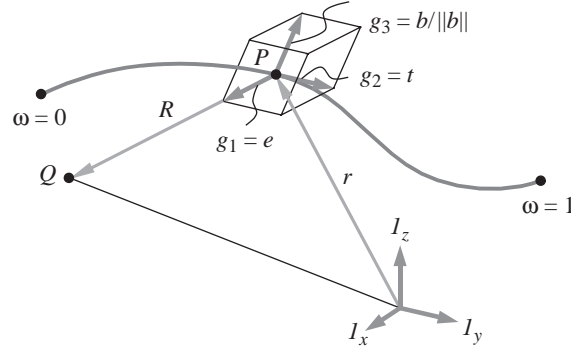
Figure 8. Parametric Representation of Dislocation Segments. After Ghoniem et al. (2001).

equations of motion from the principle of virtual power dissipation of the second law of thermodynamics [193], by finding virtual Peach-Kohler forces that would result in the simultaneous displacement of all dislocation loops in the crystal. A major simplification is that this many-body problem is reduced to the *single loop problem*. In this simplification, instead of moving all the loops simultaneously, they are moved sequentially, with the motion of each one against the collective field of all other loops. The approach is reminiscent of the single electron simplification of the many-electron problem in quantum mechanics.

In finite systems, the Green's functions are not invariant under $\mathbf{x} \to \mathbf{x}'$ transformations, and they become functions of both source and field points (i.e., not functions of the radius vector alone anymore). This does not allow the reduction of the surface integral of Eq. (207) to a simpler line integral by application of Stokes theorem. In addition, closed form solutions for the Green's functions and their spatial derivatives are available only for elastically isotropic materials. Therefore, rigorous 3D DD in finite, anisotropic systems (e.g., thin films, quantum dots, etc.) are very demanding, and have not yet been implemented.

If the material is assumed to be elastically isotropic and infinite, a great reduction in the level of required computations ensues. First, surface integrals can be replaced by line integrals along the dislocation. Second, Green's functions and their derivatives have analytical solutions. Thus, the starting point in most DD simulations so far is a description of the elastic field of dislocation loops of arbitrary shapes by line integrals of the form proposed by [201] as:

$$\sigma_{ij} = \frac{\mu}{4\pi} \oint_C \left[\frac{1}{2} R_{mpp} (\epsilon_{jmn} dl_i + \epsilon_{imn} dl_j) + \frac{1}{1-\nu} \epsilon_{kmn} (R_{ijm} - \delta_{ij} R_{ppm}) \, dl_k \right] \tag{208}$$

where μ and ν are the shear modulus and Poisson's ratio, respectively. The line integral is discretized, and the stress field of dislocation ensembles is obtained by a summation process over line segments.

Recently, Ghoniem and coworkers [190, 193] have shown that if dislocation loops are discretized into curved parametric segments, one can obtain the field by numerical integration over the scalar parameter that represents the segment. If one of these segments is described by a parameter ω that varies, for example, from 0 to 1 at end nodes of the segment. The segment is fully determined as an affine mapping on the scalar interval $\in [0, 1]$, if we introduce the tangent vector $\mathbf{T}$, the unit tangent vector $\mathbf{t}$, the unit radius vector $\mathbf{e}$, as follows: $\mathbf{T} = d\mathbf{l}/d\omega$, $\mathbf{t} = \mathbf{T}/|\mathbf{T}|$, $\mathbf{e} = \mathbf{R}/R$. Let the Cartesian orthonormal basis set be denoted by $\mathbf{1} \equiv \{\mathbf{1}_x, \mathbf{1}_y, \mathbf{1}_z\}$, $\mathbf{I} = \mathbf{1} \otimes \mathbf{1}$ as the second order unit tensor, and $\otimes$ denotes tensor product. Now define the three vectors $(\mathbf{g}_1 = \mathbf{e}, \mathbf{g}_2 = \mathbf{t}, \mathbf{g}_3 = \mathbf{b}/|\mathbf{b}|)$ as a covariant basis set for the curvilinear segment, and their contravariant reciprocals as: $\mathbf{g}^i \cdot \mathbf{g}_j = \delta^i_j$, where δ^i_j is the mixed Kronecker delta and $V = (\mathbf{g}_1 \times \mathbf{g}_2) \cdot \mathbf{g}_3$ the volume spanned by the vector basis, as shown in Fig. 8.

The differential stress field is given by:

$$\frac{d\boldsymbol{\sigma}}{d\omega} = \frac{\mu V |\mathbf{T}|}{4\pi(1-\nu)R^2} \{(\mathbf{g}^1 \otimes \mathbf{g}_1 + \mathbf{g}_1 \otimes \mathbf{g}^1) + (1-\nu)(\mathbf{g}^2 \otimes \mathbf{g}_2 + \mathbf{g}_2 \otimes \mathbf{g}^2) - (3\mathbf{g}_1 \otimes \mathbf{g}_1 + \mathbf{I})\} \tag{209}$$

Once the parametric curve for the dislocation segment is mapped onto the scalar interval $\{\omega \in [0, 1]\}$, the stress field everywhere is obtained as a fast numerical quadrature sum [190]. The Peach-Kohler force exerted on any other dislocation segment can be obtained from the total stress field (external and internal) at the segment as [202]:

$$\mathbf{F}_{PK} = \boldsymbol{\sigma} \cdot \mathbf{b} \times \mathbf{t} \tag{210}$$

The total self-energy of the dislocation loop is determined by double line integrals. However, [203] have shown that the first variation in the self-energy of the loop can be written as a single line integral, and that the majority of the contribution is governed by the local line curvature. Based on these methods for evaluations of the interaction and self-forces, the weak variational form of the governing equation of motion of a single dislocation loop was developed by Ghoniem [192] as:

$$\int_{\Gamma} (F_k^t - B_{\alpha k} V_\alpha) \delta r_k |d\mathbf{s}| = 0 \tag{211}$$

Here, F_k^t are the components of the resultant force, consisting of the Peach-Koehler force $\mathbf{F}_{PK}$ (generated by the sum of the external and internal stress fields), the self-force $\mathbf{F}_s$, and the osmotic force $\mathbf{F}_O$ (in case climb is also considered [192]). The resistivity matrix (inverse mobility) is $B_{\alpha k}$, V_α are the velocity vector components, and the line integral is carried along the arc length of the dislocation $d\mathbf{s}$. To simplify the problem, let us define the following dimensionless parameters:

$$\mathbf{r}^* = \frac{\mathbf{r}}{a}, \quad \mathbf{f}^* = \frac{\mathbf{F}}{\mu a}, \quad t^* = \frac{\mu t}{B}$$

Here, a is lattice constant, μ the shear modulus, and t is time. Hence, Eq. (211) can be rewritten in dimensionless matrix form as:

$$\int_{\Gamma^*} \delta \mathbf{r}^{*\top} \left(\mathbf{f}^* - \frac{d\mathbf{r}^*}{dt^*} \right) |d\mathbf{s}^*| = 0 \tag{212}$$

Here, $\mathbf{f}^* = [f_1^*, f_2^*, f_3^*]^\top$, and $\mathbf{r}^* = [r_1^*, r_2^*, r_3^*]^\top$, which are all dependent on the dimensionless time t^*. Following [192], a closed dislocation loop can be divided into N_s segments. In each segment j, we can choose a set of generalized coordinates q_m at the two ends, thus allowing parameterization of the form:

$$\mathbf{r}^* = \mathbf{C}\mathbf{Q} \tag{213}$$

Here, $\mathbf{C} = [C_1(\omega), C_2(\omega), \ldots, C_m(\omega)]$, $C_i(\omega)$, $(i = 1, 2, \ldots m)$ are shape functions dependent on the parameter $(0 \le \omega \le 1)$, and $\mathbf{Q} = [q_1, q_2, \ldots, q_m]^\top$, q_i are a set of generalized coordinates. Substituting Eq. (213) into Eq. (212), we obtain:

$$\sum_{j=1}^{N_s} \int_{\Gamma_j} \delta \mathbf{Q}^\top \left(\mathbf{C}^\top \mathbf{f}^* - \mathbf{C}^\top \mathbf{C} \frac{d\mathbf{Q}}{dt^*} \right) |d\mathbf{s}| = 0 \tag{214}$$

Let,

$$\mathbf{f}_j = \int_{\Gamma_j} \mathbf{C}^\top \mathbf{f}^* |d\mathbf{s}|, \quad \mathbf{k}_j = \int_{\Gamma_j} \mathbf{C}^\top \mathbf{C} |d\mathbf{s}|$$

Following a similar procedure to the FEM, we assemble the EOM for all contiguous segments in global matrices and vectors, as:

$$\mathbf{F} = \sum_{j=1}^{N_s} \mathbf{f}_j, \quad \mathbf{K} = \sum_{j=1}^{N_s} \mathbf{k}_j$$

then, from Eq. (214), we get,

$$\mathbf{K} \frac{d\mathbf{Q}}{dt^*} = \mathbf{F} \tag{215}$$

4.3.2. Anisotropic Crystals

For an anisotropic linearly elastic crystal, Mura [204] derived a line integral expression for the elastic distortion of a dislocation loop, as

$$u_{i,j}(\mathbf{x}) = \epsilon_{jnk}\, C_{pqmn} b_m \int_L G_{ip,q}(\mathbf{x} - \mathbf{x}') \nu_k \, dl(\mathbf{x}') \tag{216}$$

where ν_k is the unit tangent vector of the dislocation loop line L, dl is the dislocation line element, ϵ_{jnh} is the permutation tensor, C_{ijkl} is the fourth order elastic constants tensor, $G_{ij,l}(\mathbf{x} - \mathbf{x}') = \partial G_{ij}(\mathbf{x} - \mathbf{x}')/\partial x_l$, and $G_{ij}(\mathbf{x} - \mathbf{x}')$ are the Green's tensor functions, which correspond to displacement components along the x_i-direction at point $\mathbf{x}$ due to a unit point force in the x_j-direction applied at point $\mathbf{x}'$ in an infinite medium.

It can be seen that the elastic distortion formula (216) involves derivatives of the Green's functions, which need special consideration. For general anisotropic solids, analytical expressions for $G_{ij,k}$ are not available. However, these functions can be expressed in an integral form (see e.g. [205–208]), as:

$$\begin{aligned} G_{ij,k}(\mathbf{x} - \mathbf{x}') = \frac{1}{8\pi^2 |\mathbf{r}|^2} \oint_{C_k} \big[&-\bar{r}_k N_{ij}(\bar{\mathbf{k}}) D^{-1}(\bar{\mathbf{k}}) \\ &+ \bar{k}_k C_{lpmq}(\bar{r}_p \bar{k}_q + \bar{k}_p \bar{r}_q) N_{il}(\bar{\mathbf{k}}) N_{jm}(\bar{\mathbf{k}}) D^{-2}(\bar{\mathbf{k}}) \big]\, d\phi \end{aligned} \tag{217}$$

where $\mathbf{r} = \mathbf{x} - \mathbf{x}'$, $\bar{\mathbf{r}} = \mathbf{r}/|\mathbf{r}|$, $\bar{\mathbf{k}}$ is the unit vector on the plane normal to $\mathbf{r}$, the integral is taken around the unit circle C_k on the plane normal to $\mathbf{r}$, $N_{ij}(\mathbf{k})$ and $D(\mathbf{k})$ are the adjoint matrix and the determinant of the second order tensor $C_{ikjl}k_k k_l$, respectively.

At a point P on a dislocation line L, the external force per unit length is obtained by the Peach-Koehler formula: $\mathbf{F}^A = (\mathbf{b} \cdot \boldsymbol{\sigma}^A) \times \mathbf{t}$, where $\boldsymbol{\sigma}^A$ is the sum of the stress from an applied load and that arising from internal sources at P, $\mathbf{b}$ is the Burgers vector of the dislocation, and $\mathbf{t}$ is the unit tangent vector of the element $d\mathbf{l}$. For the special, yet important case of a planar dislocation loop lying on a glide plane with unit normal $\mathbf{n}$, the glide force acts along the in-plane normal to L at P: $\mathbf{m} = \mathbf{n} \times \mathbf{t}$. The glide component F_g^A of the external force can be obtained by resolving $\mathbf{F}^A$ along $\mathbf{m}$ as:

$$F_g^A = \mathbf{F}^A \cdot \mathbf{m} = \mathbf{b} \cdot \boldsymbol{\sigma}^A \cdot \mathbf{n} \tag{218}$$

The in-plane self-force at the point P on the loop is also obtained in a manner similar to the external Peach-Kohler force, with an additional contribution from *stretching* the dislocation line upon a virtual infinitesimal motion [209]:

$$F^S = \kappa E(\mathbf{t}) - \mathbf{b} \cdot \tilde{\boldsymbol{\sigma}}^S \cdot \mathbf{n} \tag{219}$$

where $E(\mathbf{t})$ is the pre-logarithmic energy factor for an infinite straight dislocation parallel to $\mathbf{t}$: $E(\mathbf{t}) = \frac{1}{2} \mathbf{b} \cdot \Sigma(\mathbf{t}) \cdot \mathbf{n}$, with $\Sigma(\mathbf{t})$ being the stress tensor of an infinite straight dislocation along the loop's tangent at $\mathbf{P}$. σ^S is self stress tensor due to the dislocation L, and $\tilde{\sigma} = \frac{1}{2}[\sigma^S(\mathbf{P} + \epsilon m) + \sigma^S(\mathbf{P} - \epsilon m)]$ is the *average* self-stress at P, κ is the in-plane curvature at $\mathbf{P}$, and $\epsilon = |\mathbf{b}|/2$.

Barnett and coworkers [203, 209] analyzed the structure of the self-force as a sum:

$$F^S = \kappa E(\mathbf{t}) - \kappa \left[E(\mathbf{t}) + E''(\mathbf{t}) \ln\left(\frac{8}{\epsilon \kappa}\right) \right] - J(L, \mathbf{P}) + F_{\text{core}} \tag{220}$$

where the second and third terms are line tension contributions, which usually account for the main part of the self-force, while $J(L, \mathbf{P})$ is a nonlocal contribution from other parts of the loop, and F_{core} is due to the contribution to the self-energy from the dislocation core.

4.3.3. Nanolayers and Thin Films

Most DD applications so far are for the deformation of bulk, isotropic materials. Very little attention has been paid to finding solutions for the elastic field of three-dimensional dislocations near interface, and no exact analytical solutions exist even for the simple case of straight dislocation segment in two half-space materials. Using approximate methods or numerical calculations, a few recent studies have attempted to treat the influence of free surfaces (i.e., *image effects*) on the dynamics of dislocation systems. These are summarized as:

1. In the superposition method, combined with the finite element or boundary element methods, numerical techniques are used to satisfy traction equilibrium at free surfaces [210, 211];
2. In the surface dislocation method, surface dislocation loop distributions are invoked so to approximately satisfy interfacial or free surface traction conditions at specific surface collocation points [212];
3. Approximate methods are based on Lothe's solution [213, 214], or assume rigid interfaces [215];
4. Elasticity methods for the solution of a dislocation segment near a free surface [216, 217] or the Boussinisque solution for a point force on a free surface [218].

The approaches described above have their limitations. Numerical methods [the finite element (FEM) or the boundary element (BEM)], suffer from the necessity to recalculate the superposed FEM or BEM solution every time step. As dislocations approach the surface or interface, the mesh must be refined, and the solution is not convergent if special care is not exercised with dislocation singularities. Other methods are limited to the simplest free surface boundary condition, and their extensions to anisotropic multilayered materials are not readily attainable, without ad hoc approximation. The numerous interfaces in multilayer thin films pose particular difficulties for all existing methods. No solution for 3D arbitrary shape dislocations in anisotropic multilayer materials is thus available.

We will first use the method of [219] to calculate Green's functions and their derivatives in anisotropic multilayers. The elastic field of dislocations in multilayer thin films is then presented, with numerical applications for infinitesimal and finite dislocation loops. Analysis of the effects of image forces due to free surfaces and interfaces will also be discussed.

4.3.3.1. Green's Tensor Functions and their Derivatives

Elastic Green's functions, which describe the displacement response of a linear elastic solid to a point force, are fundamental ingredients in many methods developed for understanding the mechanics of materials. A description of the internal, or *self* stress field of materials containing defects is critically dependent on accurate knowledge of elastic Green's functions. Interaction forces between defects and the elastic energy stored around them can be obtained once Green's functions are determined. Unfortunately, however, analytical solutions of Green's functions are not available, with the exception of a few cases. Moreover, numerical methods for 3D Green's functions in finite spaces of general elastic anisotropy are also very limited [221]. Using 2D Fourier transforms, numerical solutions for anisotropic Green's functions in half-space and bimaterials have been recently obtained [222]. Pan and coworkers developed Green's functions in anisotropic layered structures, such as bimaterials [223], trimaterials [220], and multilayers [219, 224]. In this section, we briefly present the basic procedure to calculate Green's functions in anisotropic multilayered materials using the 2D Fourier transform combined with the generalized Stroh's formalism. The presentation in this section follows references [219–223].

Subsequent developments for the elastic field and dislocation-interface interaction forces in the following sections will utilize the methods of these references, and hence a concise outline of the method for determination of Green's tensor functions will be given. Consider a stack of N layers, each of uniform thickness, perfectly-bonded at their interfaces, as shown in Fig. 9. Variables describing the geometry and coordinates are also shown in the figure. We assume here that each layer is homogeneous, anisotropic, and with distinct elastic properties.
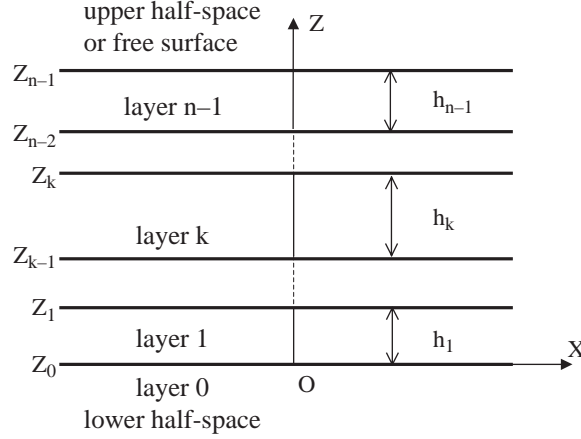
Figure 9. Geometry of a multilayered thin film system.

The Green's tensor function $G_{ij}(\mathbf{x}, \mathbf{x}')$ is the displacement component in the x_i-direction at point $\mathbf{x}$ in response to a unit body force in the x_j-direction, applied at point $\mathbf{x}'$. These functions satisfy the equilibrium equation:

$$C_{ijkl}(\mathbf{x})G_{km,lj}(\mathbf{x}, \mathbf{x}') = -\delta_{im}\delta(\mathbf{x}, \mathbf{x}') \tag{221}$$

Now, introduce the 2D Fourier transform, applied to the in-plane coordinates (x_1, x_2), for any function $f(x_1, x_2, x_3)$ in the real domain. The corresponding function in the Fourier domain, $\tilde{f}(\xi_1, \xi_2, x_3)$, is given by:

$$\tilde{f}(\xi_1, \xi_2, x_3) = \int_{-\infty}^{\infty} \int_{-\infty}^{\infty} f(x_1, x_2, x_3)e^{i(\xi_1 x_1 + \xi_2 x_2)} \, dx_1 \, dx_2 \tag{222}$$

Transforming Eq. (221), we obtain:

$$C_{i\alpha k\beta}\xi_\alpha\xi_\beta\widetilde{G}_{km} + \mathbf{i}(C_{i\alpha k3} + C_{i3k\alpha})\xi_\alpha\widetilde{G}_{km,3} - C_{i3k3}\widetilde{G}_{km,33} = e^{i\xi_\alpha x'_\alpha}\delta_{im}\delta(x_3, x'_3) \tag{223}$$

where $\alpha, \beta = 1, 2$.

The system of ordinary differential equations (223) is second order, with the independent variable being the out-of-plane coordinate x_3. The general solution for this system, which gives Green's functions in the Fourier domain is:

$$\begin{aligned}
\widetilde{\mathbf{G}}(\xi_1, \xi_2, x_3; \mathbf{x}') = e^{i\xi_\alpha x'_\alpha}\big[\widetilde{\mathbf{G}}^\infty(\xi_1, \xi_2, x_3; x'_3) \\
+ \mathbf{i}\eta^{-1}(\bar{\mathbf{A}}\langle e^{-i\bar{\mathbf{p}}\eta x_3}\rangle\mathbf{V} + \mathbf{A}\langle e^{-i\mathbf{p}\eta x_3}\rangle\mathbf{W})\big]
\end{aligned} \tag{224}$$

where (η, θ) are the polar coordinates of (ξ_1, ξ_2), $\mathbf{V}$ and $\mathbf{W}$ are unknown constant matrices to be determined from boundary conditions, $\langle e^{-i\mathbf{p}\eta x_3}\rangle = \text{diag}[e^{-ip_1\eta x_3}, e^{-ip_2\eta x_3}, e^{-ip_3\eta x_3}]$, p_i $(\text{Im}(p_i) > 0)$ and $\mathbf{A} = (\mathbf{a}_1, \mathbf{a}_2, \mathbf{a}_3)$ being the eigenvalues and eigenmatrix of

$$[\mathbf{Q} + p_i(\mathbf{R} + \mathbf{R}^T) + p_i^2\mathbf{T}]\mathbf{a}_i = 0$$
$$Q_{ik} = C_{ijks}n_jn_s, \quad R_{ik} = C_{ijk3}n_j, \quad T_{ik} = C_{i3k3} \tag{225}$$

with $n_1 = \cos\theta$, and $n_2 = \sin\theta$.

In the solution given by Eq. (224), Green's functions (displacements) are separated into two parts: a singular full-space solution $\widetilde{\mathbf{G}}^\infty$ (with elastic properties being those where the field point $\mathbf{x}$ is located, and the point force is applied at $\mathbf{x}' = (0, 0, x'_3)$), and a regular complementary part.

4.3.3.2. Stress Field of Dislocation Loops by Surface Integrals   Once Green's tensor functions are determined, the elastic field of a dislocation loop can be constructed by numerical integration. The displacement vector field of a dislocation loop can be expressed as [130]:

$$u_i(\mathbf{x}) = -\int_S C_{jlmn}(\mathbf{x}')b_m\frac{\partial}{\partial x_l'}G_{ji}(\mathbf{x}', \mathbf{x})n_n(\mathbf{x}')\,dS(\mathbf{x}') \tag{226}$$

where $G_{ji}(\mathbf{x}', \mathbf{x})$ are the Green's functions at $\mathbf{x}'$ due to a point force applied at $\mathbf{x}$, S is any arbitrary surface capping the loop, n_n is a unit normal to S and b_m is the Burgers vector. Equation (226) can be rewritten in another convenient form as:

$$u_i(\mathbf{x}) = -\int_S \sigma_{mni}(\mathbf{x}', \mathbf{x})b_m n_n(\mathbf{x}')\,dS(\mathbf{x}') \tag{227}$$

where $\sigma_{mni}(\mathbf{x}', \mathbf{x})$ is the mn-th Green's stress component at a field point $\mathbf{x}'$ due to a unit point force in the i-direction applied at the source point $\mathbf{x}$.

The stress field produced by the dislocation loop can be expressed as:

$$\sigma_{ij}(\mathbf{x}) = -C_{ijkl}(\mathbf{x})\int_S C_{pqmn}(\mathbf{x}')b_m\frac{\partial^2}{\partial x_l\partial x_q'}G_{pk}(\mathbf{x}', \mathbf{x})n_n(\mathbf{x}')\,dS(\mathbf{x}') \tag{228}$$

or

$$\sigma_{ij}(\mathbf{x}) = -C_{ijkl}(\mathbf{x})\int_S \frac{\partial}{\partial x_l}\sigma_{mnk}(\mathbf{x}', \mathbf{x})b_m n_n(\mathbf{x}')\,dS(\mathbf{x}') \tag{229}$$

When the dimensions of the dislocation loop are much smaller than the distance between any source point on the loop and the field point, the loop can be considered as infinitesimal, and its field can be obtained directly from Eqs. (226)–(229) without the surface integration.

$$\sigma_{ij}(\mathbf{x}) = -C_{ijkl}(\mathbf{x})\frac{\partial}{\partial x_l}\sigma_{mnk}(\mathbf{x}', \mathbf{x})b_m n_n(\mathbf{x}')\,\delta A \tag{230}$$

where δA is the loop area.

The derivatives of Green's functions with respect to both field and source points are needed. First, we consider derivatives with respect to a source point. The derivatives with respect to x_1' and x_2' in the Fourier domain are obtained as:

$$\partial\widetilde{\mathbf{G}}_k/\partial x_\alpha' = \mathbf{i}\xi_\alpha\widetilde{\mathbf{G}}_k, \quad \alpha = 1, 2 \tag{231}$$

where $\widetilde{\mathbf{G}}_k$ denotes Green's functions or Green's stresses of the k-th layer in the Fourier domain. The derivatives of Green's functions with respect to x_3' can be expressed as:

$$\frac{\partial\widetilde{\mathbf{G}}_k}{\partial x_3'} = e^{\mathbf{i}\xi_\alpha x_\alpha'}\left[\frac{\partial\widetilde{\mathbf{G}}_k^\infty}{\partial x_3'} + i\eta^{-1}\left(\overline{\mathbf{A}}_k\langle e^{-\mathbf{i}\bar{\mathbf{p}}_k\eta(x_3-z_{k-1})}\rangle\frac{\partial\mathbf{V}_k}{\partial x_3'} + \mathbf{A}_k\langle e^{-\mathbf{i}\mathbf{p}_k\eta(x_3-z_k)}\rangle\frac{\partial\mathbf{W}_k}{\partial x_3'}\right)\right] \tag{232}$$

Similarly, one can obtain the derivatives of Green's stresses. When we calculate Green's functions, $\mathbf{V}_k$ and $\mathbf{W}_k$ can be determined. However, their derivatives $\partial\mathbf{V}_k/\partial x_3'$ and $\partial\mathbf{W}_k/\partial x_3'$ are not available, and we need to calculate them separately for determination of the stress field. Performing derivatives on the boundary conditions, we obtain:

$$(\mathbf{Z}_k(z_k) - \mathbf{Z}_{k+1}(z_k))\begin{pmatrix}\dfrac{\partial\mathbf{V}_k}{\partial x_3'}\\[1mm]\dfrac{\partial\mathbf{W}_k}{\partial x_3'}\\[1mm]\dfrac{\partial\mathbf{V}_{k+1}}{\partial x_3'}\\[1mm]\dfrac{\partial\mathbf{W}_{k+1}}{\partial x_3'}\end{pmatrix} = \begin{pmatrix}\dfrac{\partial\tilde{\mathbf{u}}_{k+1}^\infty}{\partial x_3'}\\[1mm]\dfrac{\partial\tilde{\mathbf{t}}_{k+1}^\infty}{\partial x_3'}\end{pmatrix}(z_k) - \begin{pmatrix}\dfrac{\partial\tilde{\mathbf{u}}_k^\infty}{\partial x_3'}\\[1mm]\dfrac{\partial\tilde{\mathbf{t}}_k^\infty}{\partial x_3'}\end{pmatrix}(z_k), \quad k = 0, \ldots n-1 \tag{233}$$

$$\left(\overline{\mathbf{B}}_n \langle e^{-i\bar{p}_n \eta h_n} \rangle \mathbf{B_n}\right) \begin{pmatrix} \dfrac{\partial \mathbf{V}_n}{\partial x'_3} \\ \dfrac{\partial \mathbf{W}_n}{\partial x'_3} \end{pmatrix} = -\dfrac{\partial \tilde{\mathbf{t}}_n^\infty(z_n)}{\partial x'_3} \tag{234}$$

Solving the linear algebraic equations (233) [and (234) when needed], $\partial \mathbf{V}_k / \partial x'_3$ and $\partial \mathbf{W}_k / \partial x'_3$ $(k = 0, \ldots n)$ can be determined. Taking the inverse Fourier transforms of Eqs. (231) and (232), the derivatives with respect to $\mathbf{x}'$ are finally obtained.

4.3.3.3. Infinitesimal Dislocation Loop in Film-on-Substrate
Here, we show results for a small (infinitesimal) dislocation loop in a thin film on top of a very thick substrate, which is approximated as half-space. The film-substrate system is shown in Fig. 10, with a thin film (of thickness h) on top of a half-space substrate. The substrate material ($z < 0$) is copper, and the thin film is either aluminum or nickel. The materials selected for this example are all fcc cubic anisotropic crystals, with their crystallographic axes [100], [010], and [001] taken to coincide with the x, y, and z directions, respectively. The elastic constants are taken from reference [225]. The anisotropic ratio $A = 0.5(C_{11} - C_{12})/C_{44}$ is 3.21, 1.21, and 2.52 for Cu, Al, and Ni, respectively ($A = 1$ for isotropic materials).

We assume an infinitesimal dislocation is located at the middle of the thin film [i.e., $\mathbf{x}' = (0, 0, 0.5h)$], with its surface area δA lying on the (111) plane, and $\mathbf{b}$ along the [$\bar{1}$10]-direction. Figures 11 and 12 show contour lines for the out-of-plane stress σ_{32} and the in-plane stress σ_{12} on the plane $y = 0$, respectively. The stresses are normalized to $|\mathbf{b}|\delta A h^{-3} \times 10^{10}$. From these figures, it can be seen that the out-of-plane stresses are forced to decrease identically to zero at the surface to satisfy free traction boundary conditions. On the other hand, in-plane stresses are released at the free surface. At the interface ($z = 0$), the out-of-plane stress components are continuous, while in-plane components experience jumps as a result of the discontinuity in the elastic properties. As one approaches the interface from a softer material to a harder one (e.g., Al to Cu), the stress fields, especially in-plane components, are arrested. Once one moves across the interface, in-plane components are released, and experience a jump. It is also observed that he stress fields usually are more complex for a source in a material with a high anisotropic ratio (e.g., Ni), while show smoother variations in nearly isotropic materials (e.g., Al.)

4.3.3.4. Dislocation Loop in Film-on-Substrate
To understand the effects of free surfaces and the interfaces on stress distributions around finite-size dislocation loops, we present here results for a circular loop. As an example, we choose the same (Al) film and (Cu) substrate, as shown in Fig. 10. The circular shear loop (radius, $R = 0.5h$) is located in the middle of the film (0,0,0.5h), and lies on the (111)-plane, with $\mathbf{b}$ along the [$\bar{1}$10]-direction. Figure 13a shows the $\sigma_{23} = 0.15$ isosurface (normalized to $|\mathbf{b}|R^{-1} \times 10^{10}$). For comparison purposes, the same iso-surface in an Al infinite space is shown in Figure 13b. To satisfy the zero traction boundary condition at the top surface, the out–of-plane stress isosurface is totally confined below it. The volume of the same isosurface expands into the softer material
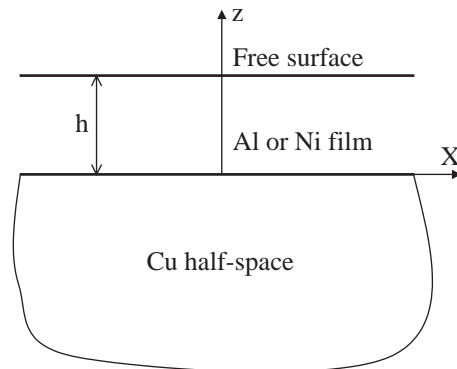
Figure 10. Geometry and coordinate system for the film-on-substrate arrangement.
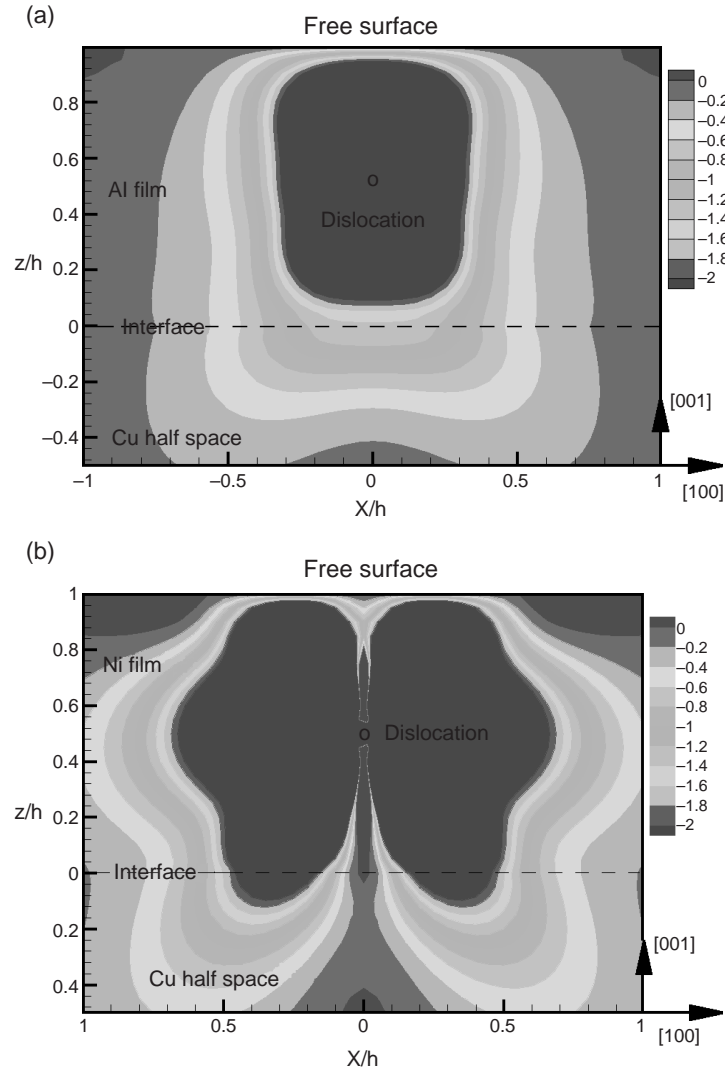
Figure 11. σ_{32} stress contours on the $y = 0$ plane due to an infinitesimal dislocation loop at $(0, 0, 0.5h)$ in (a) Al(film) on a Cu(substrate); (b) Ni(film) on a Cu(substrate).

across the interface. This means that the range of influence of a dislocation loop in a harder layer expands into neighboring softer layers, as compared to the infinite medium case.

4.3.3.5. Dislocation-Interface Interaction   So far, we determined the main characteristics of the elastic stress field induced finite size or infinitesimal dislocations in a multilayer material. However, an area of great interest, especially in relationship to DD simulations, is the distribution of configurational forces on dislocations as they move or change their shapes. A dislocations will experience a configurational force (i.e., the Peach-Koehler force), if it attempts motion or change in shape in a stress field, $\boldsymbol{\sigma}$. This force can be determined by the Peach-Koehler formula.

We will divide the stress field induced by a dislocation into two parts: the full-space solution $\boldsymbol{\sigma}^{\infty}$ and the image contribution $\boldsymbol{\sigma}^{I}$. This separation will allow us to consider interface effects on dislocation forces, and to calculate the dislocation self-force without ambiguities. For a dislocation loop that is located totally whin a single material layer, the stress separation is clear. $\boldsymbol{\sigma}^{\infty}$ corresponds to the stress field induced by the dislocation in a homogeneous, infinite medium with a material that is identical to the layer where the dislocation is located. The stress field $\boldsymbol{\sigma}^{\infty}$ of a dislocation in an infinite anisotropic material can be expressed as a line integral along the dislocation loop by the formula of Mura [130]. $\boldsymbol{\sigma}^{\infty}$ will then induce a *self-force* on the dislocation, which can be obtained by the procedure of [203], for details,
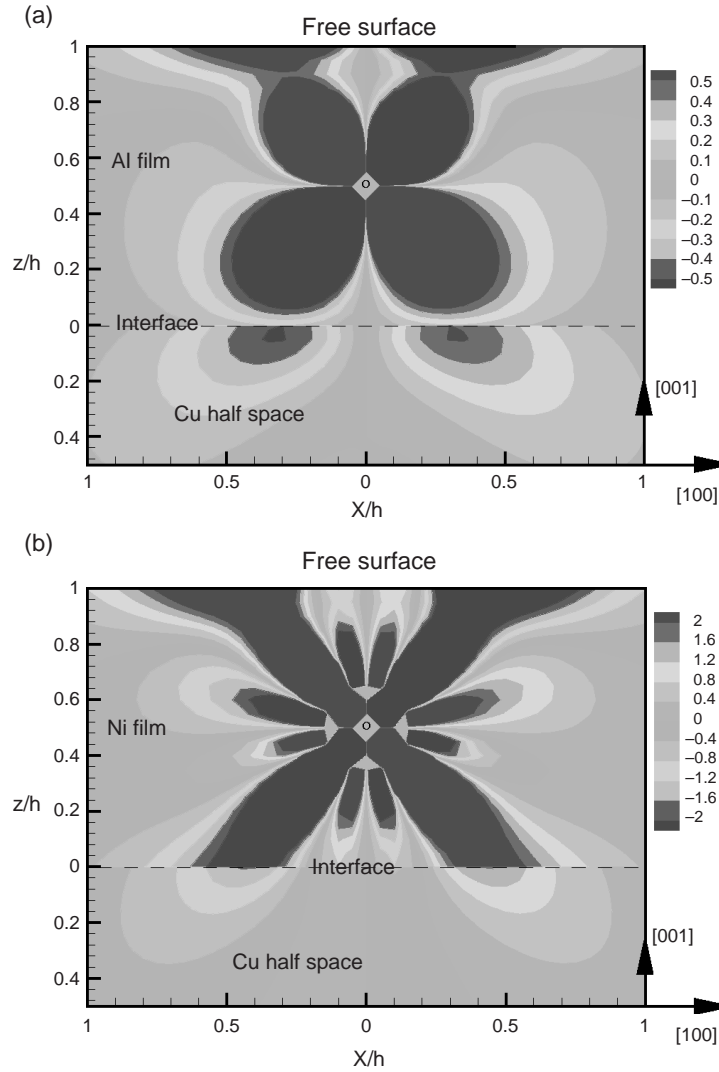
Figure 12. σ_{12} stress contours on the $y = 0$ plane due to an infinitesimal dislocation loop at $(0, 0, 0.5h)$ in (a) Al(film) on a Cu(substrate); (b) Ni(film) on a Cu(substrate).

see the work of [226]. The force induced by the regular part of the stress field, $\boldsymbol{\sigma}^I$, is usually called *image force*, and can be calculated directly by applying the Peach-Koehler formula.

When a dislocation loop does not reside totally in one single layer, but crosses one or more interfaces and material layers, the separation of self-force from the image force is not so straightforward. In this case, we distinguish between them in the following way. Consider a point **P** on the loop, and assume that the whole loop is in a homogeneous, infinite medium, with a material identical to that in which the point **P** is located. This loop will induce a stress field $\boldsymbol{\sigma}^\infty$ and self-force on the unit dislocation segment where **P** located. Now, subtract $\boldsymbol{\sigma}^\infty$ from the total stress field to obtain the image stress $\boldsymbol{\sigma}^I$, which is regular. We use this part of the stress field to calculate, unambiguously, the image force on the dislocation segment at **P**.

Force variations, for the two points A and B (which are the closest points when the corresponding loop segment approaches the interface), are displayed in Figs. 14a and 14b, respectively. Forces are plotted as functions of the distance of the point from the interface, and they include self and image contributions. They are also separated into glide and climb components. The 2D image force approximation (*Koehler barrier*), estimated for an infinite straight dislocation near the interface is calculated and shown in the figures as dashed lines [227]. It can be seen that when the loop is in one material (not across the interface), only the glide component of the image force at the leading point (nearest to the interface) is
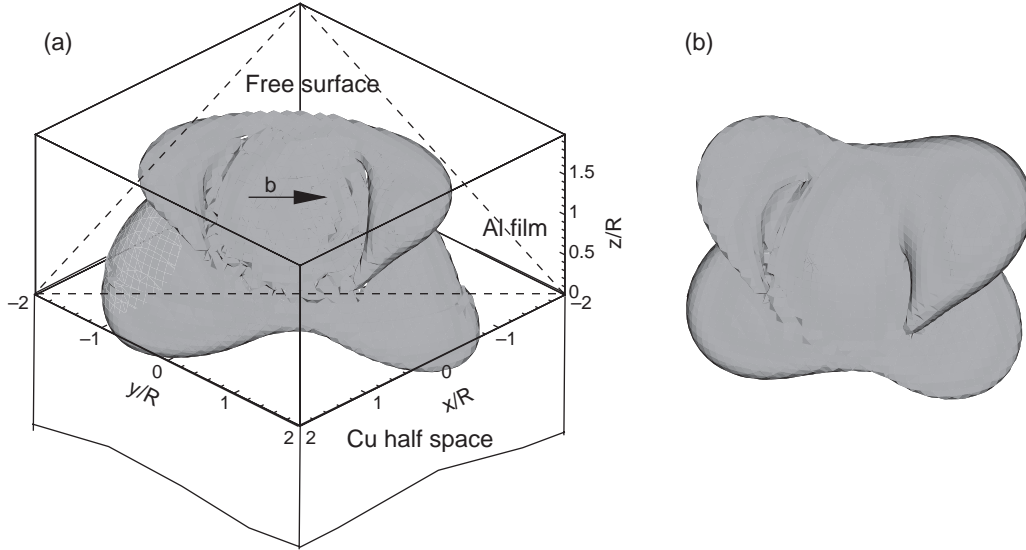
Figure 13. σ_{23} stress isosurface for a circular shear dislocation loop in (a) Al(film) on a Cu(substrate); (b) Al infinite space.

close to the Koehler estimate. The climb component and other loop configurations show drastic differences from the Koehler estimate as a result of the three dimensionality of the problem.

The direction of the in-plane curvature of the loop is chosen as the positive direction for the self- and glide-forces, while the positive direction of the climb force is defined along the plane normal to (111). It observed that when the distance between the leading point on the dislocation and the interface is less than 20|**b**|, image forces increase sharply and interface effects become dominant. If linear elasticity is taken as strictly valid, the force is singular at the interface. Here, however, we assume its validity up to a minimum approach distance on the order of the dislocation core width of 2|**b**|. The results displayed in Figs. 14a and 14b show the complexity of loop force variations in the close proximity of the interface. First, the jump in the self force is a result of the sudden change in the elastic constants of the medium, and the magnitude of the force scales with the stiffness of the material. What is interesting here to note is that while the climb component of the image force (including the Koehler barrier) is dominant on the closest segment when the loop crosses from the softer (Al) to the harder (Cu) material, as seen in Fig. 14a, the situation is reversed when the loop crosses from Cu into Al (see Figure 14b). This unique asymmetry is a result of the fact that the entire loop geometry determines the split between the climb ($\mathbf{f}_c$), and glide ($\mathbf{f}_g$) components of the force. Such detailed behavior can be critical to whether the dislocation segment would prefer to climb and cross-slip across an interface, or just simply continue gliding on the same glide plane if the orientation is favorable.

4.3.4. Line Integral Forms for DD

For a 3D dislocation loop of general geometry, the displacement vector can be expressed as [130]

$$u_i(\mathbf{x}) = -\int_S C_{jlmn} b_m \frac{\partial}{\partial x_l'} G_{ji}(\mathbf{x}', \mathbf{x}) n_n(\mathbf{x}') \, dS(\mathbf{x}') \tag{235}$$

where C_{jlmn} are the elastic moduli, $G_{ji}(\mathbf{x}', \mathbf{x})$ are the Green's functions at $\mathbf{x}'$ due to a point force applied at $\mathbf{x}$, S is an arbitrary surface capping the loop, n_n is a unit normal to S and b_m is the Burgers vector.

The surface integral in Eq. (235) is valid for a dislocation loop in either homogeneous or inhomogeneous materials, assuming that the elastic Greens functions for a particular geometry and elastic anisotropy are known. There are two main difficulties in using Eq. (235). First, evaluation of surface integrals for dislocation loops of complex 3D geometry can be
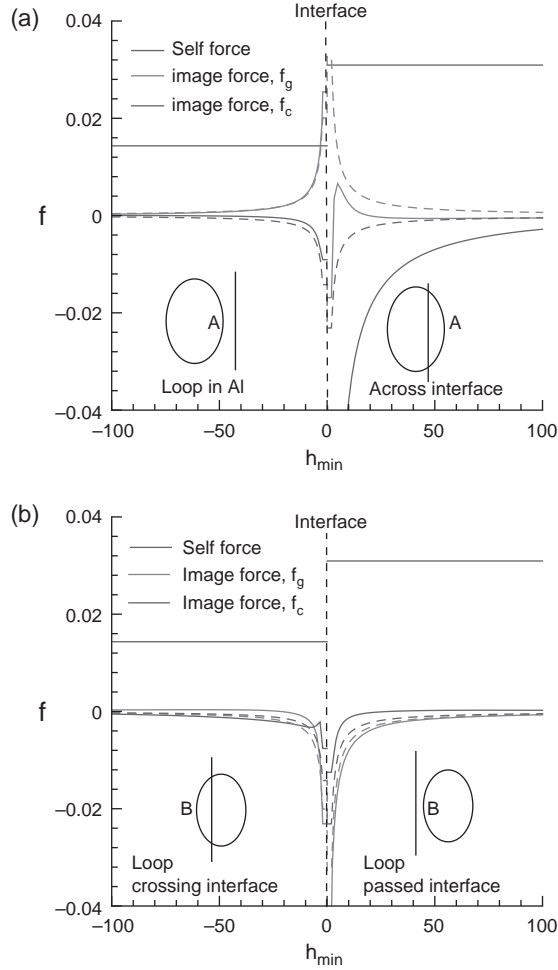
Figure 14. Dependence of force components on (a) the leading point A and (b) the trailing point B, as functions of their distance from the interface. Koehler's 2D solution is represented by dashed lines.

computationally demanding and intensive [228]. Second, elastic Greens functions are not explicitly known for inhomogeneous anisotropic materials.

For a dislocation loop in an infinite homogeneous space, the displacement gradient tensor can be reduced to a line integral along the dislocation as [130, 208]:

$$u_{i,j}(\mathbf{x})^{\infty} = \oint_L \beta_{jih}^{\infty}(\mathbf{x} - \mathbf{x}') \, dl_h(\mathbf{x}') \tag{236}$$

where

$$\beta_{jih}^{\infty}(\mathbf{x} - \mathbf{x}') = C_{klmn} b_m \epsilon_{jnh} G_{ik,l}^{\infty}(\mathbf{x} - \mathbf{x}') \tag{237}$$

and L and dl_h are the dislocation line and line element, respectively. The superscript ∞ represents quantities in an infinite space, $f_l = \partial f / \partial x_l$, and ϵ_{jnh} is the usual permutation tensor.

The stress field produced by the dislocation can then be expressed as:

$$\sigma_{ij}(\mathbf{x})^{\infty} = \oint_L S_{ijh}^{\infty}(\mathbf{x} - \mathbf{x}') \, dl_h(\mathbf{x}') \tag{238}$$

where

$$S_{ijh}^{\infty}(\mathbf{x} - \mathbf{x}') = C_{ijkl} C_{pqmn} \epsilon_{lnh} b_m G_{kp,q}^{\infty}(\mathbf{x} - \mathbf{x}') \tag{239}$$

The kernel $S_{ijh}^{\infty}(\mathbf{x} - \mathbf{x}')$ in Eq. (239) can be considered as the ij-stress component at $\mathbf{x}$ produced by a line element of dislocation lying in the h-direction at $\mathbf{x}'$, with Burgers vector $\mathbf{b}$

in an infinite space, while $\beta_{jih}^{\infty}(\mathbf{x} - \mathbf{x}')$ in Eq. (237) can be considered as the corresponding displacement gradient.

For a finite space, the field produced by the elemental dislocation source in an infinite space is not guaranteed to satisfy prescribed boundary conditions. We therefore need to add a complementary solution [denoted as $S_{ijh}^{C}(\mathbf{x}, \mathbf{x}')$ or $\beta_{jih}^{C}(\mathbf{x}, \mathbf{x}')$] to the infinite medium solution [$S_{ijh}^{\infty}(\mathbf{x} - \mathbf{x}')$ or $\beta_{jih}^{\infty}(\mathbf{x} - \mathbf{x}')$], such that all boundary conditions can be satisfied. For example, on a free surface at $x_3 = 0$, we should have: $[S_{ijh}^{\infty}(\mathbf{x} - \mathbf{x}') + S_{ijh}^{C}(\mathbf{x}, \mathbf{x}')]|_{x_3=0} = 0$. If a complementary solution (with a superscript C) can be obtained, then the elastic field due to a dislocation loop in the corresponding finite space can be evaluated through the line integral:

$$u_{i,j}(\mathbf{x}) = \oint_L \left[\beta_{jih}^{\infty}(\mathbf{x} - \mathbf{x}') + \beta_{jih}^{C}(\mathbf{x}, \mathbf{x}') \right] dl_h(\mathbf{x}') \tag{240}$$

$$\sigma_{ij}(\mathbf{x}) = \oint_L \left[S_{ijh}^{\infty}(\mathbf{x} - \mathbf{x}') + S_{ijh}^{C}(\mathbf{x}, \mathbf{x}') \right] dl_h(\mathbf{x}') \tag{241}$$

The first terms in Eqs. (240) and (241) are known infinite space solutions, and contain well-understood singularities. The second (complementary) terms, however, are regular, and need to be determined according to interface and boundary conditions. Now, assume that the displacement field of the complementary kernel is u_{kh}^{C}. The stress field it produces is then: $S_{ijh}^{C}(\mathbf{x}, \mathbf{x}') = C_{ijkl}u_{kh,l}^{C}(\mathbf{x}, \mathbf{x}')$, and the corresponding equilibrium equation is given by:

$$C_{ijkl}(\mathbf{x})u_{kh,lj}^{C}(\mathbf{x}, \mathbf{x}') = 0 \tag{242}$$

For a layered medium, the general solution can be obtained by a Fourier transform with respect to the in-plane coordinates (x_1, x_2) as

$$\tilde{\mathbf{u}}(\xi_1, \xi_2, x_3; x_3') = \int_0^{\infty} \int_0^{\infty} \mathbf{u}[\mathbf{x}; (0, 0, x_3')]e^{i\xi_{\alpha}x_{\alpha}} \, dx_1 \, dx_2 \tag{243}$$

The equilibrium equation then becomes:

$$C_{i3k3}\tilde{u}_{kh,33}^{C} - \mathbf{i}(C_{i\alpha k3} + C_{i3k\alpha})\xi_{\alpha}\tilde{u}_{kh,3}^{C} - C_{i\alpha k\beta}\xi_{\alpha}\xi_{\beta}\tilde{u}_{kh}^{C} = 0 \tag{244}$$

where the Greek subscript $\alpha = 1$ or 2, whereas Roman subscripts range over 1,2,3.

The general solution of Eq. (244) can be expressed in a compact form as [219]:

$$\tilde{\mathbf{u}}^{C}(\xi_1, \xi_2, x_3; x_3') = \mathbf{i}\eta^{-1}(\overline{\mathbf{A}}\langle e^{-i\overline{\mathbf{p}}\eta x_3}\rangle\mathbf{V} + \mathbf{A}\langle e^{-i\mathbf{p}\eta x_3}\rangle\mathbf{W}) \tag{245}$$

where (η, θ) are the polar coordinates of (ξ_1, ξ_2) $(\xi_1 = \eta\cos\theta, \xi_2 = \eta\sin\theta)$, $\mathbf{V}$ and $\mathbf{W}$ are unknown functions (of η, θ and x_3'), $\langle e^{-i\mathbf{p}\eta x_3}\rangle = \text{diag}[e^{-ip_1\eta x_3}, e^{-ip_2\eta x_3}, e^{-ip_3\eta x_3}]$, p_i $(\text{Im}\, p_i > 0)$ and $\mathbf{A} = (\mathbf{a}_1, \mathbf{a}_2, \mathbf{a}_3)$ are the eigenvalues and eigen-matrix of the generalized Stroh eigen-problem [222]:

$$[\mathbf{Q} + p_i\mathbf{R} + \mathbf{R}^T) + p_i^2\mathbf{T}]\mathbf{a}_i = 0$$
$$Q_{ik} = C_{ijks}n_jn_s, \quad R_{ik} = C_{ijks}n_jm_s, \quad T_{ik} = C_{ijks}m_jm_s \tag{246}$$

with $\mathbf{n} = [\cos\theta, \sin\theta, 0]^T$ and $\mathbf{m} = [0, 0, 1]^T$.

The displacement gradient for the complementary solution is:

$$\tilde{\mathbf{u}}_{\alpha}^{C}(\xi_1, \xi_2, x_3; x_3') = n_{\alpha}(\overline{\mathbf{A}}\langle e^{-i\overline{\mathbf{p}}\eta x_3}\rangle\mathbf{V} + \mathbf{A}\langle e^{-i\mathbf{p}\eta x_3}\rangle\mathbf{W}) \tag{247}$$

The induced stress field will then be: $S_{ijh}^{C}(\mathbf{x}, \mathbf{x}') = C_{ijkl}u_{kh,l}^{C}(\mathbf{x}, \mathbf{x}')$. We will separate the field into two contributions: (1) out-of-plane stresses $\mathbf{t} = (S_{13h}, S_{23h}, S_{33h})$, and (2) in-plane stresses $\mathbf{s} = (S_{11h}, S_{12h}, S_{22h})$. In the transformed domain, these can be expressed as [219]:

$$\tilde{\mathbf{t}}^{C}(\xi_1, \xi_2, x_3; x_3') = \overline{\mathbf{B}}\langle e^{-i\overline{\mathbf{p}}\eta x_3}\rangle\mathbf{V} + \mathbf{B}\langle e^{-i\mathbf{p}\eta x_3}\rangle\mathbf{W} \tag{248}$$

$$\tilde{\mathbf{s}}^{C}(\xi_1, \xi_2, x_3; x_3') = \overline{\mathbf{C}}\langle e^{-i\overline{\mathbf{p}}\eta x_3}\rangle\mathbf{V} + \mathbf{C}\langle e^{-i\mathbf{p}\eta x_3}\rangle\mathbf{W} \tag{249}$$

The matrices $\mathbf{B} = (\mathbf{b}_1, \mathbf{b}_2, \mathbf{b}_3)$ and $\mathbf{C} = (\mathbf{c}_1, \mathbf{c}_2, \mathbf{c}_3)$ are related to the Stroh eigen-matrix $\mathbf{A}$ as

$$\mathbf{b}_i = (\mathbf{R}^T + p_i\mathbf{T})\mathbf{a}_i, \quad \mathbf{c}_i = \mathbf{D}_i\mathbf{a}_i \tag{250}$$

with $D_{kli} = C_{1kl\alpha}n_\alpha + p_iC_{1kl3}$ for $k = 1, 2$, and $D_{3li} = C_{22l\alpha}n_\alpha + p_iC_{22l3}$. Note that for a half space $x_3 \leq 0$, $V = 0$, while for $x_3 \geq 0$, $W = 0$.

In order to impose the appropriate boundary conditions for layered materials, the transformed Green's tensor in an infinite space is needed. This is given by:

$$\widetilde{G}^\infty(\xi_1, \xi_2, x_3; x_3') = \mathbf{i}\eta^{-1}\begin{cases} \mathbf{A}\langle e^{-\mathbf{i}\mathbf{p}\eta(x_3-x_3')}\rangle\mathbf{A}^T, & x_3 < x_3' \\ -\overline{\mathbf{A}}\langle e^{-\mathbf{i}\overline{\mathbf{p}}\eta(x_3-x_3')}\rangle\overline{\mathbf{A}}^T, & x_3 > x_3' \end{cases} \tag{251}$$

We determine here the complementary terms necessary for obtaining full solutions for dislocation loops in half-space, bi-materials, and in general anisotropic layered media.

4.3.4.1. Dislocation in an Anisotropic Half-Space

Let's assume that a dislocation loop is situated in an anisotropic half-space, occupying $x_3 \leq 0$ and having a free surface on $x_3 = 0$. The surface equilibrium boundary condition is expressed as:

$$\left[S_{i3h}^C(\mathbf{x}, \mathbf{x}') + S_{i3h}^\infty(\mathbf{x} - \mathbf{x}')\right]\big|_{x_3=0} = 0 \tag{252}$$

In the transformed domain, we have:

$$\widetilde{S}_{i3h}^C(\mathbf{x}, \mathbf{x}')\big|_{x_3=0} = \tilde{t}_{ih}^C\big|_{x_3=0} = \mathbf{BW} \tag{253}$$

$$\widetilde{S}_{i3h}^\infty(\mathbf{x} - \mathbf{x}') = C_{i3kl}C_{pqmn}\epsilon_{lnh}b_m\widetilde{G}_{kp,q}^\infty(\mathbf{x} - \mathbf{x}')$$
$$= -\mathbf{i}\xi_\alpha C_{i3kl}C_{p\alpha mn}\epsilon_{lnh}b_m\widetilde{G}_{kp}^\infty + C_{i3kl}C_{p3mn}\epsilon_{lnh}b_m\widetilde{G}_{kp,3}^\infty \tag{254}$$

Substituting (251) (for $x_3' < x_3 \leq 0$) into (254), we obtain:

$$\widetilde{S}_{i3h}^\infty\big|_{x_3=0} = \lambda_{ikhpq}[n_q(-\overline{\mathbf{A}}\langle e^{\mathbf{i}\overline{\mathbf{p}}\eta x_3'}\rangle\overline{\mathbf{A}}^T)_{kp} + m_q(-\overline{\mathbf{A}}\langle e^{\mathbf{i}\overline{\mathbf{p}}\eta x_3'}\rangle\langle\overline{\mathbf{p}}\rangle\overline{\mathbf{A}}^T)_{kp}] \tag{255}$$

where $\lambda_{ikhpq} = C_{i3kl}C_{pqmn}\epsilon_{lnh}b_m$

Substituting (253) and (255) into the free traction surface boundary condition (in the transformed domain): $\widetilde{S}_{i3h}^C(\mathbf{x}, \mathbf{x}')\big|_{x_3=0} + \widetilde{S}_{i3h}^\infty\big|_{x_3=0} = 0$, we get:

$$\mathbf{W} = \mathbf{B}^{-1}\lambda_{ikhpq}\left[n_q(\overline{\mathbf{A}}\langle e^{\mathbf{i}\overline{\mathbf{p}}\eta x_3'}\rangle\overline{\mathbf{A}}^T)_{kp} + m_q(\overline{\mathbf{A}}\langle e^{\mathbf{i}\overline{\mathbf{p}}\eta x_3'}\rangle\langle\overline{\mathbf{p}}\rangle\overline{\mathbf{A}}^T)_{kp}\right] \tag{256}$$

The unknown coefficient $\mathbf{W}$ in the complementary solution is thus determined. Substituting (256) into Eqs. (245), (248), and (249) determines the complementary parts of the displacement vector and stress tensor. These are complex explicit expressions, but can be written in the following forms:

$$\tilde{\mathbf{u}}^C = \mathbf{i}\eta^{-1}\mathbf{J}_2\langle e^{-\mathbf{i}\mathbf{r}_1\eta}\rangle\mathbf{J}_1\langle e^{-\mathbf{i}\mathbf{r}_0\eta}\rangle\mathbf{J}_0 \tag{257}$$

for the displacement vector, and

$$\tilde{\mathbf{t}}^C = \mathbf{J}_2\langle e^{-\mathbf{i}\mathbf{r}_1\eta}\rangle\mathbf{J}_1\langle e^{-\mathbf{i}\mathbf{r}_0\eta}\rangle\mathbf{J}_0 \tag{258}$$

for the traction tensor. The same expression is also obtained for the in-plane tensor $\tilde{\mathbf{s}}$. In Eqs. (257) and (258), the tensors $\mathbf{J_n}(\theta)$ and $\mathbf{r_n}(\theta)$ are independent of η, but are functions of θ. These solutions are in the transformed domain, and need to be transformed back to the physical domain by the inverse Fourier transform:

$$f(x_1 - x_1', x_2 - x_2', x_3, x_3') = \frac{1}{(2\pi)^2}\int_0^\infty\int_0^{2\pi}\eta\tilde{f}(\eta, \theta, x_3, x_3')e^{-\mathbf{i}\eta[(x_1-x_1')\cos\theta+(x_2-x_2')\sin\theta]}\,d\theta\,d\eta \tag{259}$$

Carrying out the first integral over $(0 < \eta < \infty)$, the 2D inverse transformation is reduced to a 1D integral [219]. The reduced integrals for the elastic fields are given by:

$$u_{ih}^C = \frac{1}{(2\pi)^2} \oint_0^{2\pi} \frac{H_{ih}}{s} \, d\theta \tag{260}$$

$$t_{ih}^C = -\frac{1}{(2\pi)^2} \oint_0^{2\pi} \frac{H_{ih}}{s^2} \, d\theta \tag{261}$$

with $H_{ih} = (J_{k_2})_2 (J_{k_2 k_1})_1 (J_{k_1})_0$, and $s = (r_{k_2})_1 + (r_{k_1})_0 + (x_1 - x_1') \cos \theta + (x_2 - x_2') \sin \theta$. Note that s_{ih} has the same expression as that of t_{ih}, and that all these functions have their own H_{ih} (different from each other), but share the same s. Thus, the complementary parts of the elastic field of a dislocation in a half-space can be evaluated by line integrals over the interval $[0, 2\pi]$. The complementary parts plus the infinite-space solutions are the total elastic fields due to an infinitesimal dislocation segment, and the elastic field due to a dislocation loop is obtained through the line integrals (240) and (241).

4.3.4.2. Dislocation in Perfectly Bonded, Anisotropic Two Half Spaces

Consider an anisotropic bi-material full space, where the lower half-space $(x_3 < 0)$ is occupied by material (0), the upper half-space $(x_3 > 0)$ by material (1), and quantities in them are denoted by the corresponding superscripts (0) and (1), respectively. Suppose now that the interface (at $x_3 = 0$) is perfectly bonded. This requires the continuity of the displacement and traction vectors across the interface, that is,

$$\mathbf{u}^{(0)}\big|_{x_3=0^-} = \mathbf{u}^{(1)}\big|_{x_3=0^+} \qquad \mathbf{t}^{(0)}\big|_{x_3=0^-} = \mathbf{t}^{(1)}\big|_{x_3=0^+} \tag{262}$$

Instead of the displacement continuity condition (262), however, we will use an equivalent condition on the tangential displacement gradient, given by [229]:

$$\mathbf{u}_\alpha^{(0)}\big|_{x_3=0^-} = \mathbf{u}_\alpha^{(1)}\big|_{x_3=0^+} \tag{263}$$

Here, $\alpha = 1$ or 2, $\mathbf{u}_\alpha$ is the in-plane component of the displacement gradient (or called tangential distortion).

Without loss of generality, we assume that we have an infinitesimal dislocation segment, located in material (0). We express the solution for the displacement gradient in material (0) as:

$$\tilde{\mathbf{u}}_j^{(0)} = \tilde{\mathbf{u}}_j^{(0)\infty} + \tilde{\mathbf{u}}_j^{(0)C} = \tilde{\beta}_{jih}^{(0)\infty} + n_j \mathbf{A}^{(0)} \langle e^{-i\mathbf{p}^{(0)}\eta x_3} \rangle \mathbf{W} \tag{264}$$

The first term $\tilde{\mathbf{u}}_j^{(0)\infty}$ corresponds to the homogeneous full-space solution, which is known from Eq. (237), with the elastic properties of material (0). The second term corresponds to the complementary solution due to the interface. Correspondingly, the stress field is also separated into two components, and the traction vector can be expressed as:

$$\tilde{\mathbf{t}}^{(0)} = \tilde{\mathbf{t}}^{(0)\infty} + \tilde{\mathbf{t}}^{(0)C} = \tilde{S}_{i3h}^{(0)\infty} + \mathbf{B}^{(0)} \langle e^{-i\mathbf{p}^{(0)}\eta x_3} \rangle \mathbf{W} \tag{265}$$

where $S_{i3h}^{(0)\infty}$ is known from Eq. (227), with the elastic properties of material (0).

Likewise, the solutions in material (1) due to the infinitesimal dislocation segment in material (0) can also be separated. Thus, the displacement gradient in material (1) is expressed as:

$$\tilde{\mathbf{u}}_j^{(1)} = \tilde{\mathbf{u}}_j^{(0)\infty} + \tilde{\mathbf{u}}_j^{(1)C} = \tilde{\beta}_{jih}^{(0)\infty} + n_j \overline{\mathbf{A}}^{(1)} \langle e^{-i\overline{\mathbf{p}}^{(1)}\eta x_3} \rangle \mathbf{V} \tag{266}$$

The first term $\tilde{\mathbf{u}}_j^{(0)\infty}$ is the known full-space solution, with the elastic properties of material (0), while the second term is the complementary solution (which is to be determined). The stress field in material (1) can be derived from $\tilde{\mathbf{u}}_j^{(1)}$, giving the traction field as:

$$\tilde{\mathbf{t}}^{(1)} = \tilde{\mathbf{t}}^{(1)\infty} + \tilde{\mathbf{t}}^{(1)C} = \tilde{S}_{i3h}^{(1)\infty} + \overline{\mathbf{B}}^{(1)} \langle e^{-i\overline{\mathbf{p}}^{(0)}\eta x_3} \rangle \mathbf{V} \tag{267}$$

with

$$S_{i3h}^{(1)\infty} = C_{ijkl}^{(1)} C_{pqmn}^{(0)} \epsilon_{lnh} b_m G_{kp,q}^{(0)\infty}(\mathbf{x} - \mathbf{x}') \tag{268}$$

as the traction field in full-space material (1) due to the displacement field $\tilde{\mathbf{u}}^{(0)}$.

Substituting Eqs. (264)–(268) into the interface conditions, we have:

$$\mathbf{B}^{(0)}\mathbf{W} + \widetilde{S}_{i3h}^{(0)\infty}\big|_{x_3=0} = \overline{\mathbf{B}}^{(1)}V + \widetilde{S}_{i3h}^{(1)\infty}\big|_{x_3=0} \tag{269}$$

$$n_\alpha \mathbf{A}^{(0)}\mathbf{W} + \tilde{\beta}_{\alpha ih}^{(0)\infty}\big|_{x_3=0} = n_\alpha \overline{\mathbf{A}}^{(1)}V + \tilde{\beta}_{\alpha ih}^{(0)\infty}\big|_{x_3=0} \tag{270}$$

Finally, the full solution is obtained as:

$$\mathbf{W} = -(\overline{\mathbf{B}}^{(1)}\overline{\mathbf{A}}^{(1)-1}\mathbf{A}^{(0)} - \mathbf{B}^{(0)})^{-1}\Delta\widetilde{S}_{i3h}^\infty, \quad \mathbf{V} = (\mathbf{B}^{(0)}\mathbf{A}^{(0)-1}\overline{\mathbf{A}}^{(1)} - \overline{\mathbf{B}}^{(1)})^{-1}\Delta\widetilde{S}_{i3h}^\infty \tag{271}$$

with

$$\Delta\widetilde{S}_{i3h}^\infty = \widetilde{S}_{i3h}^{(1)\infty}\big|_{x_3=0} - \widetilde{S}_{i3h}^{(0)\infty}\big|_{x_3=0} = (C_{ijkl}^{(1)} - C_{ijkl}^{(0)})C_{pqmn}^{(0)}\epsilon_{lnh} b_m \widetilde{G}_{kp,q}^{(0)\infty}(\mathbf{x} - \mathbf{x}')\big|_{x_3=0}$$

$$\widetilde{G}_{kp,q}^{(0)\infty}\big|_{x_3=0} = -n_q(\overline{\mathbf{A}}^{(0)}\langle e^{\mathbf{i}\bar{\mathbf{p}}^{(0)}\eta x_3'}\rangle\overline{\mathbf{A}}^{(0)T})_{kp} - m_q(\overline{\mathbf{A}}^{(0)}\langle e^{\mathbf{i}\bar{\mathbf{p}}^{(0)}\eta x_3'}\rangle\langle\bar{\mathbf{p}}^{(0)}\rangle\overline{\mathbf{A}}^{(0)T})_{kp} \tag{272}$$

The displacement and stress (including displacement distortion) solutions have the same forms as Eqs. (257) and (258), respectively, and all real fields are obtained by 1D integrals, as in Eqs. (260) and (261).

4.3.4.3. Dislocation in an Anisotropic Multilayer Material

Consider a laterally infinite composite thin film made of different layers. Each layer is homogenous, anisotropic and of uniform thickness. Interfaces between layers are assumed to be perfectly bonded. A coordinate system (x_1, x_2, x_3) is attached to the the thin film, with the x_3-axis perpendicular to all interfaces. A general layer n occupies the space $z_{n-1} \leq x_3 \leq z_n$, and quantities with its properties are denoted by corresponding superscripts (n). Assume now that an infinitesimal dislocation segment is located in layer k. The displacement gradient in layer n can be expressed as:

$$\tilde{\mathbf{u}}_j^{(n)} = \tilde{\beta}_{jih}^{(k)\infty} + n_j[\overline{\mathbf{A}}^{(n)}\langle e^{-\mathbf{i}\bar{\mathbf{p}}^{(n)}\eta(x_3-z_{n-1})}\rangle\mathbf{V}^{(n)} + \mathbf{A}^{(n)}\langle e^{-\mathbf{i}\mathbf{p}^{(n)}\eta(x_3-z_n)}\rangle\mathbf{W}^{(n)}] \tag{273}$$

The first term is the full-space solution, given by Eq. (237), with the elastic properties of material k. The other terms correspond to the complementary part of the solution. Accordingly, the out-of-plane traction vector is given by:

$$\tilde{\mathbf{t}}^{(n)} = \widetilde{S}_{i3h}^{(n)\infty} + [\overline{\mathbf{B}}^{(n)}\langle e^{-\mathbf{i}\bar{\mathbf{p}}^{(n)}\eta(x_3-z_{n-1})}\rangle\mathbf{V}^{(n)} + \mathbf{B}^{(n)}\langle e^{-\mathbf{i}\mathbf{p}^{(n)}\eta(x_3-z_n)}\rangle\mathbf{W}^{(n)}] \tag{274}$$

with $S_{i3h}^{(n)\infty} = C_{ijkl}^{(n)} C_{pqmn}^{(k)} \epsilon_{lnh} b_m G_{kp,q}^{(k)\infty}(\mathbf{x} - \mathbf{x}')$, and the solution for the in-plane traction $\tilde{\mathbf{s}}^{(n)}$ is similar to that given by (274).

Perfectly bonded conditions along interfaces require that the traction and displacement (or tangential distortion) vectors are continuous. For interface n, this gives:

$$\overline{\mathbf{B}}^{(n)}\langle e^{-\mathbf{i}\bar{\mathbf{p}}^{(n)}\eta(z_n-z_{n-1})}\rangle\mathbf{V}^{(n)} + \mathbf{B}^{(n)}\mathbf{W}^{(n)} + \widetilde{S}_{i3h}^{(n)\infty}\big|_{x_3=0}$$

$$= \overline{\mathbf{B}}^{(n+1)}\mathbf{V}^{(n+1)} + \mathbf{B}^{(n+1)}\langle e^{-\mathbf{i}\mathbf{p}^{(n+1)}\eta(z_n-z_{n+1})}\rangle\mathbf{W}^{(n+1)} + \widetilde{S}_{i3h}^{(n+1)\infty}\big|_{x_3=0} \tag{275}$$

$$\overline{\mathbf{A}}^{(n)}\langle e^{-\mathbf{i}\bar{\mathbf{p}}^{(n)}\eta(z_n-z_{n-1})}\rangle\mathbf{V}^{(n)} + \mathbf{A}^{(n)}\mathbf{W}^{(n)},$$

$$= \overline{\mathbf{A}}^{(n+1)}\mathbf{V}^{(n+1)} + \mathbf{A}^{(n+1)}\langle e^{-\mathbf{i}\mathbf{p}^{(n+1)}\eta(z_n-z_{n+1})}\rangle\mathbf{W}^{(n+1)} \tag{276}$$

With all interface, bottom and top layer (half-space or free surface) boundary conditions, a system of algebraic equations can be formed. Solving these equations, the elastic field is fully determined.

4.3.4.4. Peach-Koehler Forces in Layered Materials

We give here an example of a 3D dislocation loop of a simple circular geometry to verify the present line integral method, and to illustrate the main characteristics of dislocation fields near interfaces.

Consider a circular dislocation loop in a half-space substrate. The loop lies near a free surface or an interface, as shown in Fig. 15. To be specific, we take the substrate material, which extends for all $z < 0$, to be an anisotropic aluminum crystal. The aluminum substrate is bound by a free surface or is perfectly bonded with an anisotropic nickel half-space along the surface $z = 0$. Both Al and Ni are fcc cubic anisotropic crystals, with their crystallographic axes [100], [010], and [001] lined up along the $x = 1$, $y = 2$, and $z = 3$ coordinate axes, respectively. The elastic constants needed for the present calculations are obtained from reference [225]. The circular dislocation loop lies on the (111) plane, its Burger's vector **b** is taken along the [1$\bar{1}$0] direction. The loop radius, R = 200 b, and its center is located at z = −180 b, where b = |**b**| is the magnitude of the Burgers vector of aluminum. For verification of the present line integral results, we show in Fig. 16 the results of stress field components for infinite space and the exact surface integral solutions. Calculations of surface integral, with Eq. (235) as the starting point, are performed using an evaluation of Green's functions and their derivatives in the corresponding materials [228]. We follow the procedure of Pan and coworkers for the numerical determination of Green's functions in anisotropic bi-materials and multilayered materials [220, 223]. Stress components along the z-axis, induced by the dislocation loop, are shown in Fig. 16a for the case of free surface and Fig. 16b for the interface case. Because of symmetry, $\sigma_{11} = -\sigma_{22}$, $\sigma_{13} = -\sigma_{23}$, $\sigma_{12} = \sigma_{33} = 0$, and thus we only show the stress components σ_{22} and σ_{23}. It can be observed from the figures that the numerical results of the present line integral method are nearly identical to those obtained by the surface integration method [228] for the case of a dislocation in half-space, and are in good agreement when the dislocation loop is near the interface. As the dislocation loop approaches the free surface, the out-of-plane stress components are forced to decrease till they become identically zero at the surface. However, in-plane stresses increase in order to satisfy overall equilibrium. When the aluminum substrate is bonded to a harder half-space (e.g., nickel), out-of-plane stresses are continuous across the interface, and larger than their corresponding values in infinite space. In-plane stress components, on the other hand, experience jumps because of the discontinuity in the elastic properties across the interface. The magnitude of stress increases across the interface, moving from the softer (aluminum) to the harder substrate (nickel).

In general, the stresses near a free surface are larger than their corresponding values near an interface to a harder material. The influence of the interface on the disturbance of the elastic field is somewhat local, and is limited to within a distance of a few hundred lattice constants from the free surface or an interface.

4.3.4.5. Dislocation-Interface Interaction

Dislocations move along the direction of the Peach-Koehler force exerted on them by the local elastic field, which of course includes image stresses due to interfaces in addition to applied and self-forces. The speed of the motion is controlled by the overall mobility, however, and that may include many contributions from interactions with electrons, phonons or other dispersed barriers. Complex DD
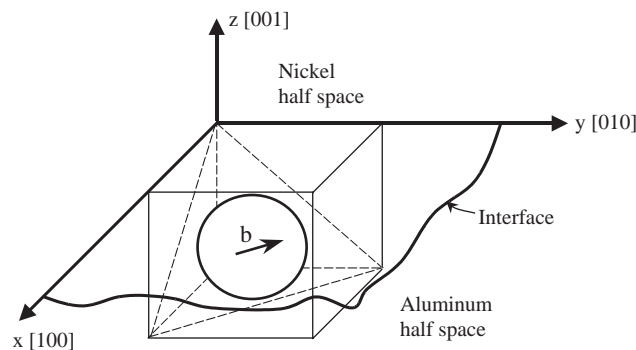
Figure 15. Schematic for the geometry of a 3D circular dislocation loop near an interface or free surface.
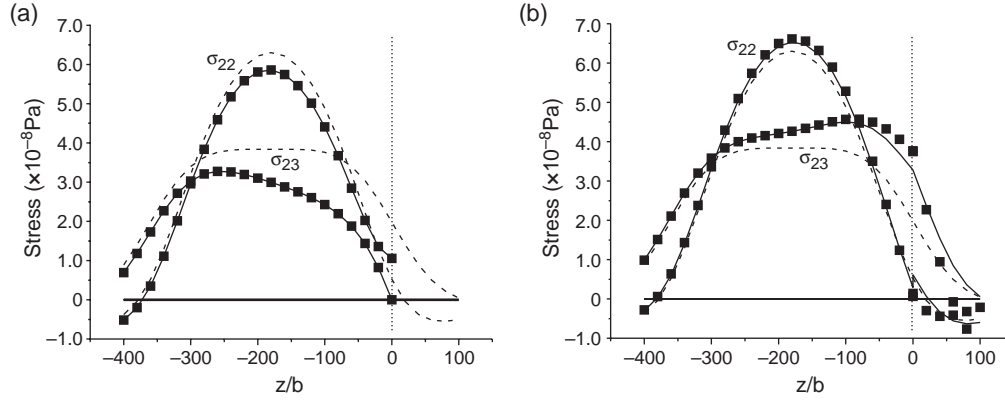
Figure 16. Stress components along the z-axis for a circular dislocation loop (see Figure (15)) in (a) Al half-space and (b) Al-Ni bi-material. Solid lines represent surface integral results, small square symbols: line integral results, and dashed lines: infinite space solutions.

simulations typically solve for the motion of interacting dislocation ensembles. In this section, we focus on understanding the influence of image forces due to interfaces or free surfaces on the magnitude and distribution of the Peach-Koehler force. This is given by: $\mathbf{f} = \boldsymbol{\sigma} \cdot \mathbf{b} \times d\mathbf{l}$, where the virtual force $\mathbf{f}$ is exerted on a line segment $d\mathbf{l}$ with the Burgers vector $\mathbf{b}$, and situated in the stress field $\boldsymbol{\sigma}$. The stress field may originate from various sources, such as applied forces, residual stresses, image stresses (due to boundary conditions), other dislocations, and even the dislocation loop itself (self-forces).

When a dislocation resides in a finite medium, adjustments of the stress field to satisfy surface or interface boundary conditions result in local changes of the stress tensor close to the dislocation line. Thus, calculations of the self-force for this altered stress field, which requires integrals along the dislocation line, would also include the influence of the boundary adjustment. Thus, the self-force would subsume the image effects of the boundary, and would be geometry dependent. To remove such ambiguities, and to determine clearly the effects of the interface or boundary, the stress field induced by a dislocation is divided into two parts: the full-space stress $\boldsymbol{\sigma}^{\infty}$ and the image stress $\boldsymbol{\sigma}^{C}$. The stress $\boldsymbol{\sigma}^{\infty}$ corresponds to that induced by the dislocation in a homogeneous and infinite space, with elastic properties of the material where most of the dislocation resides. The stress field $\boldsymbol{\sigma}^{\infty}$ of a dislocation in an infinite anisotropic material can be calculated by the line integral given by Eq. (226), and will induce a *self-force* on the dislocation. Because of the singularity of $\boldsymbol{\sigma}^{\infty}$ along the dislocation line, an average field is obtained by the Brown procedure [230] or alternatively through the Gavazza-Barnett limiting process [203]. Details of the numerical procedure for the stress field and self-force of a dislocation loop in an infinite anisotropic material are found in our recent work [226]. The force induced by the complementary part of the stress field, $\boldsymbol{\sigma}^{C}$, which reflects the interface effect on modifying the infinite medium stress field of the dislocation, will be termed henceforth the *image force* and is calculated directly by the Peach-Koehler formula.

We illustrate here the effects of free surfaces and interfaces on dislocation image forces for a typical dislocation configuration in an Al film, of width h, on a Cu substrate. The system will is modeled as a thin film that is perfectly bonded to a half-space. The Al film may have a free surface (e.g., an unoxidized film in vacuum), or is capped by a thin Al_2O_3 layer of width h_c. An oblong dislocation loop is located on the {111}-plane in the middle of the Al film, and has a Burgers vector of $\mathbf{b} = \frac{a}{2}\langle 1\bar{1}0\rangle$, and a is the lattice constant, as shown in Fig. 17. The oblong loop is composed of two straight segments parallel to the interfaces, which typically result from interface image forces as will be shown later, and are connected by two half-circular segments. The length (straight section) and width of the oblong dislocation are L and D, respectively, with $L = 2D$ and $D = h$. The distribution of image forces on the loop is shown in Figs. 17a through 17c for different thicknesses of the capped layer. The image force per unit length in these figures is normalized by $b^2 \times 10^{10}(Pa)/h$.
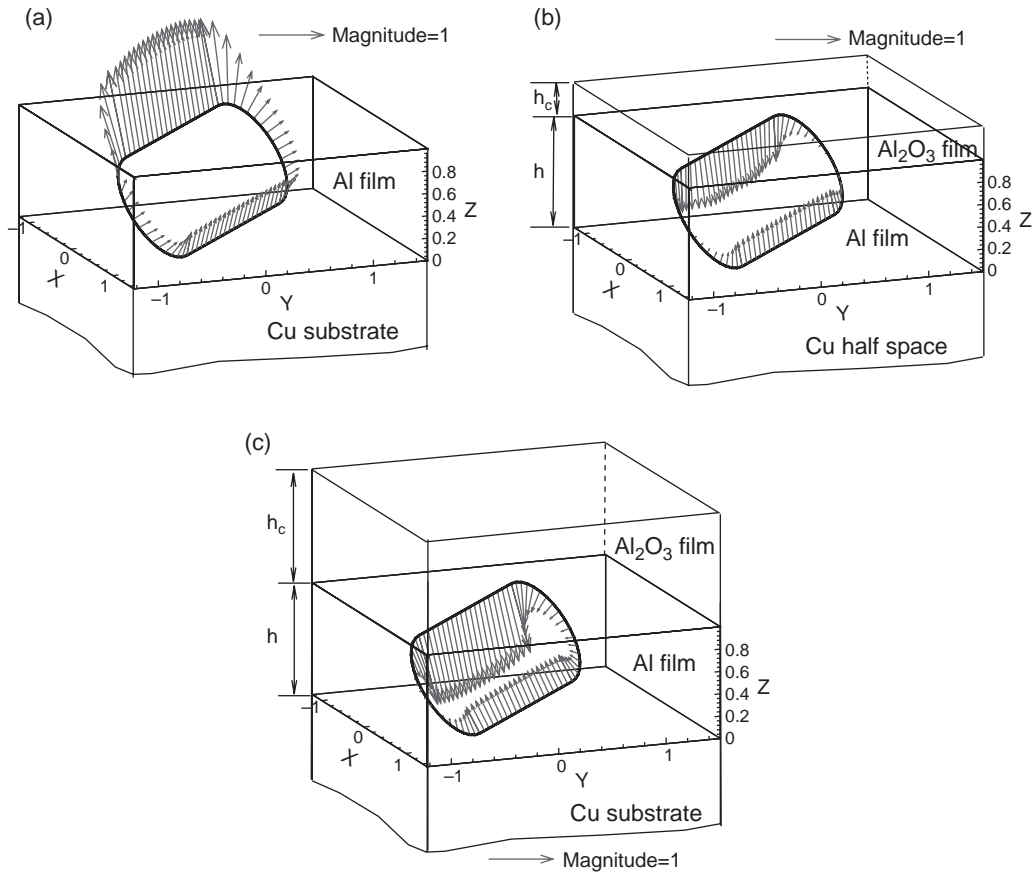
Figure 17. Image force distribution on an oblong dislocation loop in a (a) thin Al layer on a Cu substrate with (b and c) an additional aluminum oxide film on top. The layer is capped with an Al_2O_3 film of thickness (b) $h_c = 0.1$ h and (c) 1.0 h.

The image force distribution on the straight dislocation segment closest to the free surface is attractive, as one expects. However, its magnitude and direction cannot be obtained through a simple geometric construction by reflecting the dislocation loop across the interface. It is seen from Fig. 17a that the image force on the loop switches from attractive near the free surface to repulsive near the harder Cu substrate. When the Al film is capped by a harder oxide layer, the image force is found to have a strong dependence on the capping layer thickness, as long as it is less than the thickness of the thin film itself. Thus, for a thin film capped with several thinner layers, the image force would have major contributions from several neighboring interfaces. When the thickness of the capping layer is larger than the film thickness, as shown in Fig. 17c, the distribution of the image force tends to that generated by a semi-infinite medium. It is interesting to note that while the dislocation loop is attracted to the free surface, which would accelerate the formation of a surface step, it is repelled by the harder oxide film. A very thin oxide layer ($h_c = 0.1h$), as shown in Fig. 17b, almost balances the repulsive Cu interface forces on the middle curved sections of the loop rendering them force-free. This result cannot be expected from geometric image constructions as well.

5. Applications of Nanomechanics and Micromechanics

5.1. *Ab Initio*

Electronic structure calculations based on DFT also can be applied for studies of nonperiodic systems, such as those containing point, planar, or line defects or quantum dots if a periodic supercell is used. The supercell contains the defect surrounded by a region of bulk crystal or vacuum for the case of a surface. Periodic boundary conditions are applied to

the supercell so that the supercell is reproduced throughout space. It is essential to include enough bulk solid (or vacuum) in the supercell to prevent the defects in neighboring cells from interacting appreciably with each other. The independence of defects in neighboring cells can be checked by increasing the volume of the supercell until the calculated defect energy is converged. Using the supercell geometry one can study even molecules [231], provided that the supercell is large enough so that the interactions between the molecules are negligible.

   Ab initio calculations have recently been applied to study the dislocation core properties of isolated ⟨111⟩ screw dislocations in bcc Mo and Ta [232]. Alternatively, the semidiscrete variational Peierls-Nabarro (SVPN) model has come to serve as a link between atomistic and continuum approaches, by providing a means to incorporate information obtained from *ab initio* calculations directly into continuum models [233–235]. This approach has been shown to predict reliable dislocation core properties by comparing its predictions to direct atomistic simulations based on the same force law as that used for the γ-surface calculations [233]. The uniqueness of the approach when combined with *ab initio* calculations for the energetics is that it produces essentially an atomistic simulation for dislocation core properties without suffering from the uncertainties associated with empirical potentials. For example, atomistic simulations based on EAM potentials predict that dislocations in Al will dissociate into partials while experimentally no such dissociation is observed, a discrepancy which can be traced to the fact the EAM potentials underestimate the intrinsic stacking fault energy [233].

   In the SVPN approach, the equilibrium structure of a dislocation is obtained by minimizing the dislocation energy functional

$$U_{\text{disl}} = U_{\text{elastic}} + U_{\text{misfit}} + U_{\text{stress}} + Kb^2 \ln L \qquad (277)$$

with respect to the dislocation displacement density [233]. The γ-surface determined from *ab initio* calculations enters the equation through the U_{misfit} term. We identify the dislocation configuration-dependent part of the elastic energy and the misfit energy as the core energy, $U_{\text{core}} = U_{\text{elastic}} + U_{\text{misfit}}$, while the configuration-independent part of the elastic energy $Kb^2 \ln L$ is excluded because it is irrelevant in the variational procedure and it has no contribution to the dislocation core structure. The response of a dislocation to an applied stress is achieved by the minimization of the energy functional at the given value of the applied stress. An instability is reached when an optimal solution for the density distribution no longer exists, which is manifested numerically by the failure of the minimization procedure to convergence. The Peierls stress is then defined as the critical value of the applied stress giving rise to this instability. The resultant approach can then be applied to problems associated with dislocation core structure and the cross process, that neither atomistic nor conventional continuum models could handle separately. Therefore, this approach is particularly useful for studying the interaction of impurities with dislocations when empirical potentials are either not available or not reliable to deal with such multielement systems. Furthermore, it allows to study general trends in dislocation core properties and to correlate them with specific features of the underlying electronic structure.

5.1.1. Hydrogen Enhanced Local Plasticity

One of the first successful applications of this approach was the elucidation of the atomistic mechanism responsible for the hydrogen-enhanced local plasticity (HELP) in aluminum [234]. The γ-surface for both the pure Al and the Al + H system, shown in Figs. 18a and 18b, respectively, indicate an overall reduction in energy in the presence of H. This in turn not only facilitates dislocation emission from the crack tip but also enhances the dislocation mobility dramatically. The H is found to bind strongly to dislocation cores and that the binding energy is a function of dislocation character. These findings explain the experimentally observed restriction of the cross-slip process and slip planarity in the presence of H. The dislocations do not dissociate into partials even though the intrinsic stacking fault energy is reduced by 40% in the presence of H.
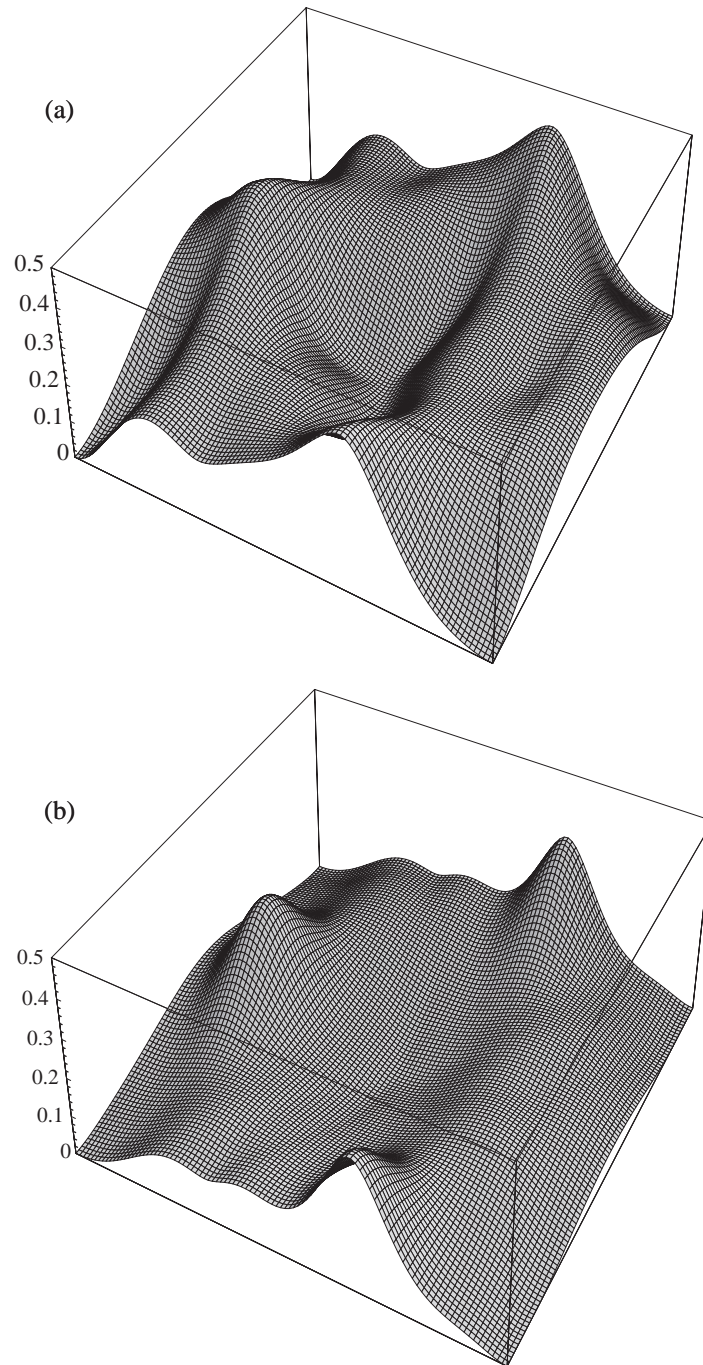
Figure 18. The γ surfaces: J/m^2 for displacements along a (111) plane for (a) pure Al and (b) Al + H systems. After Lu et al. (2001).

5.1.2. Dislocation Cross-slip

Recently, the SVPN was extended to take into account two intersecting slip planes, thus allowing the study of cross-slip properties [235, 236]. This novel model was applied to study the dislocation constriction and cross-slip process in two fcc metals, Al and Ag, exhibiting different deformation properties. The results of the dislocation density $\rho(x)$ in the primary and cross-slip planes for Al and Ag are presented in Figures XXX and XXX, respectively. The screw dislocation in Al which starts out at the primary plane spontaneously spreads into the cross-slip plane, as the density peak at the cross-slip plane indicates. As expected, the edge component of the density is zero at the cross-slip plane because only the screw
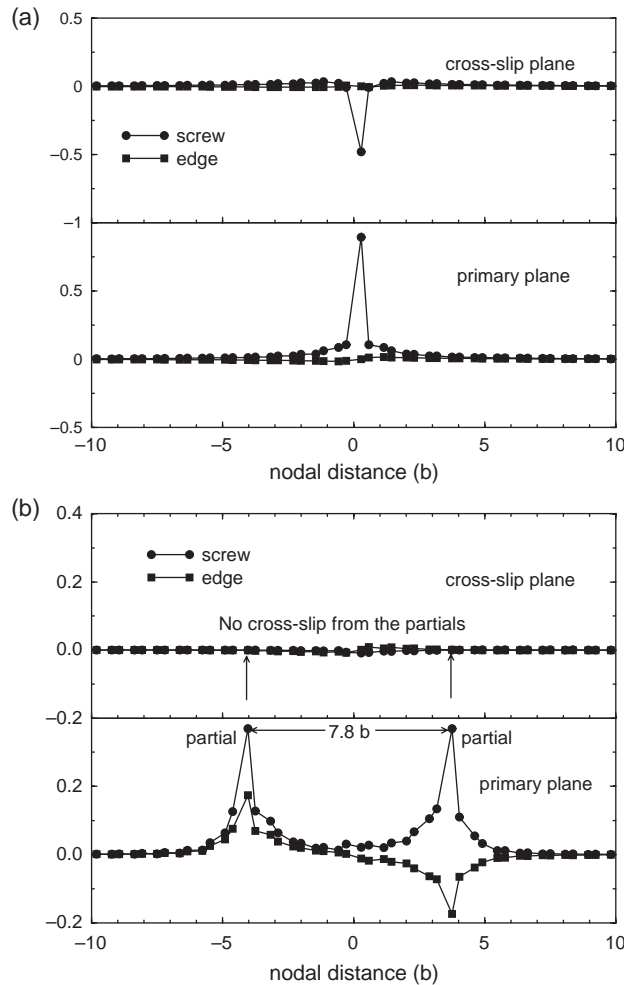
Figure 19. Dislocation displacement density $\rho(x)$ for (a) Al and (b) Ag. The peaks in the density plot in Fig. 7b represent partial dislocations.

displacement can cross-slip. On the other hand, the screw dislocation in Ag dissociates into two partials, separated by 7.8 b ($\approx$22 Å), in excellent agreement with the experimental value of 20 Å in TEM measurements [237]. The left (right) partial has a positive (negative) edge component of the Burgers vector represented by the positive (negative) density. The integral of the edge density over all atomic sites is zero, corresponding to a pure screw dislocation. These partial dislocations cannot cross-slip, as the arrows in Fig. 3a indicate, without first annihilating their edge components, and the dislocation density on the cross-slip plane is essentially zero. Apparently, the lack of obvious dissociation in Al stems from the fact that Al has a much higher intrinsic stacking fault energy than Ag. The absence of obvious dissociation into partials in Al is also consistent with experiment [238].

5.1.3. Dislocation Core Properties

The strengthening of alloys relative to pure metals has been a subject of technological and scientific interest for centuries. Al-Cu alloys are the oldest in which age hardening has been understood to arise from solute precipitation. In age-hardened solid solution alloys small amounts of solute element (e.g., Cu) are added to the pure metal (e.g., Al) at high temperatures (where there is solubility) and the alloy is quenched down in temperature. With time the supersaturated solute atoms begin to precipitate. The aged alloy becomes stronger because dislocation motion through the crystal is impeded by the precipitate itself and by the elastic strain field surrounding the precipitate. These crystallographically coherent
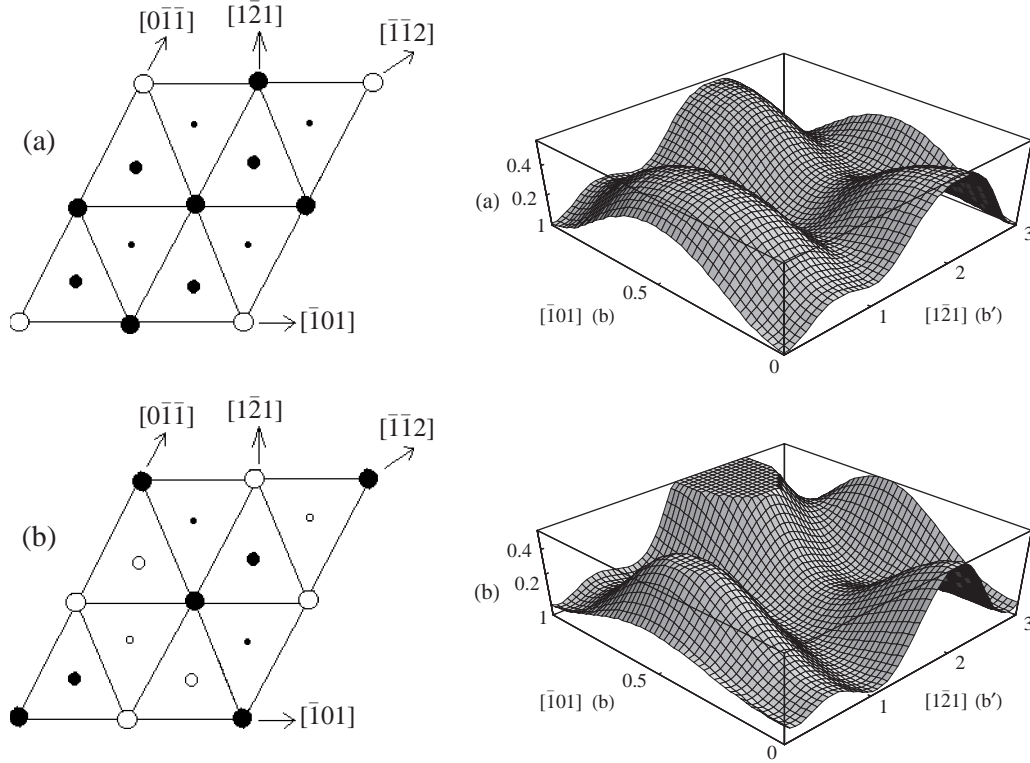
Figure 20. Left panel: positions of atoms for three successive (111) layers for the Al-Cu case (a) where one Al atom on the shear plane has been substituted with a Cu atom; and for the Al-Cu case (b) consisting of the $L1_0$ structure, with alternating Al and Cu (001) planes. The large, medium, and small circles represent atoms in the three (111) planes, respectively. Open (closed) circles denote Cu (Al) atoms. Right panel: The GSF energy surface for displacements on a (111) plane for the Al-Cu case (a) and for the Al-Cu case (b).

precipitates (i.e., without dislocations between the precipitates and the matrix) are collectively known as Guinier-Preston (GP) zones [239, 240].

The GP zones are metastable phases, with a long relaxation time. In the Al-Cu system the Cu atoms coherently precipitate in the {100} planes of the Al matrix. The shape and size of the precipitates has been a subject of long experimental and theoretical study. The coherent precipitation sequence was determined in the 50's as solid solution GP1 GP2. There has been some controversy as to what the structure of the GP zones is, but the following is usually accepted: GP1 is a single, almost pure, (100) Cu layer formed in the initial stages of precipitation; GP2 is primarily (but not only) an ordered platelet of two Cu 100 planes separated by three 100 planes of Al. Such a an ordered structure for GP2 has been inferred both from superlattice reflections in x-ray measurements [241], and from first-principles thermodynamic calculations [242]. While the Al_3Cu_1 was found to be the most stable, the Al_1Cu_1 ($L1_0$) ordered structure is very close in energy. We have used the latter structure to model the GP zone since it involves smaller supercells and hence is computationally less expensive.

To simulate the block shearing process, we employ a supercell consisting of six atomic layers in the $\langle 111 \rangle$ direction. We have considered two different cases of alloying: In the first case, which we will refer to as Al-Cu(a), we substitute one Al atom with a Cu atom on the shear layer, i.e. the shear plane consists of one Cu atom and three Al atoms with all other layers being pure Al (left panel in Fig. XXX. In the second case, which we will refer to as Al-Cu(b), each (111) layer consists of interchanging aluminum and copper chains along the $\langle 112 \rangle$ direction (left panel in Fig. XXX. The second case corresponds to the $L1_0$ ordered intermetallic with alternating Al and Cu (001) planes. The calculations were performed at the theoretically equilibrium lattice constant $a = 4.0$ Å of pure Al, since the content of Cu in the alloys under study is about 1-2% and the Cu precipitates in the Al matrix are coherent.

The generalized stacking fault energy (GSF) (γ surface) for both the Al-Cu(a) and Al-Cu(b) cases is shown in the right panels of Figures XXX and XXX, respectively. For Al-Cu(a) the intrinsic stacking fault (ISF) energy is reduced to 0.122 J/m^2 from the value of 0.164 J/m^2 in pure Al. The unstable-stacking energy is also reduced slightly from 0.224 J/m^2 for pure Al to 0.175 J/m^2. For Al-Cu(b) the GSF energy surface changes dramatically compared to that of pure Al. The ISF energy vanishes along [112] and in fact becomes negative -0.102 J/m^2 along the [121] direction. The average of the two values compares well with the value of about -0.050 J/m^2 for the 50 at.% random Al-Cu alloy [243].

For Al-Cu(a) the core energy for all four dislocations is higher than that for the pure Al case. We find that the Peierls stress for the screw, 30°, 60° dislocations is lower than for the pure Al case. On the other hand, the Peierls stress for the edge dislocation is an order of magnitude higher than that for the pure Al, which is probably due to the fact that the edge dislocation dissociates into partials for Al-Cu(a). In sharp contrast, all four dislocations for the Al-Cu(b) system have lower core energies than for Al-Cu(a), and the Peierls stress of all is an order of magnitude higher than that for Al-Cu(a), suggesting a strengthening mechanism.

5.2. MD Simulations

Applications of MD simulations to the nanomechanics of point defects, dislocations, and interfaces (free surfaces and grain boundaries) under applied stress will be presented in this section. Under stress, the normal diffusion process governed by point defect motion is polarized by the action of the stress field. The diffusion process of a point defect has been investigated by a combination of molecular statics (MS) and MD simulations. Diffusion anisotropy, which is intrinsic in low symmetry crystals, can be enhanced by the action of stress [244]. The stress effect on a point defect, particularly its formation and migration energies, is crucial to the analysis of kinetic processes, but this is usually not a first order effect in nanomechanics.

5.2.1. Dislocation Motion

MD simulations of dislocation mechanics has received much attention in recent years because of the importance of dislocations in plasticity and fracture. In dislocation statics, one is primarily concerned with the final core structure of one or a few dislocations. The discovery of three-fold symmetry of the screw dislocation in bcc metals is a direct result of the applications of dislocation statics [245–249]. MD simulations have provided much insight to details of kink-kink [250], dislocation-dislocation [251–254], dislocation-point-defect [255], and dislocation-grain boundary [87]. In the transonic velocity range, MD simulations have revealed new mechanisms and possibilities. Gumbsch and Gao [256] demonstrated that transonic dislocations are possible. Later, it was shown that a transonic dislocation can cross the sound barrier back and forth [257, 258]. The availability of fast dislocations also enabled the study of dislocation dipole stability at the atomic level [259], to serve as direct confirmation of the elasticity analysis [260]. As shown in Fig. 21, the simulations further reveal that a dislocation dipole can be stabilized even with an overshoot; a direct result of the finite speed of wave propagation.

MD simulations have also been applied in studies of dislocation emission from crack tips [261], nucleation of dislocations from surfaces [262, 263], and dislocation nucleation in nanocrystals [264, 265]. One of the challenging problems that remain is treating the interaction of boundaries with elastic waves emitted by moving dislocation. Several recent studies have attempted to dampen out boundary effects [94, 95, 259], but the problem is still not satisfactorily solved.

5.2.2. Grain Growth

Similar to point defects and dislocations, interfaces (e.g., surfaces and grain boundaries) respond to mechanical loading. In connection with dislocations, surfaces are nucleation sites. Although grain boundaries also have this function, they are more crucial in facilitating or blocking other deformation mechanisms. Using a multiscale approach, [87] have studied the
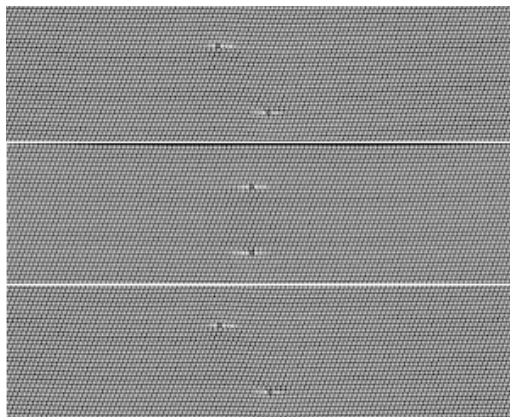
Figure 21. Three snapshots of a pair of edge dislocations in a dipole configuration, showing the stabilization of a dipole despite the dynamic overshoot. After [259].

interaction of a dislocation with a grain boundary. It is well established that grain boundaries serve as barriers to dislocation motion and give rise to the Hall-Petch effect, which shows that the strength of materials is inversely proportional to the square root of its grain size. However, for materials with grain sizes below a few nanometers, materials strength begins to decline when the grain size decreases [266]. At the nanoscale, grain boundaries facilitate mechanical deformation through grain boundary sliding. At the same time, the grain structure evolves as well, and this evolution in turn affects the mechanical deformation. Taking thin slices of polycrystalline nano-grains, Wolf and co-workers [267, 268] have investigated mechanisms of grain boundaries interactions. As shown in Fig. 22, high-angle grain boundaries shrink and that quadruple junctions are not stable and are reduced to triple junctions.

Identification of dislocations in MD simulations is straightforward if the dislocation configuration is simple. One may rely on constructing the Burgers circuit, using disregistry functions (such as the centro-symmetry parameter), or tracking the atomic level stress or energy [269–271]. When complex dislocation configurations are involved, unambiguous identification of dislocation cores may require a combination of several of the methods discussed above. Before closing this section, let's examine the type of information that can be passed on to larger length scales. Here, we consider three types of defects: point defect, dislocation, and interface (particularly grain boundary). Information on defect energetics and diffusion tensors obtained by MD or MS simulations provide parameters to rate equations and Monte Carlo methods describing microstructure evolutions. Dislocation energetics (e.g., kink-pair formation energy and dislocation core energy), Peierls stress and dislocation mobility are used as input parameters in dislocation dynamics simulations at the mesoscopic level [261]. Finally, dislocation nucleation conditions and interaction mechanisms with other defects (dislocations or grain boundaries or other interfaces) from MD simulations are critical to dislocation dynamics simulations.

5.2.3. Nanostrength

5.3. KMC Applications

5.3.1. Dislocation Decoration

Because of the significance of the effects of glissile SIA clusters on damage evolution, we first establish the dynamics of their motion in the field of grown-in dislocations. The values of the migration energy, diffusion pre-factors, and other input parameters for SIA diffusion used in this work are listed in Table 3 [119, 272]. A computational cell of $400a \times 400a \times 400a$ ($a = 2.867$ Å is the lattice constant) is used with periodic boundary conditions. The ratio of activation energy for Burgers rotation to the 1D migration energy is set to be 8. A slip dislocation loop lying on the $\langle 101 \rangle$ plane, with Burgers vector $\mathbf{b} = \frac{1}{2}\langle \bar{1}11 \rangle$ is introduced into the simulation box. The dislocation loop consists of two curved segments and two straight super-jog segments that are normal to the loop's Burgers vector. A number of SIA clusters
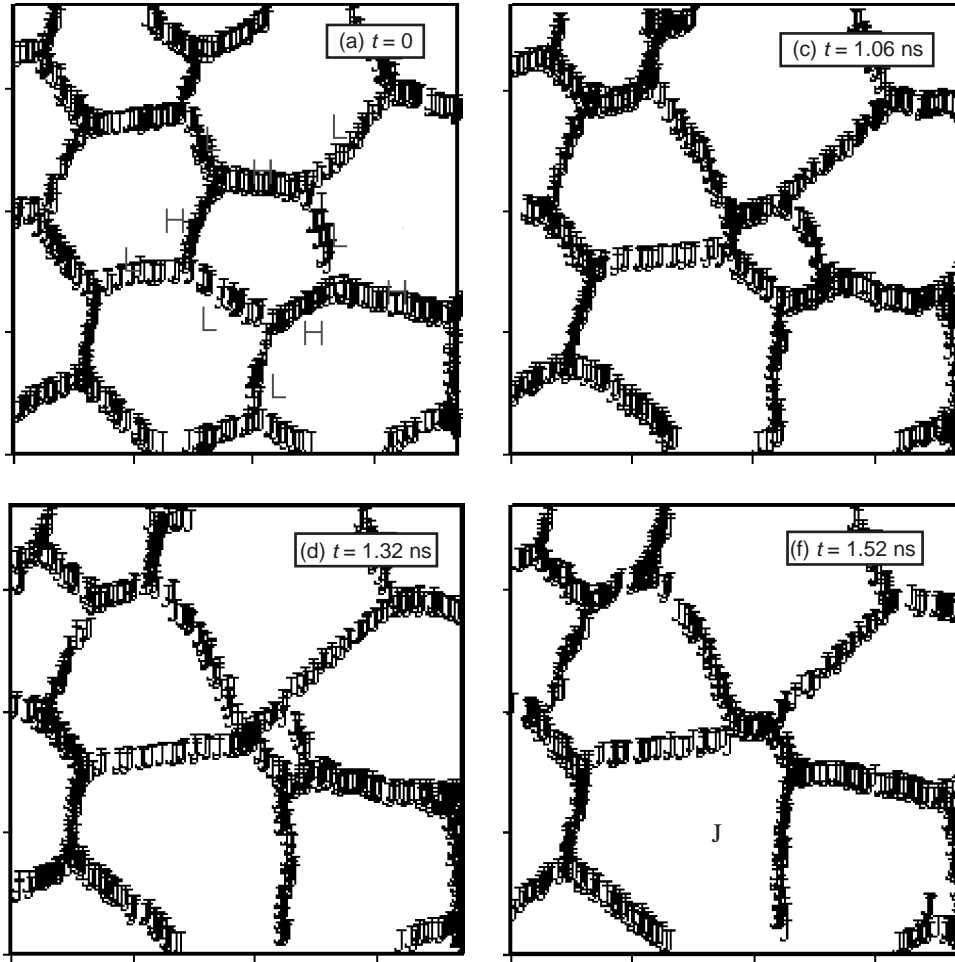
Figure 22. MD simulations of nanoscale grain boundary evolution under externally applied stress. Time is labeled in each frame. "H" indicates high-angle, and "L" low-angle grain boundary. After [268], courtesy of D. Wolf.

with the same size, R, were initially randomly distributed in the simulation box, and their initial jump directions were also randomly specified. The initial SIA cluster density was varied in the range 5×10^{22} to 2×10^{23} m^{-3}. When a cluster approaches the dislocation loop at distances closer than the standoff distance (taken as 1.5 nm), the cluster is stopped, and all events related to it are removed from the event table. When two SIA clusters approach one another within one atomic distance, they coalesce and make a larger cluster.

One of the most striking features in the evolution of dislocation microstructure under cascade damage conditions is the decoration of grown-in dislocations by loops [273, 274], which may even extend to form dislocation walls [274]. Most dislocations are observed to be heavily decorated by small, sessile interstitial clusters [275]. Figure 24 shows a TEM micrograph of pure iron irradiated with fission neutrons at about 70°C [276]. Grown-in (slip) dislocations are clearly decorated with small defect clusters, and the formation of loop rafts is significant.

5.3.2. Dislocation Pinning and Small Defect Rafts

To investigate the influence of cluster-cluster interactions on their motion, the grown-in dislocation was removed, and the elastic interaction between clusters included in a new KMC simulation. Mutual elastic interactions in between clusters was found to affect their

Table 3. Parameters used in the current simulations.

E_m(eV)	a(Å)	$R(a)$	T(K)	$\omega_0(\text{s}^{-1})$	G(GPa)	ν
0.02	2.867	3.0	300.0	2.5×10^{13}	81.8	0.29
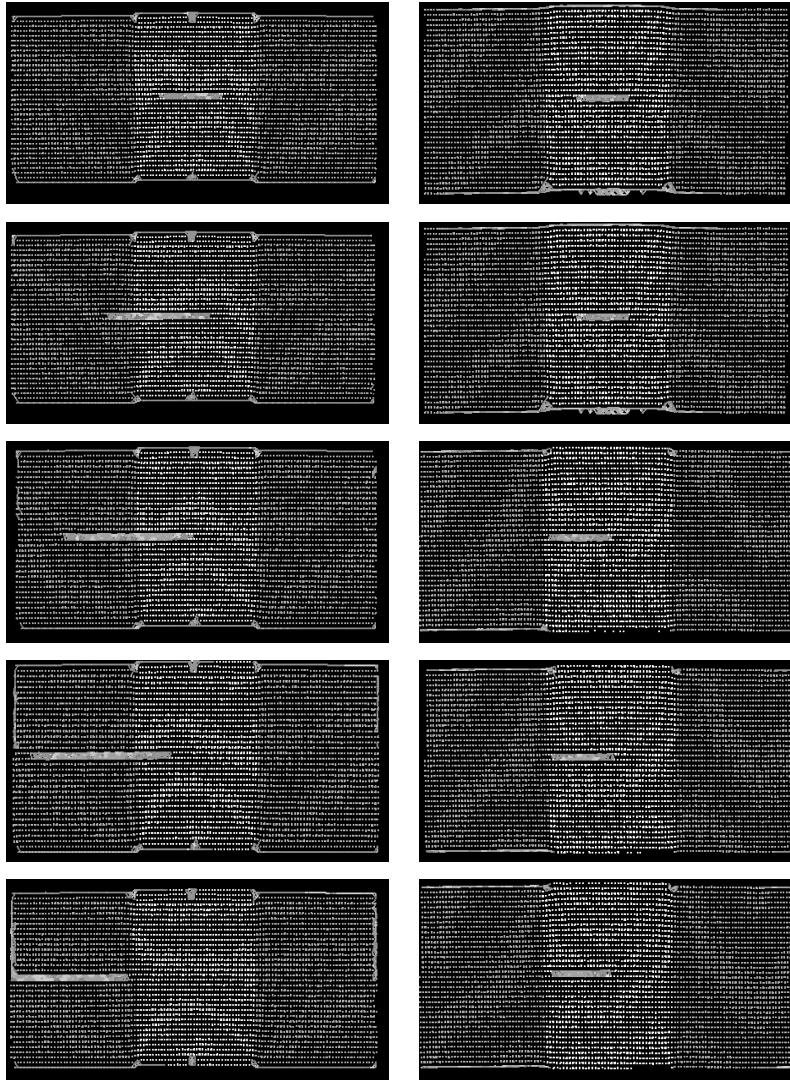
Figure 23. Snapshots of a dislocation in Cu-Ni nanolayers. Left: the dislocation is in Ni, and the applied shear stress is 400 MPa. Right: the dislocation is originally in Cu, and the applied shear stress is 800 MPa. Courtesy Lan Li, UCLA.

distribution and motion drastically. Because of mutual interaction, two clusters that are oriented along nonparallel crystallographic orientations will either coalesce forming a larger one, or rotate and pin one another at a short distance and move jointly in the same direction. Once two clusters are pinned together, they have less chance to change their orientation, and therefore their motion becomes almost pure one-dimensional. As this process proceeds, some additional clusters may be trapped into this pinned structure by changing their Burgers vectors. This self-organizing mechanism eventually results in the occurrence of SIA *rafts*, which consist of a number of small dislocation loops with the same direction of motion. This feature has been experimentally observed for some time [277].

A simulation of cluster motion integrating the influence of the internal stress field created by grown-in dislocations, as well as the clusters themselves was also performed. Figure 25 shows a typical defect evolution time sequence for 200 SIA clusters at 300 K. The effects of internal dislocation fields, aided by cluster mutual elastic interactions, rendered most of the clusters virtually immobile in the vicinity of the slip dislocation. Continuation of the decoration process results in the initiation of a "dislocation wall." Similar simulations were performed for smaller cluster density (50 SIA clusters), and also at higher temperature (600 K). The results indicate that SIA cluster density seems to have a greater influence on the transient time for decoration than temperature. Under higher temperature conditions,
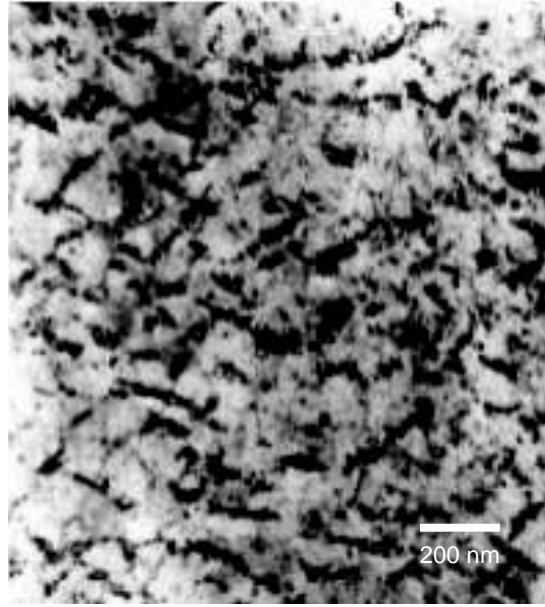
Figure 24. A TEM micrograph of pure Fe irradiated with fission neutrons at 70°C to a displacement dose level of 0.72 dpa [276].
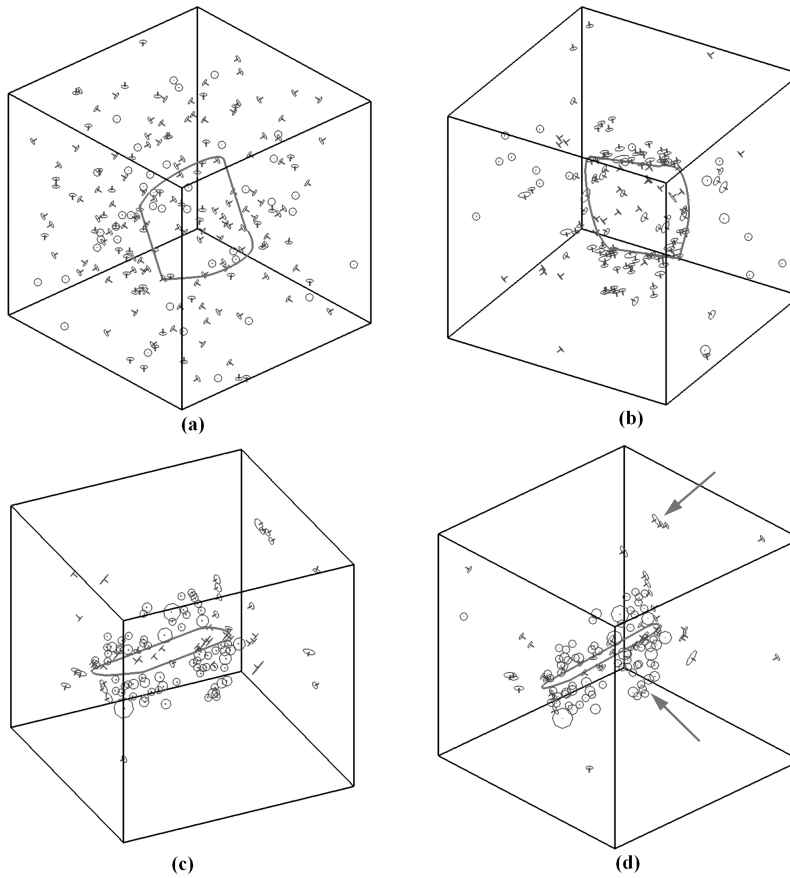
Figure 25. KMC simulation of 200 SIA clusters in the stress field of a 3D dislocation loop. Dislocation decoration and SIA cluster rafts are clearly observed, as indicated by the arrows. (a) 0 ns, (b) 0.4 ns, (3) 0.7 ns, (d) 1.0 ns.

we find that the formation of dislocation decorations is faster than at lower temperatures. The high temperature increases the thermal activities of clusters, which makes clusters have more chance to approach the reaction range of internal dislocations. The simulations also show that the *rafting* structure occurs more easily at lower temperatures.

5.3.2.1. Comparison with Experimental Data on Neutron-Irradiated Iron

We perform here KMC computer simulations for the microstructure evolution of pure Fe irradiated with fission neutrons at 300 K and compare the results to the experiments of Singh et al. [278] and Eldrup et al. [276]. The simulation conditions and procedures are first explained, followed by a discussion of the results.

Fitting MD-generated data for several metals, Bacon et al. [126] showed that the number of Frenkel pairs (N_F) is given by $N_F = A(E_{PKA})^m$, where A and m are constants, and E_{PKA} is the energy of the primary knock-on atom. On the other hand, the number of displaced atoms can be written as $N_P = PN_t$, where P is the displacement dose (dpa) and N_t the total number of atoms in the system. Therefore, the displacement dose level corresponding to one cascade can be readily calculated as:

$$P = \frac{N_F}{N_t} = \frac{A(E_{PKA})^m}{N_t} \tag{278}$$

With the relationship between the cascade energy and damage dose, we can determine the number and frequency of cascades required for producing a desired dose at a predetermined dose rate.

Point defect statistics for clusters generated by 40 KeV cascades in α-Fe (e.g., number, size distribution, and mobility) were taken from the MD simulations of Bacon, Gao and Osetsky [126]. Soneda and Diaz de la Rubia [121] have shown that two thirds of the defects that escape from the parent cascade region are in the form of small SIA clusters, which migrate in one dimension. Therefore, monodefects as well as relatively smaller clusters were ignored in the present simulations. Room temperature neutron irradiation of iron was simulated with a flux of 40 KeV cascades containing interstitial clusters of size >4 atoms.

It has been shown by MD simulations [279] that small loops consisting of four, five, and six atoms transform spontaneously from the faulted into the highly glissile unfaulted configuration. In addition, the change in the Burgers vector of a cluster consisting of four SIAs has been observed to occur in these studies. From the lifetime of one configuration, a value of 0.4 eV is estimated for the energy barrier against this transformation [279]. The height of the barrier for orientation change is expected to increase significantly with increasing cluster size. MD studies show that small, strongly bounded interstitial clusters (two to about five SIA clusters) exhibit long-range, three-dimensional (3D) diffusion, which occurs by reorientation of constituent $\langle 111 \rangle$ dumbbells from one $\langle 111 \rangle$ to another [272]. As the cluster size increases, thermal-activated reorientation from one Burgers vector to another becomes increasingly more difficult to achieve, no 3D motion is observed even at very high temperatures.

Osetsky et al. [119] developed a generalized size dependence of cluster jump frequency to describe the one-dimensional diffusional transport behavior of SIA clusters

$$\omega^n = \omega_0 n^{-S} \exp\left(-\frac{\langle E_m \rangle}{k_B T}\right) \tag{279}$$

where $\langle E_m \rangle$ is the averaged effective activation energy, n the number of SIAs in the cluster, and ω_0 is a new, size-independent, pre-exponential factor. The value of $\langle E_m \rangle$ was found not depending on size and close to that of the individual crowdion. It is estimated for clusters containing up to 91 SIAs in iron that $\langle E_m \rangle = 0.023 \pm 0.003$ eV for $\frac{1}{2}\langle 111 \rangle$ clusters in bcc iron. By fitting to the simulation results of various cases, the values $\omega_0 = 6.1 \times 10^{12}$ s^{-1}, $S = 0.66$ for Fe describe the MD data very well, and were used in our KMC simulations.

Soneda and Diaz de la Rubia [121] studied the direction change frequency of 2-SIA and 3-SIA clusters in α-Fe using MD simulations and obtained the activation energies of 0.09 eV and 0.27 eV for 2-SIA and 3-SIA clusters, respectively. Gao et al. [280] investigated possible transition states of interstitials and small interstitial clusters in SiC and α-Fe using

the *dimer method*. The activation energies of directional change were found to be 0.163, 0.133, and 0.342 eV for 1-, 2-, and 3-SIA clusters, respectively. In our work, we assume that the relationship between the activation energy of directional change for a interstitial cluster and the size of the cluster is linear, and is equal to 0.05 eV per interstitial atom. In fact, MD simulations have shown that the motion of small SIA clusters and loops is the result of the motion of individual crowdions [119, 126], and the reorientation may occur in a one-by-one fashion [281]. The value of 0.05 eV/atom is probably an underestimation for the energy barrier for direction change of a small cluster, say size less than four, but for larger clusters, it reflects the preferential 1D motion of large interstitial clusters. MD simulations revealed that defect structure of a cascade is characterized by a vacancy-rich core surrounded by a shell of SIA clusters. We represent this vacancy-rich core region as an immobile spherical recombination center. The size of a recombination center or nano-void is given by an equivalent diameter. The number of vacancies in the core of a cascade is assumed to follow a Gaussian distribution with mean value of 100 and a standard deviation of 8 vacancies.

5.3.3. Dose Dependence of Defect Density in Irradiated Materials

Doses up to 5.21×10^{-3} dpa were simulated at a displacement damage rate of 5×10^{-8} dpa/s, and damage accumulation was studied as a function of dose. Figure 26 shows the interstitial cluster density as a function of dose with and without recombination between SIA clusters and nano-voids. In addition, SIA clusters containing more than 100 interstitial atoms (diameter >3 nm) are counted as visible defects. The corresponding cluster density is calculated and compared with experimental data for bcc Fe irradiated at $\simeq 70°C$ in the HFIR reactor at Oak Ridge National Laboratory to displacement dose levels in the range of 10^{-4} to 0.72 dpa [276], and for pure iron irradiated irradiated in the DR-3 reactor at Risø National Laboratory at 320 K as shown in Fig. 27. At initial stage (dpa $< 10^{-4}$ dpa), the cluster density increases almost linearly with damage dose. The increase in cluster density then slows down when the dose level is higher than 10^{-4} dpa. The cluster density approaches a saturated value and does not change much beyond a dose level of 3.5×10^{-3}.

At the beginning of irradiation, cluster densities of both interstitials and vacancies are rather low, and the chance that one interstitial cluster can get close enough to another interstitial or vacancy cluster is rather small as well. Because of the 1D motion of SIA clusters, the recombination cross section with vacancy clusters produced in the cascade core as well as the agglomeration cross section with other interstitial clusters are small. Theoretically, there are only two mechanisms by which a SIA cluster could change its direction of motion: either thermal activation or interaction with other defects or microstructure. The effect of thermal activation can be ruled out here because our simulation is carried out at a low
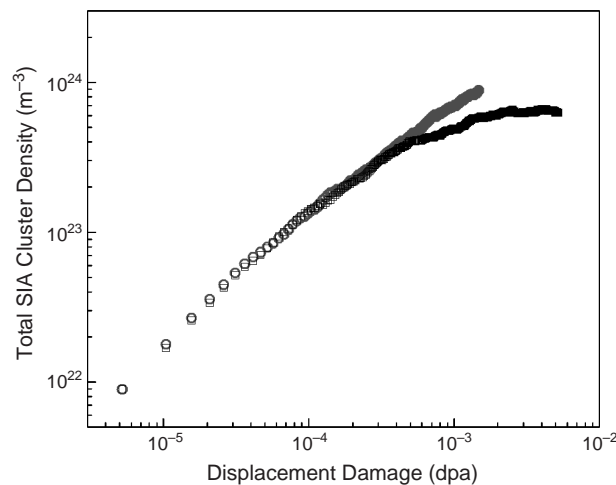
Figure 26. Dose dependence of the total SIA cluster density in bcc Fe: -○-, no recombination; -□- with recombination.
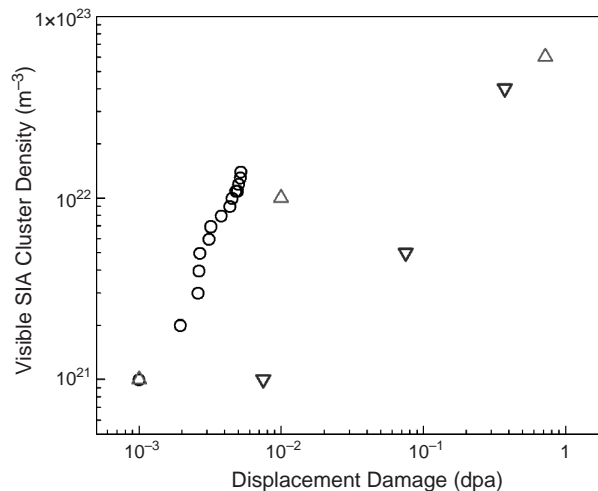
Figure 27. Dose dependence of the total visible SIA cluster density in bcc Fe: -○-, KMC simulation results; -△- experimental results of Eldrup et al.; -▽- experimental results of Singh et al. [276, 278].

temperature (i.e., room temperature). At low damage dose level, the large distance between clusters renders the interaction between them weak and can hardly affect their migration, thus the density of clusters increases linearly with dose.

When the damage builds up to an appreciable level, on the order of 10^{-4} dpa, the simulation box becomes crowded with defects. The probability of mutual interaction between clusters becomes appreciable, leading to more pronounced recombination and agglomeration events. Consequently, these ono-linear reactions slow down the increase in the density of SIA clusters. At higher accumulated damage levels, on the order of 3.5×10^{-3} dpa in the present case, the number of SIA clusters that recombine or coalesce reaches dynamic equilibrium with the number of clusters produced by fresh cascades. Then, SIA cluster density in the simulation box reaches a saturation level.

It is found that the presence of nano-voids has a significant effect on the evolution dynamics of SIA clusters. As we can see in Fig. 26, at a dose level lower than 5×10^{-4} dpa the difference between SIA cluster densities, with and without nanovoids, is not large. However, when nanovoids are included in the simulation, the surviving SIA cluster density deviates from the case when nanovoids are not included. For example, the density of surviving SIA clusters is less by a factor of 2 at 1.5×10^{-3} dpa, when nanovoids are included.

Although the density of SIA clusters reaches steady state after 3.5×10^{-3} dpa, SIA cluster sizes continue to grow, and the density of "visible" clusters increases as well. In order to compare the results from our simulations with experimentally measured cluster densities, it is necessary to assume a minimum size that can be resolved in experiments. A value between 1.5 and 2 nm in diameter is quoted in the literature as the minimum size resolved by TEM [282]. In the current simulations, we assume that SIA clusters containing more than 100 atoms are "visible." It is shown in Fig. 26 that the density of "visible" SIA clusters obtained in the simulations presented here is larger than the experimental measurement at high dose levels. The high mobility of SIA clusters allows them to be absorbed on other sinks, such as grain boundaries or free surfaces. In addition, impurities can play an important role in influencing the kinetics of damage buildup, and hence we can consider the agreement with the experimental conditions on the cluster density as qualitative rather than quantitative.

The size distribution of SIA clusters at a dose of 5.2×10^{-3} dpa is shown in Fig. 28. More than half of the total interstitial clusters consist of more than 30 defects, though small clusters consisting of less than 10 SIAs still have the largest concentration. It can expected that the size distribution will continue to shift to larger sizes as damage accumulates. It is found here that mobile SIA cluster can be immobilized, either by getting trapped near a dislocation or by getting locked with another large cluster (>37 SIAs) of a different Burgers vector.
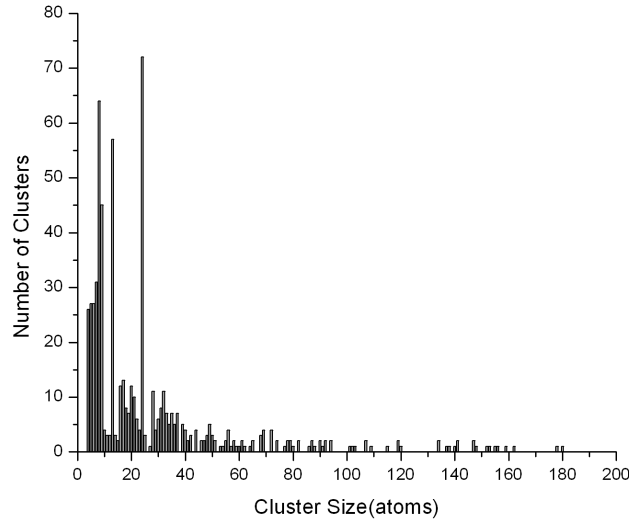
Figure 28. Size distribution of SIA clusters at a dose level of 5.21×10^{-3} dpa.

5.3.3.1. Characteristics of Decoration and Raft Formation
The dislocation decoration process builds up quickly with dose, and at 3×10^{-4} dpa the grown-in dislocation attracts a number of SIA clusters, and at higher doses dislocation decoration becomes very significant, as can be seen in Fig. 29. When an extremely mobile one-dimensionally migrating interstitial cluster passes through the neighborhood of a preexisting dislocation, it will feel the influence of the strain field of the dislocation. As long as the defect-dislocation interaction is attractive and the distance is small, the cluster cannot escape from the attractive zone by thermally activated random walk. Once a SIA cluster is trapped into the strain field of a dislocation, it will rotate its Burgers vector to accommodate to the strain field of the dislocation and tend to migrate along the direction of lowest energy barrier.

It can be clearly seen in Fig. 29b that the pure edge components of the slip dislocation attract more SIA clusters in its vicinity. Trapped clusters can still serve as sinks for the glissile clusters and increase their size before they rotate their Burgers vectors and finally get absorbed by dislocations. With the accumulation of clusters along the dislocation line, a repulsive force field is then gradually built up against further cluster trapping. Figure 30a shows contours of the interaction energy between an interstitial defect cluster of Burgers vector $a/2\langle\bar{1}11\rangle$ and an edge dislocation on the $(\bar{1}\bar{2}1)$-plane in bcc iron; and Fig. 30b shows contours of the interaction energy between an interstitial defect cluster of Burgers vector $a/2\langle\bar{1}11\rangle$ and a pre-existing same-type cluster and an edge dislocation on the $(\bar{1}\bar{2}1)$-plane.
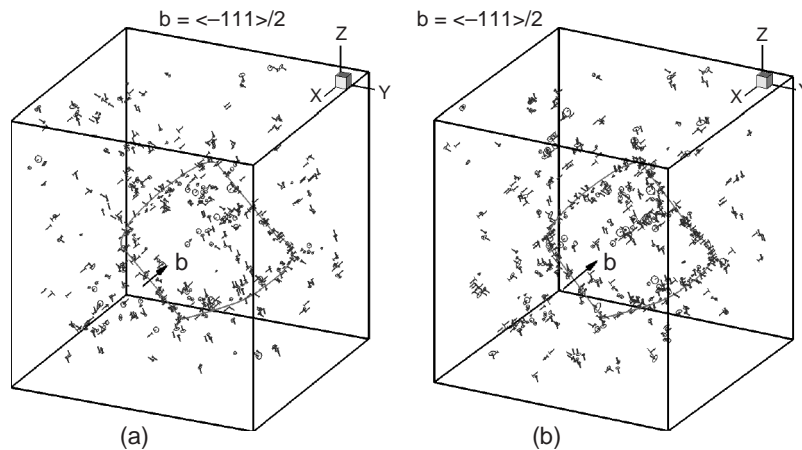
Figure 29. Spatial distribution of SIA clusters in bcc Fe at 300 K: (a) 1.3×10^{-3} dpa, (b) 5.2×10^{-3}.
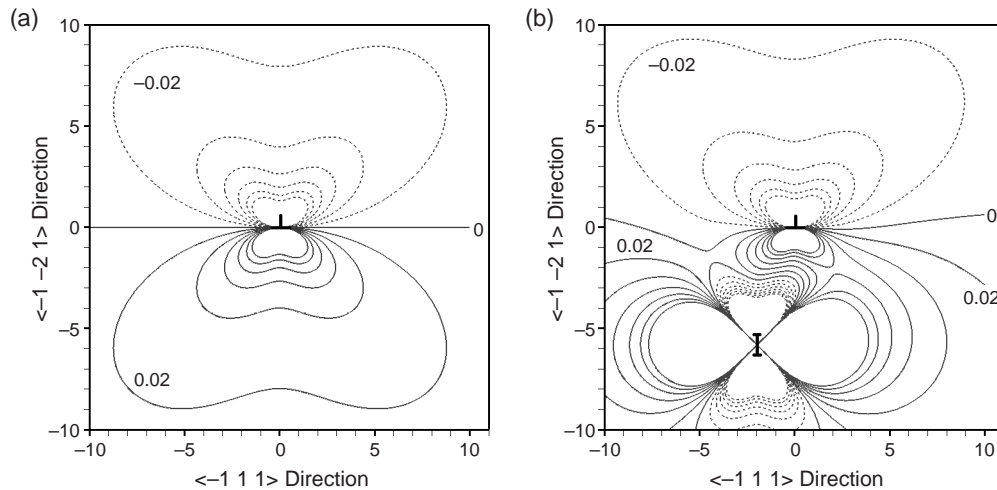
Figure 30. (a) Local isoenergy contours for the interaction energy of a SIA cluster of Burgers vector $a/2\langle\bar{1}\,1\,1\rangle$ with an edge dislocation on the $\langle\bar{1}\,\bar{2}\,1\rangle$-plane in bcc iron; (b) local isoenergy contours of the interaction energy of an interstitial defect clusters of Burgers vector $a/2\langle\bar{1}\,1\,1\rangle$ with a preexisting same type cluster and an edge dislocation on the $\langle\bar{1}\,\bar{2}\,1\rangle$-plane. Contours are plotted at 0.02 [in $\mu\delta A/(1-\nu)$, where μ is the shear modulus and δA is the surface area of the SIA cluster] increment.

When the attractive stress field of the dislocation is fully compensated for by the existing clusters, the SIA content in the primary trapping region achieves saturation and the decoration process stops. Although dislocation decoration saturates at a low dose, the primary region of cluster trapping shifts the stress field of the dislocation, and cluster trapping occurs only ahead of the existing dislocation/loop structure, where the interaction remains attractive [277]. For increasing dose, cluster trapping continues away from the dislocation and results in dislocation wall formation. As seen in Figure 25d, our simulations have already shown the extension of cluster trapping and the formation of dislocation wall.

In addition to dislocation decoration, another major striking feature of microstructure evolution is the formation of dislocation loop rafts. Figure 31 shows a configuration of SIA cluster rafts formed at a dose level of 1.8×10^{-3} dpa. The Burgers vectors of the clusters making up the raft are all parallel to on other, which is in agreement with experimental observation [277]. When an interstitial cluster approaches another one, they are subject to the influence of the strain field of each other. If the interaction between them is attractive and strong enough to overcome the energy barrier for directional change, clusters adjust
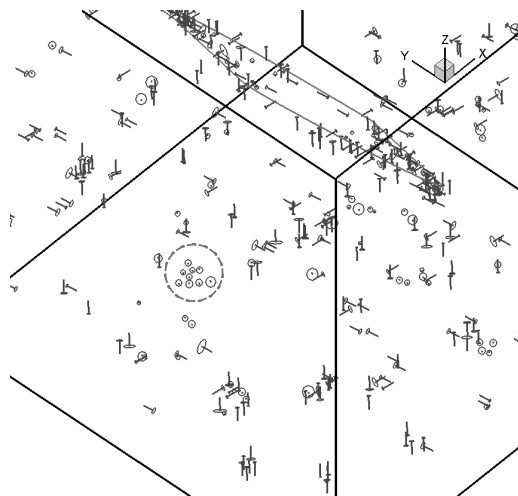
Figure 31. A close-up view of the configuration of a raft of interstitial clusters formed at a dose level of 1.8×10^{-3} dpa. The raft is enclosed in a dotted circle.

their relative positions and orientations. This scenario is similar to the pinning of clusters, which has been demonstrated in the previous section.

To shed light on the nature of cluster-cluster self-trapping, we consider the forces between two identical clusters. In Fig. 32a prismatic dislocation loop is fixed at the origin, and another identical one is moved along its slip direction. The glide force on the moving loop is plotted as a function of its relative position. It is shown that 5 equilibrium positions (zero force) exist between the two parallel clusters. However, only three of them are stable, at a relative angle of $\pm 30.5°$ or $\pm 90°$. When multiple clusters interact, this simple picture is somewhat disturbed. Nevertheless, extended stable cluster complexes form by this self-trapping mechanism. Figure 33 shows the force field along the slip direction of an existing raft obtained in our simulations. Two additional clusters that will join the raft in the following time step are also shown in dotted lines. It can be seen that raft formation is "autocatalytic," as a raft nucleus is stable, but keeps expanding through the association of other clusters on its periphery. As the number of clusters within a raft increases, the mobility of the raft as a whole decreases. The decrease in the mobility of individual clusters can be attributed to mutual elastic interactions between clusters that are members of a raft.

5.3.3.2. Conditions for Decoration and Raft Formation   Trinkaus et al. [277] have shown that a grown-in dislocation would have a large drainage area for accumulating one-dimensionally migrating glissile loops in its neighborhood. Our simulations also demonstrate that even at a fairly low dose of 1.3×10^{-3} dpa, a clear dislocation decoration is observed. The energy barrier for directional change is a critical parameter in controlling when, how, and to what extent dislocation decoration and raft formation occur. The maximum range for the elastic interaction that is strong enough to overcome the barrier and thereby leads to a Burgers vector change is strongly dependent on this parameter. In other words, the interaction between defects and the microstructures contributes to dislocation decoration and the formation of rafts in terms of changing the diffusivity and the characteristics of mixed 1D/3D migration. Brimhall and Mastel [283] proposed that loops move through the lattice
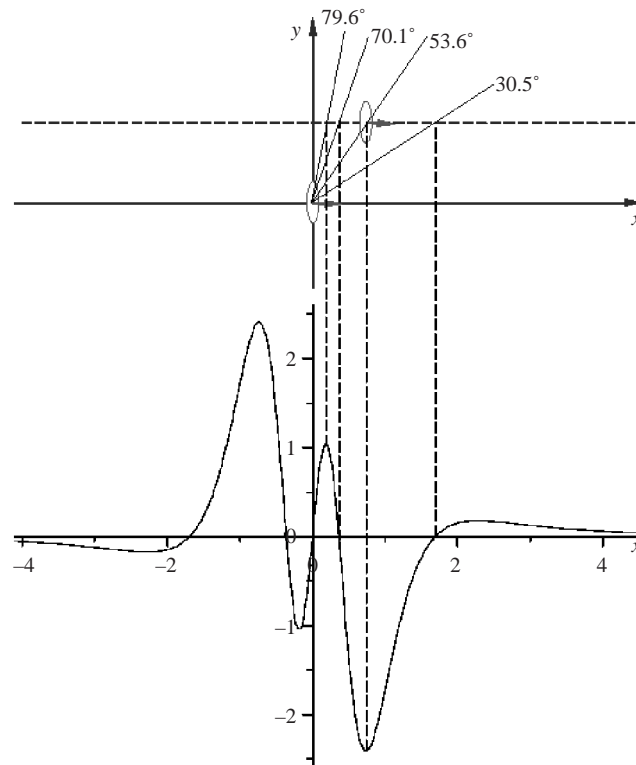
Figure 32. The glide force between two prismatic dislocation loops with parallel Burgers vectors as a function of their relative positions. The force is scaled by $\mu b_1 b_2 A_1 A_2 / 4\pi(1 - \nu)$, where b_i and A_i $(i = 1, 2)$ are the Burgers vectors and surface areas of the two loops, respectively.
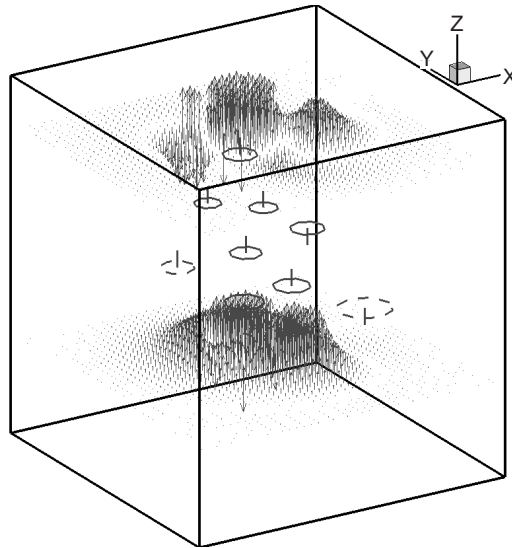
Figure 33. Force field distribution along the glide direction of an existing raft of SIA clusters (in solid lines). Two new SIA clusters (in dashed line) that will join the raft are also shown.

by a combination of prismatic glide and self-climb to form rafts. Our present simulations, however, suggest that raft formation could be achieved just by prismatic glide and rotation of glissile SIA clusters. A necessary condition for pronounced formation of rafts is that the group of clusters within a raft is large enough to trap a single glissile cluster in the strain field formed by the group and prevent it from further Burgers vector rotation. Our simulations indicate that small rafts containing two or three clusters are still mobile; more specifically, these small patches still perform 1D migration, although at reduced mobility. With the size of a patch increasing, the overall mobility decreases, and a raft consisting of more than five clusters is literally immobile. Due to thermal activation or interaction with other defects, a SIA cluster trapped in the outer region of a raft may break away and detrap from the raft.

The importance of glissile SIA clusters produced in displacement cascades has been demonstrated to play a decisive role in the irradiation-induced microstructural evolution. The 1D motion of glissile SIA clusters and the interaction between defects and the dislocation microstructure were shown to be the main cause for the appearance and development of decorations and rafts. At a rather low dose around 1.0×10^{-3} dpa, a large portion of the initially glissile clusters are shown to be trapped around the slip dislocation loop (the majority of them are distributed near the edge component) and become nearly virtually immobile. The high concentration of SIA loops around slip dislocations results in an extremely inhomogeneous spatial distribution. Our simulations show a clear picture of how SIA clusters are attracted to dislocations to decorate and lock them in place. It is suggested that raft formation could be achieved just by prismatic glide of glissile interstitial clusters and rotation of their Burgers vectors under the influence of internal strain fields (e.g., generated by dislocations).

5.4. DD Applications

5.4.1. Microstructure Evolution

The solution of the set of ordinary differential Eqs. (215) describes the motion of an ensemble of dislocation loops as an evolutionary dynamical system. However, additional *protocols* or algorithms are used to treat (1) strong dislocation interactions (e.g., junctions or tight dipoles), (2) dislocation generation and annihilation, (3) adaptive meshing as dictated by large curvature variations [192].

The shape of individual loops within an ensemble is evolved using equations of motion for generalized coordinates representing the position, tangent, and normal vectors of nodes on each loop. Figure 34 shows the results of such computations for simulation of plastic
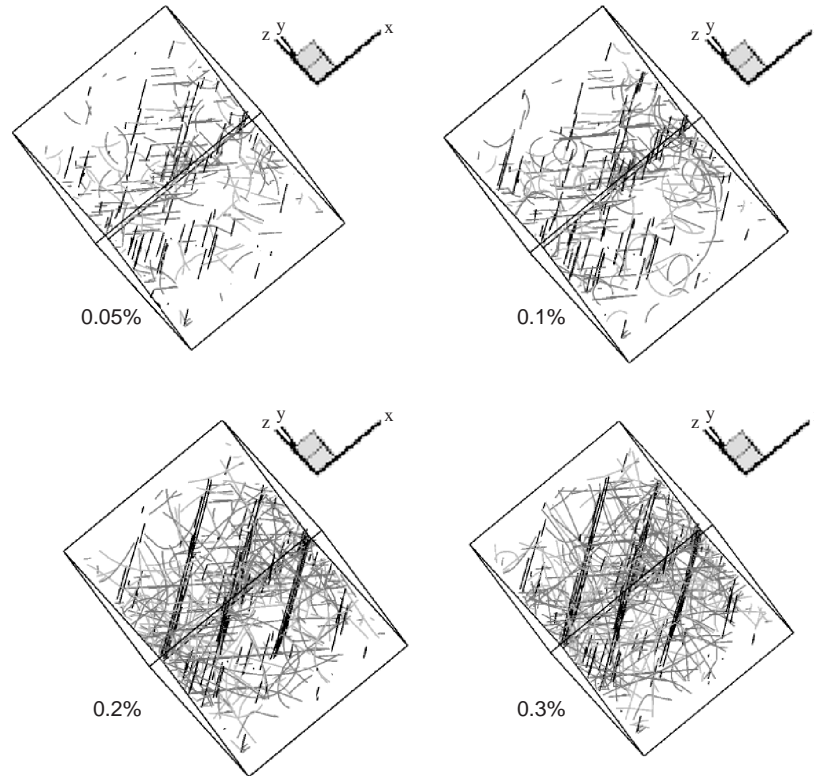
Figure 34. Results of computer simulations for dislocation microstructure deformation in copper deformed to increasing levels of strain (shown next to each microstructure). After [284].

deformation in single crystal copper at a constant strain rate of 100 second^{-1}. The initial dislocation density of $\rho = 2 \times 10^{13} \ m^{-2}$ has been divided into 300 complete loops. Each loop contains a random number of initially straight glide and superjog segments. When a generated or expanding loop intersects the simulation volume of 2.2-μm side length, the segments that lie outside the simulation boundary are periodically mapped inside the simulation volume to preserve translational strain invariance, without loss of dislocation lines. The number of nodes on each loop starts at 5, and is then increased adaptively proportional to the loop length, with a maximum number of 20 nodes per loop. The total number of Degrees of Freedom (DOF) starts at 6000, and is increased to 24,000 by the end of the calculation. However, the number of *interacting* DOF is determined by a nearest neighbor criterion, within a distance of 400 a (where a is the lattice constant), and is based on a binary tree search. The dislocation microstructure is shown in Fig. 34 at different total strain [284]. It is observed that fine slip lines that nucleate at low strains evolve into more pronounced slip bundles at higher strains. The slip bundles are well-separated in space forming a regular pattern with a wavelength of approximately one micrometer. Conjugate slip is also observed, leading to the formation of dislocation junction bundles and what appears to a stabilization of a cellular structure.

5.4.2. Plasticity Mechanisms with Anisotropic DD

Dislocations will move under forces and are balanced by viscous dissipation. The variational form of the governing equation of motion of a dislocation loop is given by Eq. (211) [190, 192, 285]. In this section, we incorporate the current methodology of calculating dislocation interactions and self-forces with full anisotropic elasticity theory into our PDD computational method [190, 192, 285]. We will focus first on the results of elementary dislocation mechanisms in anisotropic cubic crystals, where the effects of anisotropy are conveniently evaluated in terms of A. The results for three typical dislocation mechanisms, essential is DD simulations, are evaluated next. These are Frank-Read (F-R) source expansion, dislocation dipoles and dislocation junctions.

Figure 35 displays the evolution of an F-R source from an initial straight segment in an FCC crystal with different anisotropic ratios A. The segment of an initial length $1000a$ is located on the (111)-glide plane, and is pinned at its two ends. The Burgers vector is $\mathbf{b} = \frac{1}{2}[\bar{1}01]$, and the segment is along the $[\bar{1}10]$ direction. The segment is then subjected to a sudden uniaxial stress $\sigma_{11}/\mu = 0.2\%$ (with $\mu = (C_{11} - C_{12})/2$, and resolved shear stress $\tau/\mu = 0.08\%$) along the [100]-direction. Stresses are measured in units of $\mu = (C_{11} - C_{12})/2$, and distances in units of the lattice constant a. Other parameters are: $C_{11}/C_{12}/\mu = 5 : 3 : 1$, and the dislocation mobility is taken as $M = 10^4$ Pa^{-1} s^{-1}. These units and parameters will be used throughout all following simulations, unless stated otherwise. The effects of elastic anisotropy on the expansion of a typical F-R source are shown in Fig. 35. As the anisotropy ratio increases, greater resistance to shear deformation is observed, as if the "effective" self-force becomes larger. Full calculation of the self-force is computationally intensive, because of the need to perform numerical line integrals over the entire loop. Hence, local approximations become desirable. The figure shows that the F-R source expansion rate is sensitive to the method of self-force approximation, and that full calculations are
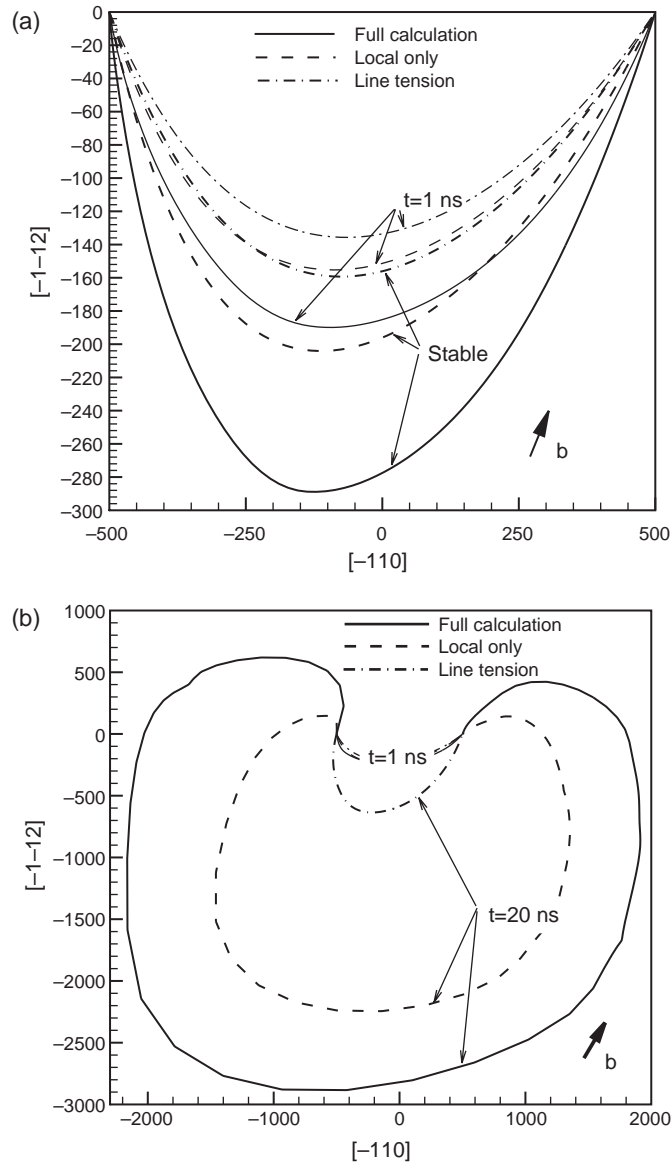
Figure 35. Evolution of an F-R source under applied stress $\sigma_{11}/\mu = 0.2\%$ [resolved shear stress $\tau/\mu = 0.08\%$, with $\tau = 0.5(C_{11} - C_{12})$], for anisotropy ratio (a) $A = 2$ and (b) $A = 0.5$.

required if one needs higher accuracy. The spatial position of the F-R source is shown for three cases: (1) full calculation of the self-force as outlined above, (2) calculations with the line tension approximation for the self force, and (3) calculations with only the local term in the self force. The effects of the method of self-force calculation is especially evident when the F-R source expansion is unstable (see Fig. 35b), because the instability threshold stress is sensitive to the magnitude of the self-force.

Next, we consider the dynamic process of dislocation dipole formation in FCC crystals. Figure 36a shows the configurations [2D projected on the (111)-plane] of two pinned dislocation segments, lying on parallel (111)-planes. The two dislocation segments are initially straight, parallel, and along $[\bar{1}10]$, but of opposite line directions, have the same Burgers vector $\mathbf{b} = \frac{1}{2}[\bar{1}01]$, and are pinned at both ends. Their glide planes are separated by h. In this figure, $h = 25\sqrt{3}a$, $L : d : h = 800 : 300 : 25\sqrt{3}$, with L and d being the length of the initial dislocation segments and the horizontal distance between them, respectively. Without the application of any external loading, the two lines attract one another, and form an equilibrium state of a finite-size dipole. It is interesting to note that while the dynamic shape of the segments during the dipole formation is dependent on the anisotropy ratio A, the final configuration appears to be insensitive to A. Under external loading, the dipole may be unzipped, if applied forces overcome binding forces between dipole arms. The forces (resolved shear stresses τ, divided by $\mu = (C_{11} - C_{12})/2$) to break up the dipoles are shown
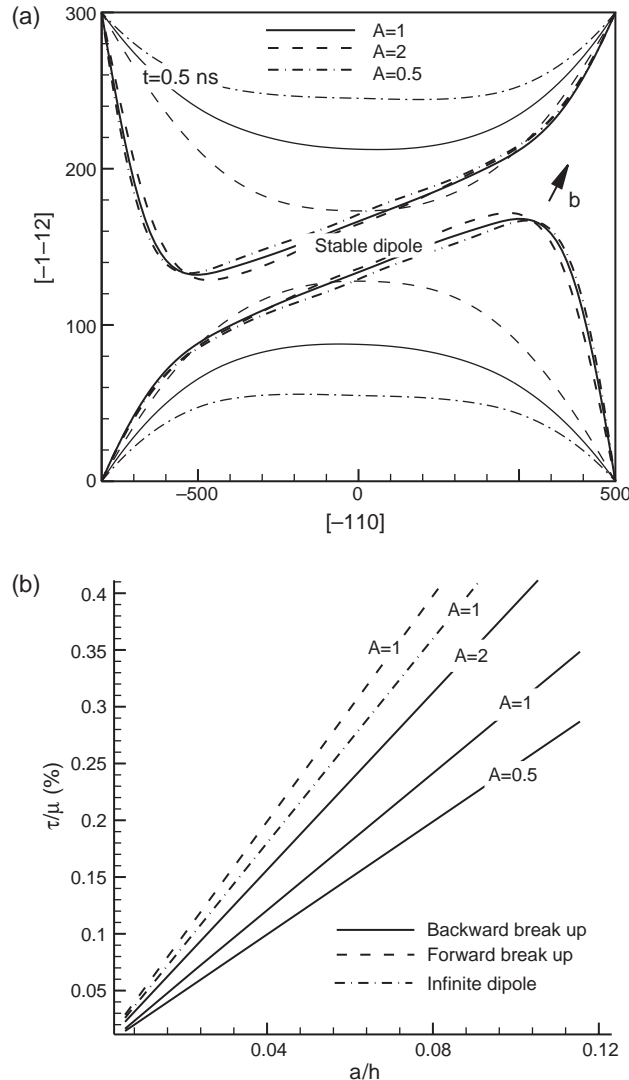
Figure 36. Evolution of dislocation dipoles without applied loading (a) and dipole break-up shear stress (b).

in Fig. 36b. It can be seen that the break up stress is inversely proportional to the separation distance h, consistent with the results of infinite-size dipoles. It is easier to break up dipoles in crystals with smaller A-ratios (e.g., some BCC crystals). It is also noted that two ways to break up dipoles are possible: in backward direction (where the self-force assists the breakup), or forward direction (where the self-force opposes the breakup). For a finite length dipole, the backward break up is obviously easier than the forward one, due to the effects of self forces induced by the two curved dipole arms, as can be seen in Fig. 36b.

When two dislocations approach each other, their interaction can be very strong, leading to significant reconfiguration. They may attract each other to form a stable common part (junction), or repel one another. In Fig. 37, we show the configurations of attractive junctions in FCC crystals of different anisotropy ratios. Two initially straight dislocation segments, with Burgers vectors and slip planes given by $\frac{1}{2}[01\bar{1}](111)$ and $\frac{1}{2}[101](11\bar{1})$, respectively, are pinned at their ends. They are allowed to move and approach each other, until they lock in an equilibrium state. The two dislocations attract each other to form a common junction along the intersection direction of the two glide planes $[\bar{1}10]$. Each of the initial dislocations has a length of $500\sqrt{5}$ and makes an angle $\theta = 26.6°$ with $[\bar{1}10]$. Without the external loading, the junction configuration in crystals with different anisotropy ratio A are quite similar. The strong binding forces appear to overcome differences in their self-forces, and thus the configuration is not sensitive to A. With an increase in external loading, the junction length decreases, until the junction is unzipped at a critical stress. The junction strength is found to depend on the anisotropy ratio. From the figure, it can be seen that under external loading, the junction length decreases faster for smaller A. Dislocation junctions of the type studied here are thus weaker (or stronger) in anisotropic crystals of lower (or higher) values of A.

5.4.3. Approximations with Effective Moduli

Although the PDD has been extended in this work to crystals of arbitrary elastic anisotropy, in practice however, the computational requirements can be taxing, especially in large-scale computer simulations. For that purpose, it may be advantageous to perform computer simulations with isotropic PDD, provided that the results of such simulations would closely match the more computationally intensive anisotropic PDD. In this section, we investigate three different averaging methods that have been proposed to extract "equivalent" isotropic
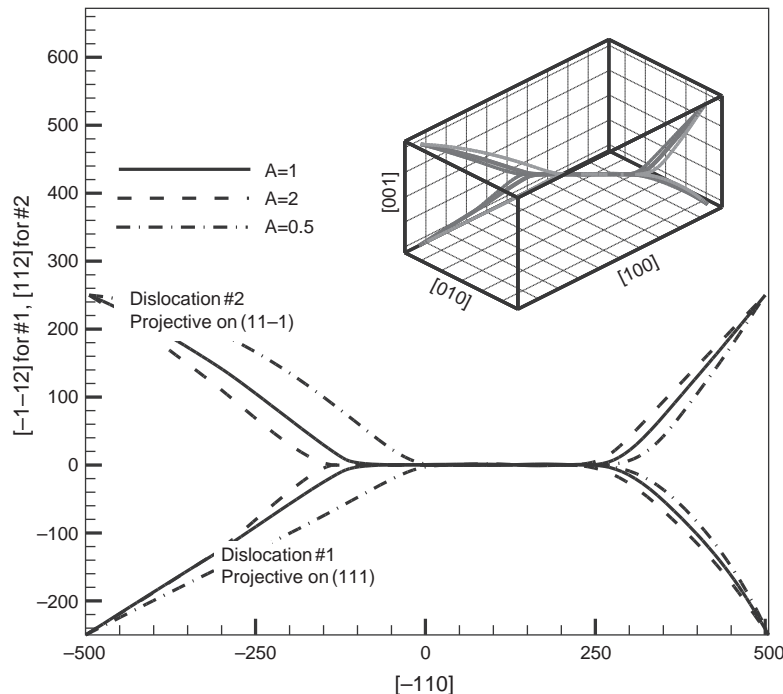
Figure 37. Evolution of dislocation junctions under applied loading $\sigma_{11}/\mu = 0.24\%$ ($\tau/\mu = 0.056\%$).

elastic constants from the full anisotropic values. Two such methods, the Voigt (V) and Reuss (R) averaging procedures, are common in general elastic deformation problems, while the third one, the Scattergood-Bacon (S-B) procedure, has been specially used in the context of determining equilibrium shear loop configurations [286]. We will examine here the extent of agreement between isotropic PDD with the anisotropic counterpart APDD, when these three approximations are used.

In the Voigt scheme, the averaging is performed over the elastic constant tensor C_{ijkl}, while in the Reuss scheme, it is done over elastic compliances S_{ijkl}. Results of such averaging and relevant parameters for some anisotropic crystals are listed in [225]. All calculations reported in this section are for the case of single crystal copper ($A = 3.21$). The calculated elastic constants are given in Table 4 below.

First, we give a simple example, to determine how well the static stress field of dislocations in anisotropic crystals can be approximated by effective isotropic elasticity. Calculations of the stress field along the symmetry axes of a circular shear dislocation loop show that the shear stress component σ_{zx} can be well approximated (especially by the S-B scheme) along the coordinate axes. However, as a result of anisotropy, a distortion stress component σ_{xy} exists even along the geometric symmetric axes, and which cannot be produced by any isotropic approximation. Thus, the full components of the stress field tensor induced by dislocations in anisotropic crystals cannot be replaced by isotropic approximations. However, the influence of such difference on interaction and self-forces, and on microstructure evolution need to be investigated.

To study the effects of averaging the anisotropic elastic moduli in PDD simulations, we will compare here the results of full anisotropic calculations with their corresponding isotropic approximations. This will be accomplished by focusing on three typical dislocation mechanisms: F-R source expansion, dipole dynamics, and junction formation.

Figure 38 shows the results of DD simulations of an F-R source on the $\frac{1}{2}[\bar{1}01](111)$ slip system. For stable F-R configurations below a critical bow out stress, or at short evolution times, the isotropic approximations of Reuss and S-B are quite suitable. For stress levels greater than the critical bow out stress, and at long time intervals, great differences exist between the approximation and the full anisotropic calculations. For the special case of the F-R source, it is found that the S-B approximation is the most suitable, followed by the Reuss averaging schemes. Figure 39 shows the simulation results for the process of dipole formation. The results indicate that none of the isotropic approximations produce similar dipole configurations to the anisotropic case. While the middle section of the finite size dipole is perfectly straight in the isotropic case, the lateral separation between the dipole arms is not constant in the anisotropic case. This is a consequence of the stronger dependence of the self-force on the angle between the Burgers and tangent vectors in the anisotropic case.

Generally, all these typical dislocation mechanisms can be captured and simulated qualitatively by isotropic approximations. The errors are on the order about 20% or less, and the Scattergood-Bacon or Reuss approximations to the elastic moduli are preferable. However, for more accurate studies of dislocation mechanisms (e.g., in thin films), or for studies of critical stress levels to bow out a segment or unzip dipoles/junctions, care must be exercised in using isotropic approximations.

5.4.4. Strain Hardening in Cu

In contrast with our PDD computer code using isotropic elastic theory, APDD simulations are computationally massive. The main reason is that the evaluation of the elastic field and self-forces requires additional numerical integrations, with a corresponding large number of

Table 4. Elastic constants of single crystal Cu ($C_{11} = 168.4$, $C_{12} = 121.4$, and $C_{44} = 75.4$ GPa).

Averaging method	μ (GPa)	ν
Voigt (V)	54.6	0.324
Reuss (R)	40.0	0.369
Scattergood & Bacon (S-B)	42.1	0.431
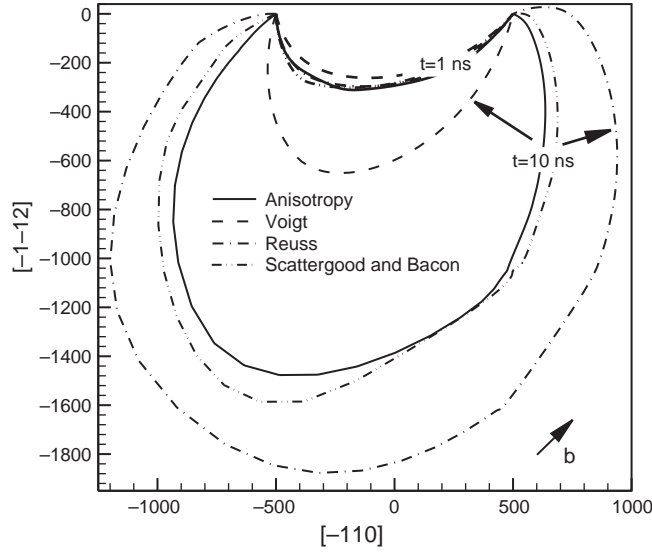
Figure 38. Evolution of F-R source in anisotropic elasticity, compared with isotropic approximations under stress $\sigma_{11} = 120$ MPa.

calculations of the derivatives of Green's functions. To reduce the computational cost, a storage and look-up table technique can be used. We calculate the functions $G_{ij,k}(\mathbf{r})/r^2$, which only depend on the unit direction vector $\mathbf{r}/r$ at tabulated data points (usually represented in spherical coordinates). We then store the results of these calculations in a look-up table. Values of these functions at desired directions are obtained by interpolation. This technique results in higher demands on memory allocations, but is generally advantageous for massive DD simulation. When computing and storing these functions, we also take advantage of the symmetry properties: $G_{ij,k}(\mathbf{r}) = G_{ji,k}(\mathbf{r}) = -G_{ij,k}(-\mathbf{r})$. This symmetry reduces the number of Green's derivative components from 27 to 18. The functions $G_{ij,k}(\mathbf{r})/r^2$ were first evaluated at points on a half unit sphere, represented by the two angles $0 \leq \theta \leq \pi/2$
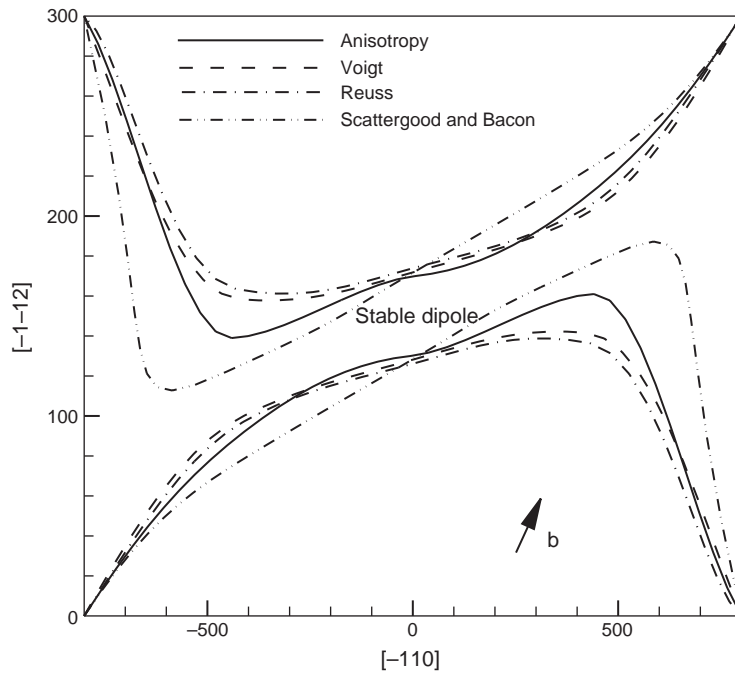
Figure 39. Dislocation dipole in anisotropic elasticity, compared with isotropic approximations, under the stress $\sigma_{11} = 45$ MPa.

and $0 \leq \phi \leq 2\pi$. Values at intervals $\Delta\theta = \Delta\phi = h$ have been calculated and stored, and a linear interpolation scheme was then used to determine other function values. We chose $h = \pi/500$, resulting in storage requirements for 4.5 million function evaluations.

To study the effects of elastic anisotropy on strain hardening and the corresponding dislocation microstructure evolution, the deformation of a Cu cube of side 0.75 μm and containing an initial dislocation density of 5×10^{13} m^{-2} is simulated. An initial random distribution of 40 dislocation loops was generated on different slip planes. Periodic boundary conditions were applied to loops that expand beyond the simulation volume boundary such that segments which leave one of the surfaces are mapped back periodically on corresponding entry points on opposite surfaces. In these calculations, we simulate a uniaxial tensile test of the cube at a constant strain rate 10^3 s^{-1}, with the load applied along [100] direction.

The corresponding simulated stress-strain curve is shown in Fig. 40, where calculations with full elastic anisotropy are compared with the Voight and S-B approximations. It is clear that both approximations are not capable of reproducing the stress-strain curve for anisotropic single crystals. A major difference is attributed to the elastic response at very low strains as a result of differences in the "effective Young's modulus." If this difference is accounted for, one can see that the strain hardening behavior that results from dislocation microstructure is reproduced somewhat better by the S-B approximation. These observations are derived from simulations to low strain values, while simulations at high strain or different microstructure may reveal other features.

5.4.5. Nanolayered Materials

A variational form of the governing equation of motion for a dislocation loop Γ has been developed for over-damped dislocation dynamics, where the work exerted on dislocation loop expansion is balanced by viscous dissipation [192], that is, $\int_\Gamma (F_k^t - B_{\alpha k} V_\alpha)\delta r_k |d\mathbf{s}| = 0$. Here, F_k^t is the total Peach-Koehler force induced by applied external forces, internal stress fields (such as dislocation interactions, interface image forces, and the self-force), $B_{\alpha k}$ is the resistance (inverse mobility) matrix, V_α is the velocity, r_k is the displacement of the dislocation line, and $d\mathbf{s}$ the dislocation line vector. Because the present formulation results in a line integral form of the force vector distribution, it can be readily incorporated into the PDD framework [192]. In this section, we present computer simulation results for dislocation motion in nano-layered materials using the PDD methodology.

It has been experimentally established that the hardness (or strength) of multilayer thin films is much higher than corresponding bulk materials. It is also shown by numerous
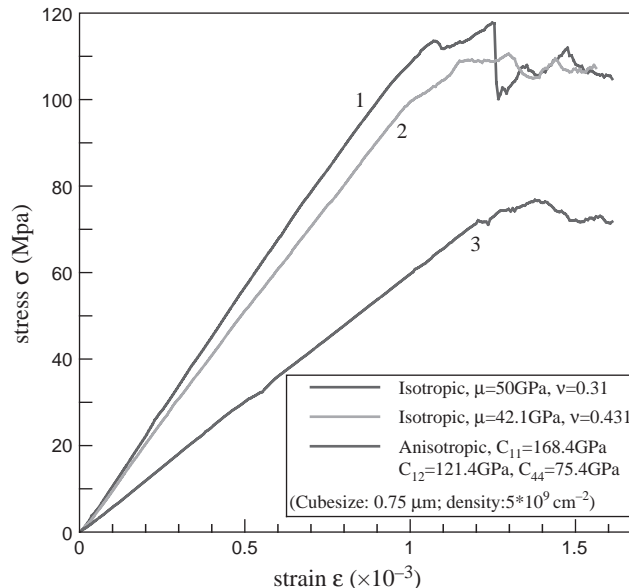
Figure 40. Stress-strain curves for single copper crystals.

experiments that the strength and hardness of the film increase as the thickness of constituent layers decreases [287–289]. Several underlying mechanisms have been proposed in recent years, although relying on approximate treatments of dislocation fields in such systems. The objective here is to apply the present rigorous elasticity solutions for 3D dislocation loops in anisotropic, multi-layer thin films to develop an understanding of plasticity and strength at the nano- to the microscale.

Experimental results and isotropic elasticity estimates show that the dominant mechanism that controls the strength and hardness of multi-layer thin films is the influence of the dislocation image force associated with a mismatch in elastic properties between adjacent film layers [289]. For layered materials with a large mismatch in elastic properties, a significant hardness enhancement was observed. On the other hand, for layered materials with small differences in their elastic properties, no measurable hardness enhancement was detected [287, 289]. Experiments on an Fe/Pt layered system [290, 291] indicated that when the bilayer thickness ranges from few to tens of nano-meters, the hardness of this bilayer metal system exhibits a plateau. Over this bilayer period range, the interface structure, misfit dislocation density and coherency strains all change rapidly, so they are not likely to be the dominant mechanism. Hence, the mismatch in elastic moduli was concluded to be the most likely dominant factor determining hardness enhancements in these layered materials [290, 291].

Two models are often used to explain the observed behavior of hardness (or flow stress) in thin films. In the threading dislocation model [292, 293], the flow stress is determined by the energy balance between the threading glide dislocation segment and the misfit dislocation left behind at the interface. This model results in a flow stress that scales approximately with the inverse of the film/layer thickness. For a thin film/layer of thickness h, subjected to a uniform applied biaxial stress σ_a, the critical stress (σ_c^{th}) for threading dislocation motion is given by [292]

$$\sigma_c^{th} \approx \frac{\mu b}{4\pi(1-\nu)h}[(4-\nu)\ln(h/r_0) - 1] \tag{280}$$

for an isotropic material with a shear modulus μ, Poisson's ration ν, and a dislocation core cutoff radius $r_0 \approx b$. In this model, interfaces are introduced as impenetrable planes for dislocations.

The second model is an extension of the well-known Hall-Petch effect. Here, dislocations are assumed to form a pile-up at a boundary until a critical stress is reached. This results in a flow stress which is inversely proportional to the square root of the layer thickness or grain size. Both models qualitatively explain the increase in the flow stress with decreasing film/layer thickness, but not the behavior as the layer thickness decreases below tens of nano-meters.

In the current work, we focus on simulation of dislocation motion in relatively thin layers, when the individual layer thickness is in the range of few nanometers to hundreds of nano-meters. This is typically much smaller than the characteristic length scale of grains occupied by dislocation networks in bulk materials. Therefore, the number of dislocations needed in order to study thin layer plasticity is small. In many cases, plasticity and strength can be described through the behavior of a single dislocation loop.

Consider a Cu thin layer (thickness h), sandwiched between two semi-infinite harder Ni substrates. The dislocation is originally located within the thin layer. Cu and Ni are both fcc crystals with [001] out-of-plane orientations and $\langle 110 \rangle \{111\}$ slip systems, and anisotropic elastic constants [225]. In Cu, $b = 0.361$ nm, and the dislocation mobility is taken to be isotropic ($M = 10^4$ Pa^{-1} s^{-1}). The system is subjected to a uniform applied biaxial stress σ_a. We will ignore here the stress due to lattice mismatch. We only consider the image force effect due to the modulus difference at the Cu-Ni interface. The value of image force increases as the dislocation segment approaches the interface, and is singular exactly at the interface. This is a consequence of the assumptions of linear elasticity, which has been successfully used in dislocation dynamics simulations including similar singular behavior of the dislocation self-force, energy and junction formation. If a cutoff radius is introduced for the dislocation, the results of infinitesimal linear elasticity for self-force, energy, and junction formation are in good agreement with more detailed atomistic simulations [253]. We assume also here that

dislocations do not dissociate into partials, and take the cutoff radius to be $r_0 \approx b$ [292, 293]. Detailed atomistic simulations are required to ascertain the value of the cutoff distance. In the following simulations, we assume that there is one Frank-Read (F-R) source inside one of the layers, and that the source dislocation is initially straight and pinned from both ends.

5.4.5.1. Confined Layer Slip Figure 41 shows the propagation mode of a source dislocation in a Cu layer of thickness 144 nm at different loading levels. We choose the length L of the original dislocation to be longer than the layer thickness, h, that is, L = 4h. Under a small applied stress below a critical value [approximately estimated by Freund's formula, Eq. (280)], the dislocation will bow out in the Cu layer towards the interface. As a result of the image force exerted by the harder Ni layer, the dislocation is repelled away from the interface and reaches an equilibrium configuration. If the applied stress is larger than the critical value, the dislocation first bows out towards the interface then it is blocked by the image force and is confined to propagate within the layer. The critical stress for the onset of confined layer slip is first estimated according to Eq. (280) with equivalent isotropic values of μ and ν. This value is then refined by increasing (or decreasing) the applied stress until the dislocation cannot achieve its equilibrium configuration any more.

The influence of the dislocation source size is also considered. Below the critical stress for threading dislocation motion σ_c^{th}, dislocations cannot propagate in the layer. When the initial source size is approximately longer than the layer thickness, the dislocation bows out and reaches an equilibrium configuration. If the initial source size is smaller than the layer thickness, slip propagation is controlled by the Orowan mechanism, and the critical stress for bowing out can be estimated as [294]: $\sigma_c^O \approx \mu b / 2\pi L \sqrt{6} \ln(L/r_0)$.

In comparing the critical stresses for a threading dislocation motion within a layer, σ_c^{th}, with that for the activation of an F-R source by the Orowan mechanism, σ_c^O, the two values are close when the layer thickness, h, is on the order of the initial F-R source length, L. In any thin layer, many F-R sources may exist with different sizes, locations, and orientations. If the applied stress is smaller than the critical stress for threading dislocation motion, $\sigma < \sigma_c^{th}$, some dislocations will expend toward the interface, but none would be able to propagate within the layer. Once the applied stress is removed, F-R source dislocations will re-tract to their original length. This type of dislocation motion does not lead to permanent deformation of the thin film. We term this regime as *quasi-elastic*. When the applied stress reaches the critical value σ_c^{th}, longer dislocations with L > h will expand, but will still be confined within the layer. This regime of behavior is the so-called confined layer slip (CLS) [295]. Finally, if the applied stress is increased further, $\sigma > \sigma_c^O > \sigma_c^{th}$, shorter dislocations L < h are gradually activated, first bowing out from stable shapes, then reach the interface, and finally propagate within the layer. Thus, dislocations emitted from longer F-R sources with L > h
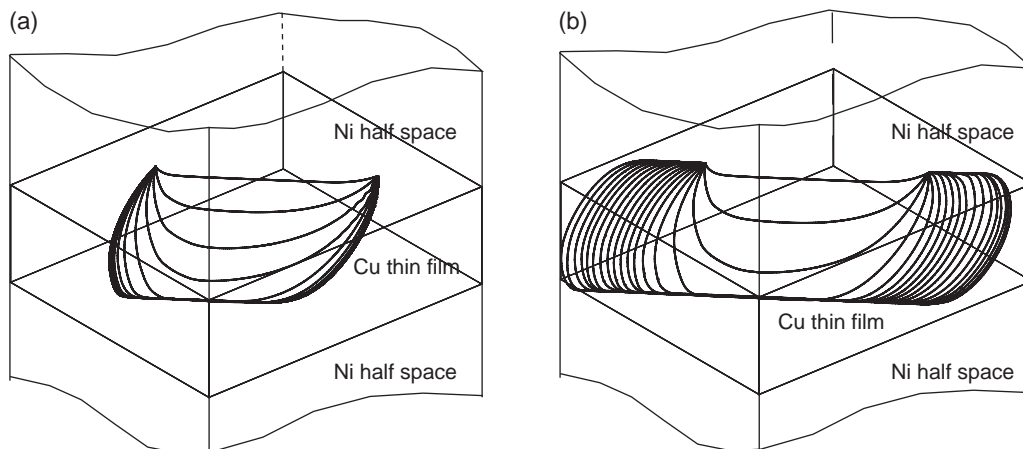
Figure 41. Dislocation motion in a thin layer with h = 144 nm under different applied biaxial stress levels (a) $\sigma_a = 210$ MPa < $\sigma_c^{th} = 250$ MPa, and (b) $\sigma_a = 280$ MPa > $\sigma_c^{th} = 250$ MPa. Each line corresponds to a time increment of 0.1 ns.

are controlled by the threading dislocation mechanism, while shorter ones by the Orowan mechanism.

5.4.5.2. *Loss of Slip Confinement*

As individual layers become very thin (i.e., in the tens of nanometers), only single dislocations can propagate and expand upon the application of an externally applied stress. However, because the layer thickness is very small, the curvature of the dislocation loop in segments subtended between layers would be extremely high, and thus self-forces in these regions are very substantial. The externally applied stress would have to overcome such large self-forces if these curved segments are to expand. The applied P-K force on those segments that are parallel to the interface does not have to overcome self-forces because the curvature of these segments is small. Rather, the image force from neighboring and other interfaces would have to be overcome by the applied P-K force. Because we regularized the solution by selecting a cutoff radius of one Burgers vector on either side of the interface, the dislocation will be repelled with a maximum image force on one side of the interface, and then attracted with a different maximum force once it crosses the interface. If the applied stress is high enough that the maximum P-K force on the straight dislocation segments close to the interface overcomes both repulsive and attractive forces, the dislocation will cross from one layer to the neighboring one, and CLS is finally lost. This mode of deformation is shown in Fig. 42, where successive dislocation positions at 10 ns time intervals are shown for an F-R source dislocation, initially with a straight segment pinned at both ends, and is subjected to a suddenly applied bi-axial stress of magnitude 1.2 GPa. The dislocation, which lies on the (111)-slip plane, has an initial length of 43.2 nm, and its Burgers vector is $\frac{a}{2}\langle\bar{1}01\rangle$. After 15 ps, the leading edge of the bowed out dislocation reaches the interface. Because the applied P-K force is larger than both the attractive and repulsive components of the image force, the dislocation loses confinement within the copper layer and expands into the neighboring nickel layer.

Figure 43 shows results of our calculations for the maximum strength of a copper layer in a thin film of alternating Cu/Ni layers based on the activation of a single F-R source, as a function of the layer period. Experimental results for nanoindentation by Misra et al. [288] and Clemens et al. [289] are also shown. Because Freund's formula is often used to estimate the strength of thin films, film strength using Eq. (280) is also shown as a solid line on the same figure for comparison. For layers of thickness less than approximately 100 nm, a single F-R source will determine the overall strength of the layer as a competition between confinement in the layer by image forces generated by elastic modulus mismatch, and resistance to deformation by self-forces on the curved ends of the dislocation loop. If the modulus mismatch is not too great, dislocation loops will cross from layer to layer rather than be
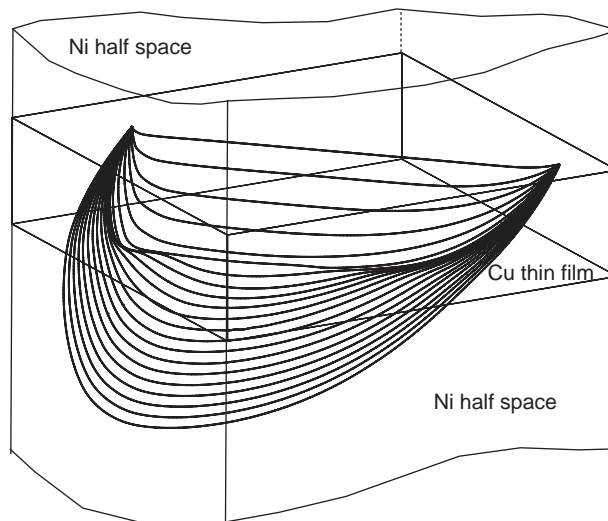
Figure 42. Dislocation motion in a thin layer with h = 10.8 nm under an applied stress $\sigma_a = 1.2$ GPa $> \sigma_c^{th} = 1$ GPa. Each line corresponds to a time increment of 2 ps.
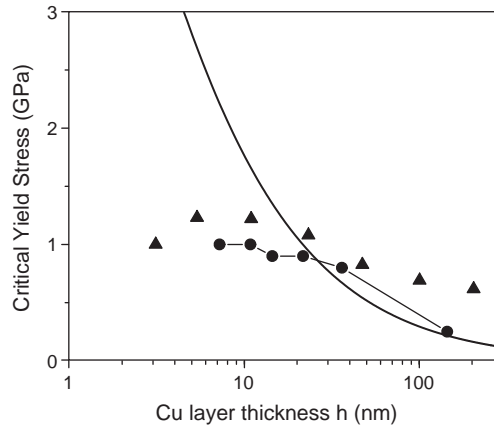
Figure 43. Yield strength of a Ni-Cu layered thin film as a function of the layer thickness. Solid line, Freund's formula; triangles, experimental results; and circles, current simulation results [288, 292].

confined within a layer. One would expect that the maximum strength is determined by the layer thickness and the ratio of elastic modulii as well. For thicker layers, F-R sources can operate many times leading to dislocation multiplication and the formation of a pile-up. In such case, the dominant deformation mode is the Hall-Petch mechanism.

Based on the current simulations, a strength-thickness map for Cu/Ni multilayer materials is shown in Fig. 44. Four regions representing different deformation mechanisms are shown, consistent with earlier investigations (see [296, 297]). These are:

1. **Region I**: The applied P-K force is smaller than both the Koehler barrier and the self-force. Dislocation loops deform to an equilibrium shape and regain their original shape upon removal of the applied stress. This is a *quasi-elastic* deformation mode.
2. **Region II**: The applied P-K force is larger than the Koehler barrier. Dislocation loops are no longer confined in this region, and *plastic instability* is manifest in loss of confinement.
3. **Region III**: The applied P-K force is less than the Koehler barrier but still greater than the maximum self-force anywhere on the loop. Loops are forced to propagate within one layer in this *confined layer slip* (CLS) mode of deformation.
4. **Region IV**: The layer thickness is so large that it can support several emitted dislocations from F-R sources within the layer, but the applied P-K force is such that the leading dislocation in the pile-up cannot overcome the Koehler barrier. This is the *classical Hall-Petch* mode of plastic deformation.
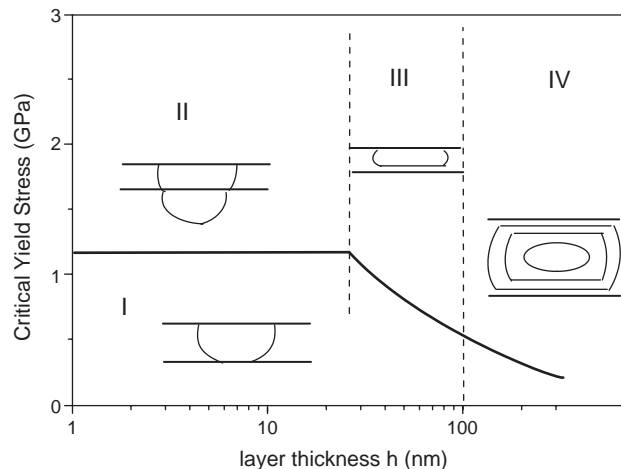
Figure 44. Plastic deformation mechanism and strength map for thin layered films.

The development of a line integral form for the elastic field of dislocations in anisotropic, multi-layered materials has enabled an extension of the PDD method to the simulations of plasticity and strength in these material systems. Earlier efforts in this area rely on surface integrals for the derivatives of Green's functions, which complicates numerical implementation in DD computer simulation programs. The following conclusions can be drawn from applications of the developed method to a number of material deformation problems at the nanoscale to the microscale:

1. The influence of free surfaces or interfaces on dislocation motion through image forces extends into the material to several hundred lattice constants. Thus, for computer simulations of large material volumes (e.g., tens of micrometers), image forces can be neglected until the dislocation is within a few hundred lattice constants. Numerical resolution of any method (including the finite element) must be sufficient close the surface.

2. In thin anisotropic films containing many layers of small thickness (i.e., in the tens to hundreds of nanometers), interaction between several interfaces contributes to the image force on dislocations. No simple geometric image construction can be found to yield accurate magnitude and direction of interface image forces.

3. To retain the original idea of the dislocation self-force in an infinite medium, the elastic field is separated into two components: one that yields the self-force in an infinite medium, while the second is due to the effect of interfaces (i.e., the image force).

4. In thin Al films on Cu substrates, it is shown that a small layer of aluminum oxide can reverse the surface image force from attractive to repulsive. Also, the interaction between the Al/Al_2O_3 interface and the Al/Cu interface can result in near zero image force on curved dislocation segments in the middle of the film. If the oxide film thickness is greater than the film thickness itself, its image force can be approximated by the semi-infinite half-space results.

5. Plastic deformation of very thin layers in the tens of nanometers in thickness range is controlled by a competition between the resistance of curved segments due to high self-forces, and the maximum force to transmit nearly straight segments across the interface (i.e., the Kohler barrier). If the layer is too thin, this results in high curvatures and resistance to CLS. Depending on the ratio of the elastic modulii of adjacent layers, dislocations may find an easier path to move into adjacent layers, and thus CLS is lost. On the other hand, if the ratio of elastic modulii between adjacent layers is sufficiently high and the layer thickness is sufficiently large, dislocations are forced to be confined within one layer.

6. Strength calculations from the current model show reasonable agreement with experimental nano-indentation data on Cu/Ni nanolayered materials. Strength saturation below layer thicknesses of $\sim$20 nm is a result of the near independence of the Koehler barrier strength on layer thickness. The present model is incapable of explaining the decrease in layer strength below $\sim$10 nm, as shown in the experimental data. This limitation may be attributed to atomistic dislocation core effects not included in the model.

7. Four general deformation mechanisms are identified for layered thin films: quasi-elastic, plastic instability, confined layer slip, and the Hall-Petch regime, consistent with recent literature [296, 297].

REFERENCES

1. J. L. Loubet, J. M. Georges, and G. F. Meille, in "Micro Indentation Techniques in Materials Science and Engineering" (P. J. Blau and B. R. Lawn, Eds.), p. 72. ASTM-STP 889, American Society for Testing and Materials, Philadelphia, PA, 1986.

2. T. W. Wu, C.-K. Lee, and R. H. Wang, Micro-impact technique and its application, *Mater. Res. Soc. Symp. Proc.*, Vol. 308, p. 133 (1993).

3. M. K. Small, B. J. Daniels, B. M. Clemens, and W. D. Nix, *J. Mater. Res.* 9, 25 (1994).

4. S. P. Baker, in "The Analysis of Depth-sensing Indentation Data" (P. J. Blau and B. R. Lawn, Eds.), *Mater. Res. Soc. Symp. Proc.*, Vol. 308, p. 209. Materials Research Society, Philadelphia, PA, 1993.

5. F. James, *Rep. Prog. Phys.* 43, 1145 (1980).

6. A. Segmueller and M. Murakami, Treatise on Materials Science and Engineering, Vol. 27, p. 143. Academic Press, New York, 1988.

7. U. Erb, G. Palumbo, R. Zugic, and K. T. Aust, "Structure-property Relationships of Nano-Crystalline Materials, Treatise on Materials Science and Engineering," p. 93. The Minerals, Metals and Materials Research Society, Pittsburgh, PA, 1996.

8. G. H. Campbell, S. M. Foiles, H. Huang, D. A. Hughes, W. E. King, D. H. Lassila, D. J. Nikkel, T. Diaz de la Rubia, J. Y. Shu, and V. P. Smyshlyaev, *Mat. Sci. Eng.* A251, 1 (1998).

9. H. Mughrabi, *Acta Met.* 31, 1367 (1983).

10. H. Mughrabi, *Mat. Sci. Eng.* 85, 15 (1987).

11. R. J. Amodeo and N. M. Ghoniem, *Res. Mech.* 23, 137 (1988).

12. M. Born and J. R. Oppenheimer, *Ann. Physik.*, 84, 457 (1927).

13. R. G. Parr and W. Yang, "Density Functional Theory of Atoms and Molecules." Oxford University Press, New York, 1989.

14. R. M. Dreizler and E. K. U. Gross, "Density Functional Theory." Springer, Berlin, 1990.

15. L. H. Thomas, *Proc. Cambridge Philos. Soc.* 23, 542 (1927).

16. E. Fermi, *Z. Phys.* 48, 73 (1928).

17. P. Fulde, "Electron Correlations in Molecules and Solids." Springer Verlag, Berlin, 1993.

18. J. Phillips and L. Kleinman, *Phys. Rev.* 116, 287 (1959).

19. W. E. Pickett, "Computer Physics Reports," Vol. 9, p. 115. North Holand, Amsterdam, 1989.

20. E. Wigner, *Phys. Rev.* 46, 1002 (1934).

21. N. H. March, *Adv. Phys.* 6, 1 (1957).

22. W. Kohn and L. J. Sham, *Phys. Rev.* 140, A1133 (1965).

23. P. Hohenberg and W. Kohn, *Phys. Rev.* 136, 864B (1964).

24. R. O. Jones and O. Gunnarsson, *Rev. Mod. Phys.* 61, 689 (1989).

25. N. W. Ashcroft and N. D. Mermin, Solid State Physics, Saunders College, Philadelphia, 1976.

26. J. P. Perdew, in "Exchange and Correlation in Atoms, Molecules, and Solids: The Density Functional Picture" (A. Gonis, N. Kioussis, and M. Ciftan, Eds.), p. 287. Electron Correlations and Materials Properties, Kluwer and Plenum, New York, 1999.

27. R. Car and M. Parrinello, *Phys. Rev. Lett.* 55, 2471 (1985).

28. M. C. Payne, M. P. Teter, D. C. Allan, T. A. Arias, and J. D. Joannopoulos, *Rev. Mod. Phys.* 64, 1045 (1992).

29. M. J. Gillan, *J. Phys.: Condens. Matter* 1, 689 (1989).

30. U. von Barth and L. Hedin, *J. Phys. C* 5, 1629 (1972).

31. L. Hedin and B. Lundqvist, *J. Phys. C* 4, 2064 (1971).

32. S. H. Vosko, L. Wilk, and M. Nusair, *Can. J. Phys.* 58, 1200 (1980).

33. J. P. Perdew and A. Zunger, *Phys. Rev. B* 23, 5048 (1981).

34. J. Harris and R. O. Jones, *J. Phys. F* 4, 1170 (1974).

35. O. Gunnarsson and B. I. Lundqvist, *Phys. Rev. B* 13, 4274 (1976).

36. D. C. Langreth and J. P. Perdew, *Phys. Rev. B* 15, 2884 (1977).

37. J. P. Perdew, in "Unified Theory of Exchange and Correlation Beyond the Local Density Approximation" (P. Ziesche and H. Eschrig, Eds.), p. 11. *Electronic Structure of Solids '91*, Akademie Verlag, Berlin, 1991.

38. J. P. Perdew, K. Burke, and Y. Wang, *Phys. Rev. B* 54, 16533 (1996).

39. H. Eschrig, "Optimized LCAO Method and the Electronic Structure of extended Systems." Springer-Verlag, Berlin, 1989.

40. P. J. H. Denteneer and W. van Haeringen, *J. Phys. C* 18, 4127 (1985).

41. E. Wimmer, H. Krakauer, M. Weinert, and A. J. Freeman, *Phys. Rev. B* 24, 864 (1981).

42. D. L. Price and B. R. Cooper, *Phys. Rev. B* 39, 4945 (1989).

43. D. L. Price, J. M. Wills, and B. R. Cooper, *Phys. Rev. B* 46, 11368 (1992).

44. N. Papanikolaou, R. Zeller, and P. H. Dederichs, *J. Phys.: Condens. Matter* 14, 2799 (2002).

45. V. Anisimov, "*Strong Coulomb Correlations in Electronic Structure Calculations: Beyond the Local Density Approximation*." Gordon and Breach Science, Amsterdam, 2000.

46. V. I. Anisimov, J. Zaanen, and O. K. Andersen, *Phys. Rev. B* 44, 943 (1991).

47. A. I. Lichtenstein, J. Zaanen, and V. I. Anisimov, *Phys. Rev. B* 52, R5467 (1995).

48. A. Svane and O. Gunnarsson, *Phys. Rev. Lett.* 65, 1148 (1990).

49. A. Georges, G. Kotliar, W. Krauth, and M. Rozenberg, *Rev. Mod. Phys.* 68, 13 (1996).

50. E. K. U. Gross, T. Kreibich, M. Lein, and M. Petersilka, in "Orbital Functionals in Static and Time-Dependent Density Functional Theory" (N. Kioussis, A. Gonis, and M. Ciftan, Eds.), p. 393. Electron Correlations and Materials Properties, Kluwer/Plenum, New York, 1998.

51. C. E. Dykstra, "Ab initio Calculation of the Structure and Properties of Molecules." Elsevier, Amsterdam, 1988.

52. L. Hedin and S. Lundqvist, in "Solid State Physics, Advances in Research and Application" (F. Seitz, D. Turnbell, and H. Ehrenreich, Eds.), Vol. 23, p. 1. Academic, New York, 1969.

53. S. G. Louie, in "Quasiparticle Theory of Electron Excitations in Solids" (J. R. Chelikowsky and S. G. Louie, Eds.), p. 83. Quantum Theory of Real Materials, Kluwer, Boston, 1996.

54. W. Yang. *Phys. Rev. Lett.* 66, 1438 (1991).

55. X. P. Li, R. W. Nunes, and D. Vanderbilt, *Phys. Rev. B* 47, 10891 (1993).

56. P. Ordejon, D. A. Drabold, M. P. Grumbach, and R. M. Martin, *Phys. Rev. B* 48, 14646 (1993).

57. S. Goedecker, *Rev. of Modern Phys.* 71, 1085 (1999).

58. N. Marzari and D. Vanderbilt, *Phys. Rev. B* 56, 12847 (1997).
59. R. W. Nunes, J. Bennetto, and D. Vanderbilt, *Phys. Rev. Lett.* 77, 1516 (1996).
60. S. Ismail-Beigi and T. A. Arias, *Phys. Rev. Lett.* 82, 2127 (1999).
61. G. Galli and F. Mauri, *Phys. Rev. Lett.* 73, 3471 (1994).
62. P. M. Ajayan, V. Ravikumar, and J.-C. Charlier, *Phys. Rev. Lett.* 81, 1437 (1998).
63. J. P. Lewis, P. Ordejon, and O. Sankey, *Phys. Rev. B* 55, 6880 (1997).
64. J. E. Lennard-Jones, *Proc. Roy. Soc. A* 106, 463 (1924).
65. P. M. Morse, *Phys. Rev.* 34, 57 (1929).
66. M. Daw and M. Baskes, *Phys. Rev. Lett.* 50, 1285 (1983).
67. M. Daw and M. Baskes, *Phys. Rev. B* 29, 6443 (1984).
68. M. Finnis and J. Sinclair, *Phil. Mag. A* 50, 45 (1984).
69. F. H. Stillinger and T. A. Weber, *Phys. Rev. B* 31, 5262 (1985).
70. G. J. Ackland and V. Vitek, *Phys. Rev. B* 41, 10324 (1990).
71. J. Tersoff, *Phys. Rev. Lett.* 56, 632 (1986).
72. R. Johnson, *Phys. Rev. B* 37, 3924 (1988).
73. M. I. Baskes, S. M. Foiles, and M. S. Daw, *Phys. Rev. B* 33, 7983 (1986).
74. J. R. Smith, F. Guinea, J. H. Rose, and J. Ferrante, *Phys. Rev. B* 29, 2963 (1984).
75. R. E. Cohen, M. Mehl, and D. A. Papaconstantopoulos, *Phys. Rev. B* 50, 14694 (1994).
76. M. Mehl and D. A. Papaconstantopoulos, *Phys. Rev. B* 54, 4519 (1996).
77. Th. Frauenheim, D. Porezag, M. Elstner, G. Jungnickel, J. Elsner, M. Haugk, and A. Sieck, in "An ab initio Two-Center Tight-Binding Approach to Simulations of Complex Materials Properties" (A. Gonis, P. E. A. Turchi, and L. Colombo, Eds.), Vol. 491, p. 91. Tight-Binding Approach to Computational Materials Science, MRS Symposium Proc., 1998.
78. D. G. Pettifor, *Phys. Rev. Lett.* 63, 2480 (1989).
79. D. G. Pettifor and I. Oleinik, *Phys. Rev. B* 59, 8487 (1999).
80. D. G. Pettifor and I. Oleinik, *Phys. Rev. Lett.* 84, 4124 (2000).
81. J. A. Moriarty, *Phys. Rev. B* 38, 3199 (1988).
82. J. A. Moriarty and M. Widom, *Phys. Rev. B* 56, 7905 (1997).
83. J. A. Moriarty, J. F. Belak, R. E. Rudd, P. Söderlind, F. H. Streitz, and L. H. Yang, *J. Phys.: Condens. Matter* 14, 2825 (2002).
84. C. W. Gear, "Numerical Initial Value Problems in Ordinary Differential Equations." Prentice-Hall, Englewood Cliffs, 1971.
85. E. Kuramoto, K. Ohsawa, and T. Tsutsumi, *J. Comput. Aided Mater. Design* 7, 89 (2000).
86. T. Kido, T. Maruyama, K. Niita, and S. Chiba, *Nucl. Phys. A* 663, 877c (2000).
87. M. Ortiz and R. Phillips, *Adv. Appl. Mech.* 36, 1 (1999).
88. J. E. Sinclair, *J. Appl. Phys.* 42, 5321 (1971).
89. C. H. Woo and M. P. Puls, *J. Phys. C* 9, L27 (1976).
90. R. G. Hoagland, J. P. Hirth, and P. C. Gehlen, *Phil. Mag. A* 34, 413 (1976).
91. S. Rao, C. Hernandez, J. P. Simmons, T. A. Parthasarathy, and C. Woodward, *Phil. Mag. A* 77, 231 (1998).
92. F. F. Abraham, J. Q. Broughton, N. Bernstein, and E. Kaxiras, *Comput. Phys.* 12, 538 (1987).
93. S. I. Golubov, X. L. Liu, H. C. Huang, and C. H. Woo, *Comput. Phys. Commun.* 137, 312 (2001).
94. K. Ohsawa and E. Kuramoto, *J. Appl. Phys.* 86, 179 (1999).
95. W. Cai, M. de Koning, V. V. Bulatov, and S. Yip, *Phys. Rev. Lett.* 85, 3213 (2000).
96. M. Parrinello and A. Rahman, *J. Appl. Phys.* 52, 7182 (1981).
97. S. Nose. *Mol. Phys.* 52, 255 (1984).
98. W. G. Hoover, *Phys. Rev. A* 31, 1695 (1985).
99. F. Ercolessi and J. Adams, *Europhys. Lett.* 26, 583 (1994).
100. M. I. Baskes, *Phys. Rev. Lett.* 59, 2666 (1987).
101. H. C. Huang, N. M. Ghoniem, J. K. Wong, and M. I. Baskes, *Mod. Sim. Mat. Sci. Eng.* 3, 615 (1995).
102. R. Pasianot, D. Farkas, and E. J. Savino, *Phys. Rev. B* 43, 6952 (1991).
103. J. A. Moriarty, *Phys. Rev. B* 49, 12431 (1994).
104. N. X. Chen. *Phys. Rev. Lett.* 64, 1193 (1990).
105. W. Q. Zhang, Q. Xie, X. J. Ge, and N. X. Chen, *J. Appl. Phys.* 82, 578 (1997).
106. M. J. Field, "A Practical Introduction to the Simulation of Molecular Systems." United Kingdom at the University Press, Cambridge, 1999.
107. J. P. M. Postma, W. F. Gunsteren, A. D. Nola, J. R. Haak, H. J. C. Berendsen, *J. Chem. Phys.* 81, 3684, (1984).
108. H. C. Andersen, *J. Chem. Phys.* 72, 2384 (1980).
109. S. Nosé and M. L. Klein, *Mol. Phys.* 50, 1055 (1983).
110. F. James, *Computer Physics Communications* 60, 329 (1990).
111. D. G. Doran, *Rad. Eff.* 2, 249 (1970).
112. J. R. Beeler, "Radiation Effects Computer Experiments." Amsterdam, Netherlands: North-Holland, 1982.
113. H. L. Heinisch, *Nuc. Inst. Meth. Phys. Res. B* 102, 47 (1995).
114. F. Kroupa, in "Dislocation loops" (B. Gruber, Ed.), pp. 275–316. Theory of Crystal Defects, Academic Press, New York, 1966.
115. R. Siems, *Phys. Stat. Sol.* 30, 645 (1968).
116. R. Bullough and J. R. Hardy, *Phil. Mag.* 17, 833 (1968).
117. E. Kröner, *Phys. kondens. Materie.* 2, 262 (1964).

118. C. Teodosiu, "Elastic Models of Crystal Defects," Editura Academiei, Bucuresti; Springer-Verlag, New York, 1982.
119. Yu. N. Osetsky, D. J. Bacon, A. Serra, B. N. Singh, and S. I. Golubov, *J. Nucl. Mater.* 276, 65 (2000).
120. C. C. Battaile and D. J. Srolovitz, *J. Appl. Phys.* 82, 6293 (1997).
121. N. Soneda and T. Diaz de la Rubia, *Phil. Mag. A* 78, 995 (1998).
122. H. L. Heinisch and B. N. Singh, *J. Nucl. Mater.* 251, 77 (1997).
123. N. M. Ghoniem, *Transactions of the ASME, J. Eng. Mater. Tech.* 121, 136 (1999).
124. N. M. Ghoniem and L. Z. Sun, *Phys. Rev. B* 60, 128 (1999).
125. J. Huang and N. M. Ghoniem, *J. Comp. Mater. Sci.* 23, 225 (2002).
126. D. J. Bacon, F. Gao, and Y. N. Osetsky, *J. Nucl. Mater.* 276, 1 (2000).
127. J. D. Eshelby, *Proc. R. Soc. London A* 241, 376 (1957).
128. E. Kröner, *Erg. Angew. Math.* 5, 1 (1958).
129. E. Kröner, "Kontinuumstheorie der Versetzungen und Eigenspannungen." Springer, Berlin, Germany, 1958.
130. T. Mura, "The Continuum Theory of Dislocations, Advances in Materials Research 3." Interscience, New York, 1968.
131. T. Mura, Micromechanics of Defects in Solids, Martinus Nijhoff Publishers, Dordrecht, The Netherlands, 1982.
132. Arnold Markovich Kossevich, "Crystal Lattice Phonons, Solitons, and Dislocations." Wiley, John and Sons, Incorporated, 1999.
133. H. Neuhäuser, in "Slip-line Formation and Collective Dislocation Motion" (F. R. N. Nabarro, Ed.), Vol. 6. Dislocations in Solids, North-Holland, Amsterdam, 1983.
134. M. Zaiser, *Mat. Science Engr. A* 3019, 304 (2001).
135. D. Walgraef and C. Aifantis, *Int. J. Eng. Sci.* 23, 1351 (1985).
136. V. Gregor and J. Kratochvil, *Res. Mech.* 29, 197 (1990).
137. J. Kratochvil and N. Saxlòva, *Scripta metall mater.* 26, 113 (1992).
138. N. Saxlòva, J. Kratochvil, and J. Zatloukal, *Mat. Sci. Eng. A* 234, 205 (1997).
139. P. Hähner, K. Bay, and M. Zaiser, *Phys. Rev. Lett.* 81, 2470 (1998).
140. M. Zaiser, M. Avlonitis, and E. C. Aifantis, *Acta Mat.* 46, 4143 (1998).
141. A. El-Azab, *Phys. Rev. B* 61, 11956 (2000).
142. R. Thomson, L. E. Levine, Y. Shim, D. E. Kramer, and M. F. Savage, *Comp. Mod. Engr. & Sci. (CMES)* 3, 245 (2002).
143. J. Lepinoux and L. P. Kubin, *Scripta Met.* 21, 833 (1987).
144. N. M. Ghoniem and R. J. Amodeo, *Solid State Phenomena* 3, 377 (1988).
145. N. M. Ghoniem and R. J. Amodeo, *Int J. Eng. Sci.* 26, 653 (1988).
146. R. J. Amodeo and N. M. Ghoniem, *Phys. Rev.* 41, 6958 (1990).
147. R. J. Amodeo and N. M. Ghoniem, *Phys. Rev.* 41, 6968 (1990).
148. A. N. Guluoglu, D. J. Srolovitz, R. LeSar, and R. S. Lomdahl, *Scripta Met.* 23, 1347 (1989).
149. J. A. Blume, V. A. Lubarda, and A. Needleman, *Acta Met. et Mat.* 41, 625 (1993).
150. D. B. Barts and A. E. Carlsson, *Phys. Rev. E* 52, 3195 (1995).
151. D. B. Barts and A. E. Carlsson, *Phil. Mag. A* 77, 751 (1998).
152. H. Y. Wang and R. LeSar, *Phil. Mag. A* 71, 149 (1995).
153. P. Neumann, *Acta Met.* 19, 1233 (1971).
154. N. M. Ghoniem, J. R. Matthews, and R. J. Amodeo, *Res. Mech.* 29, 197 (1990).
155. P. Hähner, *Appl. Phys. A* 62, 473 (1996).
156. M. Zaiser and P. Hähner, *Phys. Stat. Sol. B* 199, 267 (1997).
157. R. LeSar and J. M. Rickman, *Phil. Mag. this issue* (2003).
158. U. Essmann and H. Mughrabi, *Phil. Mag. A.* 40, 731 (1979).
159. L. P. Kubin and J. Kratochvil, *Phil. Mag. A* 80, 201 (2000).
160. H. Mughrabi, "Cyclic plasticity of Matrix and Persistent Slip Bands in Fitigued Metals" (O. Brulin and R. K. T. Hsi, Eds.), Proceedings of the Fourth International Conference on Continuum Models of discrete Systems, North Holland, Amsterdam, 1981.
161. E. Kröner, Continuum Theory of Defects, Course 3. Physics of Defects, Les Houches Session XXXV, p. 217. North-Holland, Amsterdam, 1981.
162. I. Groma, *Phys. Rev. B* 56, 5807 (1997).
163. C. Hartley, "Stereological Determination of Dislocation Density Metrics," Proceedings of the International Conference on Plasticity, Quebec City, Canada, 2003.
164. D. Hughes, D. C. Chrzan, Q. Liu, and N. Hansen, *Phys. Rev. Lett.* 81, 4664 (1998).
165. R. Thomson and L. E. Levine, *Phys. Rev. Lett.* 81, 3884 (1998).
166. Y. Shim, L. E. Levine, and R. Thomson, *Mat. Sci. Engr. A* 309, 340 (2001).
167. D. Stauffer and A. Aharony, "Introduction to Percolation Theory." Taylor and Francis, London, 1992.
168. R. LeSar, R. Najafabadi, and D. J. Srolovitz, *Phys. Rev. Lett.* 63, 624 (1989).
169. R. LeSar and J. M. Rickman, *Phys. Rev. B* 65, 144110 (2002).
170. J. Rickman, R. LeSar, and D. J. Srolovitz, *Acta Mater.* 51, 1199 (2003).
171. N. G. Van Kampen, "Stochastic Processes in Physics and Chemistry." North-Holland, New York, (1992).
172. N. M. Ghoniem and R. J. Amodeo, "Numerical Simulation of Dislocation Patterns During Plastic Deformation" (D. Walgreaf and N. M. Ghoniem, Eds.), p. 303. Patterns, Defects and Material Instabilities, Kluwer Academic Publishers, Dordrecht, 1990.

173. R. J. Amodeo and N. M. Ghoniem, in "Rapid Algorithms for Dislocation of Dynamics in Micromechanical Calculations" (P. Follansbee, T. Lowe, T. Rollett, and G. Daehn, Eds.), p. 125. Modeling of Deformation of Crystalline Solids, TMS Press, 1991.
174. N. M. Ghoniem, in "Non-linear Dynamics of Shear Crack Interaction with Dislocations" (L. Kubin, Martin, and G., Eds.), Non-Linear Phenomena in Material Science II, Kluwer Academic Publishers, 1992.
175. I. Groma and G. S. Pawley, *Phil. Mag. A* 67, 1459 (1993).
176. L. P. Kubin, G. Canova, M. Condat, B. Devincre, V. Pontikis, and Y. Brechet, *Diffusion and Defect Data—Solid State Data, Part B (Solid State Phenomena)* 23, 455 (1992).
177. L. P. Kubin and G. Canova, *Scripta Met. et Mater.* 27, 957 (1992).
178. B. DeVincre and M. Condat, *Acta Metall.* 40, 2629 (1992).
179. G. Canova, Y. Brechet, and L. P. Kubin, in "3D Dislocation Simulation of Plastic Instabilities by Work-softening in Alloys" (S. I. Anderson et al., Eds.), Modeling of Plastic Deformation and its Engineering Applications, RISØNational Laboratory, Roskilde, Denmark, 1992.
180. B. DeVincre, V. Pontikis, Y. Brechet, G. Canova, M. Condat, and L. P. Kubin, in "Three-dimensional Simulations of Plastic Flow in Crystals" (M. Mareschal and B. L. Lolian, Eds.), p. 413. Microscopic Simulations of Complex Hydrodynamic Phenomena, Plenum Press, New York, 1992.
181. L. P. Kubin, *Phys. Stat. Sol. A* 135, 433 (1993).
182. B. Devincre and L. P. Kubin, *Mod. Sim. Mater. Sci. Eng.* 2, 559 (1994).
183. G. Canova, Y. Brechet, L. P. Kubin, B. DeVincre, V. Pontikis, and M. Condat, in "3D Simulation of Dislocation Motion on a Lattice: Application to the yield surface of single crystals" (J. Rabiet, Ed.), Microstructures and Physical Properties, 2000.
184. J. P. Hirth, M. Rhee, and H. Zbib, *J. Comp.-Aided Mat. Design* 3, 164 (1996).
185. K. V. Schwarz and J. Tersoff, *App. Phys. Lett.* 69, 1220 (1996).
186. K. W. Schwarz, *Phys. Rev. Lett.* 78, 4785 (1997).
187. K. W. Schwarz and F. K. LeGoues, *Phys. Rev. Lett.* 78, 1877 (1997).
188. R. M. Zbib, M. Rhee, and J. P. Hirth, *In. J. Mech. Sci.* 40, 113 (1998).
189. M. Rhee, H. M. Zbib, J. P. Hirth, H. Huang, and T. de la Rubia, *Mod. Sim. Mater. Sci. Eng.* 6, 467 (1998).
190. N. M. Ghoniem and L. Z. Sun, *Phys. Rev. B* 60, 128 (1999).
191. N. M. Ghoniem, *Transactions of ASME. J. Eng. Mat. Tech.* 121, 136 (1999).
192. N. M. Ghoniem, S.-H. Tong, and L. Z. Sun. *Phys. Rev.* 61, 913 (2000).
193. N. M. Ghoniem, J. Huang, and Z. Wang, *Phil. Mag. Lett.* 82, 55 (2001).
194. R. V. Kukta and L. B. Freund, in "Three-Dimensional Numerical Simulation of Interacting Dislocations in a Strained Epitaxial Surface Layer" (V. V. Bulatov, T. Diaz de la Rubia, R. Phillips, E. Kaxiras, and N. M. Ghoniem, Eds.), Multiscale Modelling of Materials, Materials Research Society, Boston, Massachusetts, USA, 1998.
195. A. Moulin, M. Condat, and L. P. Kubin, *Acta Mater.* 45, 2339 (1997).
196. L. M. Brown, *Phil. Mag.* 15, 363 (1967).
197. A. G. Khachaturyan, in "The Science of Alloys for the 21st Century: A Hume-Rothery Symposium Celebration" (E. A. Turchi, A. Gonis, and R. D. Shull, Eds.), Proceedings of a symposium of TMS, TMS, 2000.
198. Y. U. Wang, Y. M. Jin, A. M. Cuitino, and A. G. Khachaturyan, Presented at the International Conference, Dislocations 2000, the National Institute of Standards and Technology, Gaithersburg, p. 107. 2000.
199. Y. U. Wang, Y. M. Jin, A. M. Cuitino, and A. G. Khachaturyan, *Acta Mat.* 49, 1847 (2001).
200. V. Volterra, *Annal. Sci. de l'École Norm. Super., Paris* 24, 401 (1907).
201. R. deWit, in "The Continuum Theory of Stationary Dislocations" (F. Seitz and D. Turnbull, Eds.), Sol. State Phys. 10, Academic Press, 1960.
202. M. O. Peach and J. S. Koehler, *Phys. Rev.* 80, 436 (1950).
203. S. Gavazza and D. Barnett, *J. Mech. Phys. Solids* 24, 171 (1976).
204. T. Mura, *Phil. Mag.* 8, 843 (1963).
205. D. M. Barnett, *Phys. Status Solidi (b)* 49, 741 (1972).
206. J. Willis, *J. Mech. Phys. Solids* 23, 129 (1975).
207. D. J. Bacon, D. M. Barnett, and R. O. Scattergodd, in "Anisotropic Continuum Theory of Lattice Deffects" (J. W. Christian, T. B. Massalski, and B. Chalmers, Eds.), *Progress in Materials Science*, Vol. 23, pp. 51–262, Pergamon Press, Great Britain, 1980.
208. T. Mura, Micromechanics of Defects in Solids, 2nd Edn., Martinus Nijhoff, Dordrecht, 1987.
209. D. Barnett, *Phys. Status Solidi (a)* 38, 637 (1976).
210. D. Weygrand, L. H. Friedman, E. Van der Giessen, and A. Needleman, *Mod. Sim. Mat. Sci. Eng.* 10, 437 (2002).
211. R. Martinez and N. M. Ghoniem, *J. Comp. Mat. Science* 23, 225 (2002).
212. T. A. Khraishi, H. M. Zbib, and T. de la Rubia, *Mater. Sci. Eng. A* 309, 283 (2001).
213. J. Lothe, V. L. Indenbom, and V. A. Chamrov, *Phys. Stat. Sol. (b)* 11, 671 (1982).
214. K. Schwarz, *J. Appl. Phys.* 85, 108 (1999).
215. B. Von Blanckenhagen, P. Gumbsch, and E. Arzt, *Mod. Sim. Mat. Sci. Eng.* 9, 157 (2001).
216. T. J. Gosling and J. R. Willis, *J. Mech. Phys. Solids* 42, 1199 (1994).
217. M. Fivel, T. J. Gosling, and I. Groma, *Mod. Sim. Mat. Sci. Eng.* 4, 581 (1996).
218. M. Verdier, M. Fivel, and I. Groma, *Mod. Sim. Mat. Sci. Eng.* 6, 755 (1998).
219. B. Yang and E. Pan, *Int. J. Solids Struct.* 39, 2235 (2002).
220. B. Yang and E. Pan, *Engng Analysis Boundary Element* 26, 355 (2002).

221. D. M. Barnett and J. Lothe, *Physica Norvegica* 8, 13 (1975).
222. T. C. T. Ting, "Anisotropic Elasticity: Theory and Applications." Oxford University Press, New York, 1996.
223. E. Pan and F. G. Yuan, *Int. J. Solids Struct.* 37, 5329 (1999).
224. F. G. Yuan, S. Yang, and B. Yang, *Int. J. Solids Struct.* 40, 331 (2003).
225. J. P. Hirth and J. Lothe, "Theory of Dislocations," 2nd Edn. John Wiley & Sons, New York, 1982.
226. X. Han, N. Ghoniem, and Z. Wang, *Phil. Mag. A* 83, 3705 (2003).
227. J. S. Koehler, *Phil. Mag.* 2, 547 (1970).
228. X. Han and N. M. Ghoniem, Stress field and interaction forces of dislocations in anisotropic multilayer thin films, *Phil. Mag.*, submitted (2004).
229. R. Hill, in "Progress in Solid Mechanics 2" (I. N. Sneddon and R. Hill, Eds.), pp. 245–276. North-Holland, Amsterdam, 1961.
230. L. Brown, *Phil. Mag.* 10, 441 (1964).
231. Andrew M. Rappe, J. D. Joannopoulos, and P. A. Bash, *J. Am. Chem. Soc.* 114, 6466 (1992).
232. C. Woodward and S. I. Rao, *Phys. Rev. Lett.* 88, 216402 (2002).
233. G. Lu, N. Kioussis, V. Bulatov, and E. Kaxiras, *Phys. Rev. B* 62, 3099 (2000).
234. G. Lu, Q. Zhang, N. Kioussis, and E. Kaxiras, *Phys. Rev. Lett.* 87, 095501 (2001).
235. G. Lu, V. Bulatov, and N. Kioussis, *Phys. Rev. B* 66, 144103 (2002).
236. G. G. Lu, V. Bulatov, and N. Kioussis, *Intern. Journ. of Plasticity* 20, 447 (2004).
237. D. J. H. Cockayne, M. L. Jenkins, and I. L. F. Ray, *Phil. Mag.* 24, 1383 (1971).
238. M. S. Duesbery, in "The dislocation core and plasticity" (F. R. N. Nabarro, Ed.), Vol. 8, p. 67. Dislocations in Solids, North-Holland, Amsterdam, 1989.
239. A. Guimier, *Nature* 142, 568 (1938).
240. G. D. Preston, *Phil. Mag.* 26, 855 (1938).
241. M. Karlík and B. Jouffrey, *J. Phys. III France* 6, 825 (1996).
242. C. Wolverton, *Phil. Mag. Letters* 79, 683 (1999).
243. T. C. Schulthess, P. E. A. Turchi, A. Gonis, and T.-G. Nieh, *Acta Mater.* 46, 2215 (1998).
244. C. H. Woo, H. C. Huang, and W. J. Zhu, *Appl. Phys. A* 76, 101 (2002).
245. V. Vitek, *Crystal Lattice Defects* 5, 1 (1974).
246. M. S. Duesbery and V. Vitek, *Acta Mater.* 46, 1481 (1998).
247. S. I. Rao and C. Woodward, *Phil. Mag. A* 81, 1317 (2001).
248. W. Xu and J. A. Moriarty, *Phys. Rev. B* 54, 6941 (1996).
249. G. F. Wang, A. Strachan, T. Cagin, and W. A. Goddard, *Mater. Sci. Eng. A* 309, 133 (2001).
250. V. V. Bulatov, S. Yip, and A. S. Argon, *Phil. Mag. A* 72, 453 (1995).
251. W. Xu and J. A. Moriarty, *Comput. Mater. Sci.* 9, 348 (1998).
252. S. J. Zhou, D. L. Preston, P. S. Lomdahl, and D. M. Beazley, *Science* 279, 1525 (1998).
253. D. Rodney and R. Phillips, *Phys. Rev. Lett.* 82, 1704 (1999).
254. D. Rodney and G. Martin, *Phys. Rev. B* 61, 8714 (2000).
255. J. F. Justo, M. de Koning, W. Cai, and V. V. Bulatov, *Mater. Sci. Eng. A* 309, 129 (2001).
256. P. Gumbsch and H. Gao, *Science* 283, 965 (1999).
257. S. Q. Shi, H. C. Huang, and C. H. Woo, *Comput. Mater. Sci.* 23, 95 (2002).
258. Q. K. Li and S. Q. Shi, *Appl. Phys. Lett.* 80, 3069 (2002).
259. J. Wang, C. H. Woo, and H. C. Huang, *Appl. Phys. Lett.* 79, 101 (2001).
260. H. C. Huang, N. M. Ghoniem, T. Diaz de la Rubia, M. Rhee, H. Zbib, and J. P. Hirth, *J. Eng. Mater. Tech.* 121, 143 (1999).
261. V. V. Bulatov, F. F. Abraham, L. Kubin, B. Devincre, and S. Yip, *Nature* 391, 669 (1998).
262. W. C. Liu, S. Q. Shi, H. C. Huang, and C. H. Woo, *Comput. Mater. Sci.* 23, 155 (2002).
263. W. C. Liu, S. Q. Shi, C. H. Woo, and H. C. Huang, *Comput. Model. Eng. Sci.* 3, 213 (2002).
264. H. Van Swygenhoven, A. Caro, and D. Farkas, *Mater. Sci. Eng. A* 309, 440 (2001).
265. F. Cleri, D. Wolf, S. Yip, and S. R. Phillpot, *Acta Mater.* 45, 4993 (1997).
266. H. Van Swygenhoven, *Science* 296, 66 (2002).
267. B. Schonfelder, D. Wolf, S. R. Phillpot, and M. Furtkamp, *Interface Sci.* 5, 245 (1997).
268. B. Schonfelder, P. Keblinski, D. Wolf, and S. R. Phillpot, *Mater. Sci. Forum* 294, 9 (1999).
269. J. P. Chang, W. Cai, V. V. Bulatov, and S. Yip, *Mater. Sci. Eng. A* 309, 160 (2001).
270. J. C. Hamilton, R. Stumpf, K. Bromann, M. Giovannini, K. Kern, and H. Brune, *Phys. Rev. Lett.* 82, 4488 (1999).
271. J. C. Hamilton, *Phys. Rev. B* 55, R7402 (1997).
272. N. Soneda and Diaz de la Rubia, *Phil. Mag. A* 81, 331 (2001).
273. J. O. Stiegler and E. E. Bloom, *Radiat. Eff.* 8, 34 (1971).
274. B. N. Singh, A. Horsewell, P. Toft, and D. J. Edwards, *J. Nucl. Mater.* 224, 131 (1995).
275. B. N. Singh, A. J. E. Foreman, and H. Trinkaus, *J. Nucl. Mater.* 249, 103 (1997).
276. M. Eldrup, B. N. Singh, S. J. Zinkle, T. S. Byun, and K. Farrell, *J. Nucl. Mater.* 307, 912 (2002).
277. H. Trinkaus, B. N. Singh, and A. J. E. Foreman, *J. Nucl. Mater.* 249, 91 (1997).
278. B. N. Singh, A. Horsewell, and P. Toft, *J. Nucl. Mater.* 271, 97 (1999).
279. H. Trinkaus, B. N. Singh, and A. J. E. Foreman, *J. Nucl. Mater.* 206, 200 (1993).
280. F. Gao, G. Henkelman, W. L. Weber, L. R. Corrales, and H. Jonsson, *Nucl. Instr. and Meth. B* 202, 1 (2003).
281. Yu. N. Osetsky, A. Serra, and V. Priego. *J. Nucl. Mater.* 276, 202 (2000).
282. B. N. Singh and S. J. Zinkle, *J. Nucl. Mater.* 206, 212 (1993).

283. J. L. Brimhall and B. Mastel, *Radiat. Effects* 3, 203 (1970).
284. Z. Wang, N. M. Ghoniem, R. LeSar, and S. Sriram, *Mod. Sim. Mat. Sci. Eng.* (2003).
285. J. Huang and N. M. Ghoniem, *Mod. Sim. Mat. Sci. Eng.* 10, 1 (2002).
286. R. Scattergood and D. Bacon, *Phys. Stat. Sol.(a)* 25, 395 (1974).
287. M. Shinn, L. Hultman, and S. Barnett, *J. Mater. Res.* 7, 901 (1992).
288. A. Misra, V. Verdier, Y. C. Lu, H. Kung, T. E. Mitchell, M. Nastasi, and J. D. Embury, *Scripta Materialia* 39, 555 (1998).
289. B. M. Clemens, H. Kung, and S. A. Barnett, *MRS Bulletin* 20, 20 (1999).
290. B. J. Daniels, W. D. Nix, and B. M. Clemens, in "Thin Films:Stress and Mechanical Properties V" (P. H. Townsend, C. A. Volkert, S. P. Baker, C. A. Ross, and P. Borgesen, Eds.), Vol. 356, pp. 373–378. *Mater. Res. Soc. Symp. Proc.* Pittsburgh, 1995.
291. B. J. Daniels, W. D. Nix, and B. M. Clemens, in "Structure and Properties of Multilayered Thin Films" (B. M. Clemens, S. C. Shin, K. Sato, T. D. Nguyen, and B. M. Lairson, Eds.), Vol. 382, pp. 373–378. *Mater. Res. Soc. Symp. Proc.* Pittsburgh, 1995.
292. L. Freund, *J. Mech. Phys. Solids* 58, 657 (1990).
293. W. Nix, *Scripta Materialia* 39, 545 (1998).
294. A. J. E. Foreman, *Phil. Mag.* 15, 1011 (1967).
295. P. M. Anderson and Z. Li, *Marerials Science and Engineering* A319, 182 (2001).
296. P. M. Anderson, T. Foecke, and P. M. Hazzledine, *MRS Bulletin* 20, 27 (1999).
297. A. Misra, V. Verdier, H. Kung, J. D. Embury, and J. P. Hirth, *Scripta Materialia* 41, 973 (1999).